Evaluation of Image Quality and Reconstruction Parameters in Recent PET-CT and PET-MR Systems

Evaluatie van de beeldkwaliteit en reconstructieparameters in recente PET-CT- en PET-MR-systemen

Paulo Rauli Rafeson De Vasconcelos Caribé

Promotoren: prof. dr. S. Vandenberghe, prof. dr. M. Koole
Proefschrift ingediend tot het behalen van de graad van
Doctor in de ingenieurswetenschappen: biomedische ingenieurstechnieken

UNIVERSITEIT
GENT

Vakgroep Elektronica en Informatiesystemen
Voorzitter: prof. dr. ir. K. De Bosschere
Faculteit Ingenieurswetenschappen en Architectuur
Academiejaar 2019 - 2020

ISBN 978-94-6355-366-7
NUR 954
Wettelijk depot: D/2020/10.500/43

Medical Image and Signal Processing (MEDISIP)
Department of Electronics and Information Systems
Faculty of Engineering and Architecture
Ghent University

GHENT
UNIVERSITY

Corneel Heymanslaan 10
Entrance 36, floor 5
9000 Ghent
Belgium

Promotors
Prof. dr. Stefaan Vandenberghe
Prof. dr. Michel Koole

Examination board
Prof. dr. Hennie De Schepper, Ghent University, *chair*
Prof. dr. Christian Vanhove, Ghent University *secretary*
Prof. dr. ir. Yves D'Asseler, Ghent University
Prof. dr. Ana Maria Marques da Silva, PUCRS, Brazil
Dr. ir. Roel Wierts, Maastricht University, Netherlands
Prof. dr. Michel Koole, KU Leuven
Prof. dr. Stefaan Vandenberghe, Ghent University

This work was funded by a PhD Fellowship from the National Council of Technological and Scientific Development - CNPq, Brazil (process number 235040/2014-2).

Acknowledgements

"*You see things, and you say Why? But I dream things that never were, and I say Why not?*"
Bernard Shaw

I am quite sure you probably know that a PhD student's life is not all rainbows and butterflies, don't you? By definition, the nature of research means that things will not always go according to plan and most of the things you do will fail, over and over again. You just have to keep calm, take a break and then carry on until something finally works. It can be tough, indeed, but the doctoral journey is full of wonderful experiences and may also allow you to work on something that fascinates you greatly. It gives the possibility to socialize with your multidisciplinary lab group and to cooperate with other students from different countries and fields of expertise. And believe me, this is a great way to discuss PhD experiences, get advice and help, improve your research and make friends. I feel blessed because during my journey I received generous support from many people in Ghent and across this beautiful country. Therefore, I would like to begin this thesis by expressing my sincere gratitude to all of you.

First of all, I would like to thank my supervisors, **prof. dr. Stefaan Vandenberghe** and **prof. dr. Michel Koole**, for their support throughout my PhD, without whom none of this would have been possible. They have introduced me to their network, given me the chance to travel, go to international conferences and meet so many interest-

ing researchers. I appreciate all your professional contribution and your endless support in every aspect of my PhD. **Stefaan**, you allowed me to work as a researcher at **MEDISIP** research group. Giving me enough freedom to pave my way in science and you were always available for questions and scientific discussions. My experience here has been incredibly diverse, valuable and opened a lot of doors in my future and for that, I am very grateful. Together with **prof. dr. Roel Van Holen**, **prof. dr. Christian Vanhove**, **prof. ir. Vincent Keereman** and **prof. dr. ir. Pieter van Mierlo** you succeed in achieving a high-quality scientific output while managing the **MEDISIP** group in a friendly way. **Michel**, I also want to thank you for allowing me to do part of my research in Leuven and for introducing me to so many interesting people in the nuclear medicine research domain. Your motivation to work has inspired me and I still cannot believe how you manage to combine all your activities. Whenever I knocked at your office's door, with a question, you would find some time to help me, especially in improving my papers before the submission.

Several people have contributed to the scientific content of this PhD. In particular, I want to thank **prof. dr. ir. Yves D'Asseler** and **dr. lic. Jan Courtyn** from Ghent University Hospital, for the fruitful collaboration we had in the past years, for their hard work to run experiments so swiftly, for the valuable feedback on results and manuscripts and for making this project a success, now and in the future. I owe thanks to **dr. ir Kristof Baete**, **Georg Schramm**, **Jef Van Loock**, **Kwinten Porters** and **Nathalie Mertens** from the department of nuclear medicine and molecular imaging at KU Leuven, for the pleasant cooperation on my research in Leuven and their insightful comments and suggestions. I also would like to thank **prof. dr. Alexander Hammers** and **prof. dr. Paul Marsden** from King's College London for the support and the interesting conversations during my short-training in the St Thomas' PET Centre at St Thomas' Hospital. A special thanks to **dr. ir Nikolaos Efthimiou** (University of Pennsylvania, USA), **prof. dr. Damian Borys** (Silesian University of Technology, Poland) and the PET/MR engineering (GE Healthcare) **Timothy Deller** for their pleasant cooperation on the PET/MR GATE-model project. I am also grateful to the members of the examination board for their advice

and suggestions to improve this manuscript, OBRIGADO.

I wish to thank all the colleagues at **MEDISIP** for keeping up the friendship in our research group, the pleasant lunch breaks and drinks in the kitchen. I always felt at home here (even being out of my home country for so long time). First of all, I owe gratitude to my former colleagues. I am grateful to my first office mates, **Carmen**, **Radek**, **Lara**, **Ester** (btw, what a beautiful name Ester is!) and **Stijn** for their funny stories and for the warm welcome in Ghent. Particularly, Stijn (the last one of this generation) for helping me in understanding the UGent websites and introducing me the best red-brown beer in Belgium, Rodenbach Grand Cru. Also, I wish you all the best with your upcoming wedding. I am so happy for you and Valérie! Next, I need to thank **Thibault** and **Willeke** for sharing your PhD book source code (and Stijn), **Prakash** for showing the best of India, **Marek** (and Darja) for inviting me to play the guitar in your wonderful wedding in Chomutov, Czech Republic (my pleasure). Thanks for being a great friend and for showing the way away to the "Tatratea mountains". **Kim**, (the sweetest heart in the lab) thanks for sharing your notes and backing me up during our doctoral training courses (tough times). **Jens** and **Tim**, who has been a great support in my PhD, OBRIGADO.

I would like to express my gratitude to my current colleagues. Much of gratitude is owed to **Mariele**, who has become a true friend and taught me how to make German Pretzels (so good!). Thank you for laughing with all my silly jokes *"How you doin?"* (she is probably laughing right now) and for always be there for most of my PhD. I wish you the best of luck in your PhD defence next year. **Charlotte** (and Kevin), thanks for opening your home to celebrate together my anniversary with a BBQ (it was amazing!) and for the time we have spent in the office. **Milan**, thank you for the great support in my PhD, as well as many other computer-related things. **Jolan**, thanks for the friendship and being my football teammate. We had a lot of laughs together. **Emma** always had a smile on her face and willing to help someone. **Jens** (Maebe) and **Ashkan** have been my office and lunch mates for the last period of my PhD, so they quickly found their place within **MEDISIP** (and become my new *"Spotify Family"*). Jens, I wish you all the luck with your research! Ashkan, I am convinced your Exoliga-

mentz project will be a great success (I am already missing you guys good vibes and daily high five). **Gert** and **Karnsinee**, I also would like to thank you for our lunch-time discussions about life, the universe, international politics, artificial intelligence. I wish you guys a great PhD journey and remember: the most important outcome of a PhD journey is not the PhD thesis, it is you! A special thanks to **Saskia** and **Inge**, who, have been invaluable to me, by taking care of most administrative tasks and for organizing many great group events (especially, the last team building) which will remain in my memory. And lastly, all my other colleagues who have enriched my journey: **Benedicte** (the sweetest smile), **Katya**, **Lars**, **Syed**, **Pieter Mollet**, **André**, **Lois**, **Amir**, **David** (the coolest guy I've ever met), **Gwenaëlle** and all my football teammates (come on Campus!).

I also thank the many other scientists, research groups and organizations that have been a part of my PhD experience. In particular, I would like to thank all my colleagues from **bioMMeda**. **prof. dr. Patrick Segers**, you have amazed me, not only for your scientific contributions but for your warm-hearted and generosity (you are too good to be *"The Mol"*). Together with **prof. dr. Pascal Verdonck**, **prof. dr. Charlotte Debbaut**, **prof. dr. Martijn van den Broek** and **prof. dr. An Ghysels** your professionalism is an example for many other researchers. I have also received a lot of support from my university "flat-mates", namely **Jurgen**, **Bram**, **Annette**, **MaThias**, **MaTThias**, **Amith**, **Carlos**, **Alessio**, **Federico**, **Viviana**, **Daniela**, **Gerlinde**, **Lise**, **Mohammad**, **Hicham**, **Sarah**, **Shengda** and **Tim Bomberna** (and I'm sorry if I forgot anyone!) OBRIGADO!

A special thanks to **prof. dr. Raul Montagne**, **prof. dr. Sara Cristina**, **prof. dr. Ailton Macedo**, **prof. dr. Wictor Magno**, **prof. dr. Pedro Hugo**, **prof. dr. Mike Sundheimer**, **prof. dr. Ramón González**, **prof. dr. Adalto josé** and **prof. dr. André Vilela** from Physics Department (UFRPE, Brazil) for the valuable feedback and for trusting that I could make it so far.

I also thank my colleagues from the Nuclear Energy Department (UFPE, Brazil), namely **Prof. dr. Helen Khoury**, **Prof. dr. Vagner Cassola**, **Prof. dr. Fernando Lima**, **Prof. dr. Vinícius Barros** and **Prof. dr. José Wilson** (I will never forget your

generosity) for allowing me to work as young researcher and for all supporting that I had. I also thank the medical physicists **Karen**, **Rosa** and **Geneci** for all amazing help during my internship in the Radiotherapy Department, OBRIGADO!

The other researchers I met at the EANM/PSMR/BELNUC conferences. To **CNPq** for funding my research, as well as **Ghent University** and the **Doctoral Schools**, for offering the opportunity to do courses and training in many other fields.

I am very grateful to **Belgium** and **Ghent** for all the amazing opportunities I have had to learn and grow (especially parenthood). Despite the FIFA World Cup 2018 results (Brazil vs Belgium), this beautiful country will be forever in my life, not only because of my PhD experience but for the birth of my sweetest daughter **Esther Caribé**. Together with my lovely wife **Thayenny Caribé**, we will keep this culture alive. **Dank je**! I also made some good friends here who made us feel home away from home. Much of gratitude is owed to pastor **Leo** and his wife **Anneke**, for the honest friendship and a warm welcome to the International Community Church, which has become my family here in Ghent. We love you both! **Els** (my first English teacher in Belgium), I am writing this acknowledgement with deep joy in my heart, thanks to you my friend.

And last but not least, I owe a lot to my family, who have always been by my side and respected my choices in life. **Thayenny**, thank you for always being there for me and showing enough patience during the busy periods of my PhD. This achievement is not only mine but yours too. Thank you for being a life mate and for continuing to change my life! Your perseverance and commitment fascinate me. I love you and increasingly in a new way! My sister **Pérola**, who has been my life-long companion, through laughs and tears, through love and hate, the person in the world who I know I can always count on. Together with **Rodolfo**, you guys gave me the opportunity to be the uncle of **Isabella**, which I am looking forward to meet in person. A special thanks to my brother **Igor** (*"...a friend who sticks closer than a brother"* Proverbs 18:24) for being my brother, study buddy and colleague during the past 10 years. You truly are a warm-hearted and honest man who sets a great example for others. **Aline**, you have brightened up Igor's life much more he could

ever imagine. I am very grateful to my mother **Graça** and my father **Caribé**, where everything started. You both have been my greatest role model, showing me the value of your word and principles, and how much you can accomplish with your drive. You are the truly Champions!

I have greatly appreciated this journey with all of you. OBRIGADO!

Paulo Caribé
Gent, April 26, 2020

Summary

A clinician making a diagnosis based on medical images looks for several different types of indications. These could be changes in the shape of a particular structure, changes in image intensity within that structure compared to normal tissue and the appearance of features such as lesions which are normally not seen. A full diagnosis may be based upon information from several different imaging modalities, which can be correlative or additive in terms of their information content. The work presented in this thesis is situated in the nuclear medicine field. In our research we mainly focus on Positron Emission Tomography (PET).

PET has proven a very valuable imaging tool to explore a variety of cellular and molecular processes *in-vivo*. Because of its high sensitivity, only very low amounts of a PET tracer (a compound labeled with a positron-emitting radionuclide) need to be administered and therefore pharmacological effects and physiological changes are avoided. Once the tracer is injected in the patient and the radiation is detected by the PET scanner, an analytical/iterative algorithm is applied to reconstruct the tracer distribution. This way, PET can provide high contrast and quantitative functional information about the disease state or therapy response, complementary to information provided by anatomical imaging modalities such as computer tomography (CT) or magnetic resonance imaging (MRI).

The diagnostic value of a PET image depends crucially on the image quality, for example, the spatial resolution, signal-to-noise ratio (SNR) and quantitative accuracy. In oncology, these factors determine whether

the physician can detect the tumors (and/or metastases), accurately identify their locations and distinguish them from ordinary inflammations. The image quality in turn is largely determined by the PET system design, PET detector response and is highly impacted by the reconstruction algorithm.

The state-of-the-art of clinical PET scanners has led to a system resolution, that approximates the fundamental limitations of PET imaging. The two main fundamental limitations of resolution in PET are the positron range and the non-collinearity. A positron travels some distance in tissue before it captures an electron and subsequently decays into a pair of 511 keV annihilation photons. Because the position where the annihilation photons are created is different from the position of the parent PET isotope, blurring of the PET signal occurs with a magnitude that is dependent on the energy of the emitted positron and the electron density of the surrounding tissue. While the positron range is inherent to PET imaging and can be considered isotropic within homogeneous tissue, the presence of a strong magnetic field will cause the positron to travel in a helical path, therefore reducing the positron range in the plane transverse to the magnetic field but extending it in the direction along the main magnetic field.

Fully integrated PET/MR systems, combine functional (PET) and anatomical (MR) imaging techniques. These systems are frequently being used in clinical research and routine. The acquisitions are generally done with ^{18}F which is clinically the most relevant PET isotope. However, other PET isotopes, such as ^{68}Ga and ^{90}Y, are gaining clinical importance as they are of specific interest for oncological applications and follow-up of ^{90}Y-based radionuclide therapy. These isotopes have a complex decay scheme with a variety of prompt gammas in coincidence. They have a higher positron energy and, because of the larger positron range, there may be interference with the magnetic field of the MR compared to ^{18}F. Therefore, it is relevant to determine the performance of PET/MR for these clinically relevant and commercially available radioisotopes.

In this PhD dissertation, we propose to derive the impact of using different PET isotopes for the National Electrical Manufacturers Association (NEMA) tests performance evaluation of the GE Signa integrated

PET/MR. The methods were divided into three closely related categories: NEMA performance measurements, system modelling and evaluation of the image quality of the state-of-the-art of clinical PET scanners. NEMA performance measurements for characterizing spatial resolution, sensitivity, image quality, the accuracy of attenuation and scatter corrections (IQ), and noise equivalent count rate (NECR) were performed using clinically relevant and commercially available radioisotopes. Then we modelled the GE Signa integrated PET/MR system using a realistic GATE Monte Carlo simulation and validated it with the result of the NEMA measurements (sensitivity and NECR). Monte Carlo simulations were implemented in GATE and run in the high-performance computer *Vlaams Supercomputer Centrum* installed at Ghent University. The simulated system has an axial and transaxial field-of-view of 25 cm and 60 cm respectively, uses a LYSO scintillator with crystal elements of 25 x 4.0 x 5.3 mm^3, an energy window of 425-650 keV and a coincidence window of 4.57 ($\pm$2.29 ns). The geometry was modelled using the cylindrical PET system in GATE, considering foam, plastic and copper shielding between the field of view and the detectors. To characterize the effect of the 3 T MR field on the positron range, we simulated point sources of positron-emitting radionuclides including ^{18}F, ^{11}C, ^{15}O, ^{13}N, ^{82}Rb and ^{68}Ga positioned in the middle of a homogeneous 20 x 20 x 20 cm^3 cube with different tissue media (soft-tissue, lung-tissue and bone).

For the evaluation of the image quality of the state-of-the-art of clinical PET scanners, we proposed a noise reduction study using a Bayesian Penalized-Likelihood reconstruction algorithm on a time-of-flight PET/CT scanner. The performance and clinical use of a block sequential regularized expectation maximization (BSREM) penalized-likelihood reconstruction algorithm were compared to the ordered-subset expectation maximization (OSEM) with full modelling of PSF and TOF information for both algorithms. The NEMA IQ phantom and a whole-body patient study were acquired on a new GE Discovery MI PET/CT 3-rings system (axial FOV of 15 cm) in list mode and different datasets with varying noise levels were generated. Phantom data were evaluated using four different contrast ratios (8:1, 6:1, 4:1 and 2:1). These were reconstructed using BSREM with different β-factors of 300–3000 and with a clinical setting used for OSEM including point spread function

(PSF) and time-of-flight (TOF) information. Both phantom and patient data were analyzed with regards to contrast recovery (CR), background coefficient of variance (COV), contrast-to-noise ratio (CNR), SUV ratio, metabolic active tumour volumes (MATVs) and signal-to-noise ratio (SNR). This study aimed to evaluate different β-factors compared to a clinical post-filter kernel for different datasets with varying noise levels to investigate whether and to what extent noise can be reduced by using BSREM instead of OSEM.

The outcome of this thesis will allow clinicians to reduce the PET dose which is especially relevant for young patients. Besides, the Monte Carlo simulation platform for PET/MR developed for this thesis will allow physicists and engineers to better understand and design integrated PET/MR systems. For some remaining issues, suggestions for future research will be presented in the final chapter.

Samenvatting

Een arts die op basis van medische beelden een diagnose stelt, zoekt steeds naar een aantal verschillende soorten indicaties. Dit kunnen veranderingen in de vorm van een bepaalde structuur zijn, veranderingen in de beeldintensiteit binnen die structuur in vergelijking met normaal weefsel en het verschijnen van kenmerken zoals laesies die normaal niet worden gezien. Een volledige diagnose kan gebaseerd zijn op informatie uit verschillende beeldvormingsmodaliteiten, die correlatief of additief kunnen zijn in termen van hun informatie-inhoud. Het werk in dit proefschrift situeert zich op het gebied van nucleaire geneeskunde. In ons onderzoek richten we ons vooral op Positron Emission Tomography (PET).

PET heeft zich bewezen als een zeer waardevol beeldvormingsinstrument voor het verkennen van verschillende cellulaire en moleculaire processen in vivo. Vanwege de hoge gevoeligheid moeten slechts zeer kleine hoeveelheden van een PET-tracer (een verbinding gelabeld met een positron-emitterend radionuclide) worden toegediend waardoor farmacologische effecten en fysiologische veranderingen vermeden worden. Nadat de patiënt is geïnjecteerd met de tracer en de straling is gedetecteerd door de PET-scanner, wordt een analytisch/iteratief algoritme toegepast om de tracerverdeling te reconstrueren. Op deze manier kan PET zowel hoog contrast en kwantitatieve functionele informatie bieden over de ziektetoestand of therapierespons, aanvullend op informatie die wordt bekomen via anatomische beeldvormende modaliteiten zoals computertomografie (CT) of magnetische resonantiebeeldvorming (MRI).

De diagnostische waarde van een PET-beeld hangt cruciaal af van de beeldkwaliteit, dewelke o.a. bepaald wordt door de ruimtelijke resolutie, signaal-ruisverhouding (SNR) en kwantitatieve nauwkeurigheid. In de oncologie bepalen deze factoren of de arts in staat is om de tumoren (en/of metastase) te detecteren, hun locaties nauwkeurig te identificeren en ze te onderscheiden van gewone ontstekingen. De beeldkwaliteit wordt op zijn beurt grotendeels bepaald door het ontwerp van het PET-systeem, de respons van de PET-detector en wordt sterk beïnvloed door het reconstructie-algoritme.

De state-of-the-art van klinische PET-scanners heeft geleid tot een systeemresolutie die de fundamentele beperkingen van PET-beeldvorming benadert. De twee belangrijkste fundamentele beperkingen van PET zijn het positronbereik en de acolliniariteit. Een positron reist enige afstand in weefsel voordat het een elektron vangt dewelke vervolgens annihileren in een paar 511 keV-fotonen. Omdat de positie waar de annihilatiefotonen worden gecreëerd, verschilt van de positie van de oorspronkelijke PET-isotoop, treedt vervaging van het PET-signaal op met een grootte die afhankelijk is van de energie van het uitgezonden positron en van de elektronendichtheid van het omliggende weefsel. Hoewel het positronbereik inherent is aan PET-beeldvorming en kan worden beschouwd als isotroop in homogeen weefsel, zal de aanwezigheid van een sterk magnetisch veld ervoor zorgen dat het positron in een spiraalvormige baan reist. Hierdoor wordt het positronbereik in het vlak dwars op het magnetische veld verkleind, terwijl dit bereik zal uitbreiden in de richting langs het magnetische hoofdveld.

Volledig geïntegreerde PET/MR-systemen combineren functionele (PET) en anatomische (MR) beeldvormingstechnieken. Deze systemen worden vaak gebruikt in onderzoek en klinische routine. De acquisities worden doorgaans gedaan met ^{18}F, wat klinisch het meest relevante PET-isotoop is. Andere PET-isotopen, zoals ^{68}Ga en ^{90}Y, worden echter steeds belangrijker omdat ze van specifiek belang zijn voor oncologische toepassingen en voor de opvolging van ^{90}Y op radionuclide gebaseerde therapie. Deze isotopen hebben een complex vervalschema met een groot aantal prompt gamma's die gelijktijdig met de annihilatiefotonen worden uitgezonden. Ze hebben een hogere positronenergie en vanwege het grotere positronbereik kan er interferentie zijn met het magnetis-

che veld van de MR in vergelijking met ^{18}F. Daarom is het relevant om de prestaties van PET/MR te bepalen voor deze klinisch relevante en commercieel beschikbare radio-isotopen.

In dit doctoraatsproefschrift werd de impact afgeleid van het gebruik van verschillende PET-isotopen via de National Electrical Manufacturers Association (NEMA)-testprestatie-evaluatie van de geïntegreerde PET/MR van GE Signa. De methoden werden onderverdeeld in drie nauw verwante categorieën: NEMA-prestatiemetingen, systeemmodellering en evaluatie van de beeldkwaliteit van de nieuwste klinische PET-scanners. NEMA-prestatiemetingen voor het karakteriseren van ruimte-lijke resolutie, gevoeligheid, beeldkwaliteit, nauwkeurigheid van demping en verstrooiingscorrecties (IQ) en ruisequivalente telcadans (NECR) werden uitgevoerd met behulp van klinisch relevante en in de handel verkrijgbare radio-isotopen. GATE Monte Carlo-simulatie werd gebruikt voor het modelleren van een realistisch General Electrics (GE) Signa geïntegreerd PET/MR-systeem. De simulatie werd gevalideerd met het resultaat van de NEMA-metingen (gevoeligheid en NECR). Monte Carlo-simulaties werden geïmplementeerd in GATE en uitgevoerd in de supercomputer *Vlaams Supercomputer Centrum* geïnstalleerd aan Universiteit Gent. Het systeem heeft een axiaal en transaxiaal gezichtsveld van respectievelijk 25 cm en 60 cm, LYSO scintillatoren met kristalelementen van 25 x 4,0 x 5,3 mm^3, een energievenster van 425-650 keV en een coïncidentie venster van 4.57 ($\pm$2.29 ns). De geometrie werd gemodelleerd met behulp van het cilindrische PET-systeem in GATE, rekening houdend met de afscherming door schuim, kunststof en koper tussen het gezichtsveld en de detectoren. Om het effect van het 3T MR-veld op het positronbereik te karakteriseren, hebben we puntbronnen van positron-emitterende radionucliden gesimuleerd, waaronder ^{18}F, ^{11}C, ^{15}O, ^{13}N, ^{82}Rb en ^{68}Ga gepositioneerd in het midden van een homogene 20 x 20 x 20 cm^3 kubus met verschillende weefselmedia (zacht weefsel, longweefsel en bot).

Voor de evaluatie van de beeldkwaliteit van de state-of-the-art van klinische PET-scanners werd een ruisreductiestudie met behulp van een Bayesian Penalized-Likelihood reconstructie-algoritme op een time-of-flight PET/CT-scanner uitgevoerd. De prestaties en het klinisch gebruik van een block sequential regularized expectation maximization

(BSREM) penalized-likelihood reconstructie-algoritme werden vergeleken met het ordered-subset expectation maximization (OSEM) algoritme met volledige modellering van PSF- en TOF-informatie voor beide algoritmen. Het NEMA IQ-fantoom en een volledig lichaam patiëntenstudie werden verkregen op een GE Discovery MI PET/CT 3-ringensysteem (axiale FOV van 15 cm) in lijstmodus en verschillende datasets met verschillende geluidsniveaus werden gegenereerd. Fantoomgegevens werden geëvalueerd met behulp van vier verschillende contrastverhoudingen (8:1, 6:1, 4:1 en 2:1). Deze werden gereconstrueerd met behulp van BSREM met verschillende β-factoren van 300–3000 en met een klinische instelling die werd gebruikt voor OSEM inclusief point spread function (PSF) en time-of-flight (TOF) informatie. Zowel fantoom- als patiëntgegevens werden geanalyseerd met betrekking tot contrasthersteL (CR), afwijkingscoëfficiënt in de achtergrond (COV), contrast-tot-ruisverhouding (CNR), SUV-verhouding, metabolisch actieve tumorvolumes (MATV's) en signaal-tot-ruis verhouding (SNR). Deze studie had tot doel verschillende β-factoren te evalueren in vergelijking met een klinisch post-filter kernel voor verschillende datasets met verschillende geluidsniveaus om te onderzoeken of en in welke mate ruis kan worden verminderd door BSREM te gebruiken in plaats van OSEM.

De uitkomst van dit proefschrift stelt clinici in staat om de PET-dosis te verlagen, hetgeen vooral relevant is voor jonge patiënten. Bovendien zal het Monte Carlo-simulatieplatform voor PET/MR ontwikkeld voor dit doctoraatsproefschrift natuurkundigen en ingenieurs in staat stellen om geïntegreerde PET/MR-systemen beter te begrijpen en te ontwerpen. Voor enkele resterende kwesties zullen suggesties voor toekomstig onderzoek worden gepresenteerd in het laatste hoofdstuk.

List of Abbreviations

^{18}F-FDG	2-deoxy-2-(^{18}F)fluoro-D-glucose
ANN	Artificial neural network
bp	Bed position
BSREM	Block sequential regularized expectation maximization
CR	Contrast Recovery
CT	Computed tomography
DTPA	Diethylene Triamine Penta Acetic acid
fMRI	functional magnetic resonance imaging
FOV	Field-of-view
FWHM	Full width at half maximum
GATE	Geant4 Application for Tomographic Emission
GE	General Electric Company
Geant4	GEometry ANd Tracking

LBS	Lutetium-based scintillator
LOR	Line of response
MATVs	Metabolic active tumor volumes
MC	Monte Carlo
ML	Machine learning
MLEM	Maximum likelihood expectation maximization
MR	Magnetic resonance
MRS	Magnetic resonance spectroscopy
NECR	Noise equivalent count rate
NEMA	National Electrical Manufacturers Association
NMR	Nuclear magnetic resonance
OSEM	Ordered subset expectation maximization
PET	Positron emission tomography
PSF	Point spread function
PSMA	Prostate Specific membrane antigen
ROI	Region of interest
SiPM	Silicon-Photomultiplier
SPECT	Single-photon emission computed tomography
SUV	Standardized uptake value
TOF	Time of flight
VOI	Volume of interest

Contents

1 Introduction

Several topics that will be covered throughout the course of this thesis are introduced. The basic concepts of anatomical-structural and molecular-functional medical imaging are presented in this chapter.

1.1 Medical imaging

In this section, a short description is given of the two main categories of imaging modalities available today: structural (or anatomical) and functional. First, imaging modalities that mainly provide anatomical and structural information of organs and tissues but are limited in their ability to provide physiological information, such as X-ray radiography, Computed Tomography (CT), Magnetic Resonance Imaging (MRI), and Doppler Ultrasound. The second class of medical imaging modalities primarily provides functional and molecular information of tissues, e.g. the density of specific cell types, proteins, etc or the interaction of drugs. This group includes e.g. functional MRI (fMRI), ultrasound, and the two main nuclear imaging modalities: Positron Emission Tomography (PET) and Single Photon Emission Computed Tomography (SPECT).

X-Ray Radiography

An X-ray is a form of high energy (100 eV to 200 keV) electromagnetic radiation with a short wavelength capable of penetrating solids and ion-

izing matter. As they are used for clinical purposes, X-ray beams are emitted from an X-ray source and directed toward a detector (a film placed behind the patient's body). When passing through the body, parts of the beam are absorbed and scattered (due to different densities of the body) and parts of transmitted X-rays are detected, resulting in a 2D projected image. This is related to the total absorption through the path and shows a superposition of bony structures and soft tissue. An example of a typical X-ray of different parts of the body is shown in Figure 1.1.

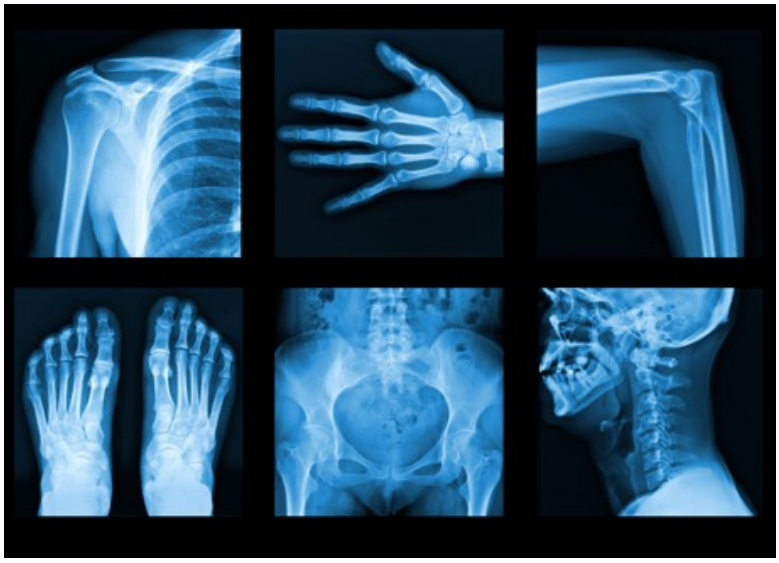

Fig. 1.1: X-ray imaging. The X-rays pass through the body and are attenuated by high-density internal structures, which is visualised here by white intensities as a measure of high X-ray attenuation. Image obtained from [1].

There are clinical applications for X-rays, but the most used are for orthopaedic applications and lung diseases. On the other hand, mammography uses X-ray radiography to detect breast cancer and there are several applications in fluoroscopy (interventional radiology). X-ray imaging can also be used in combination with contrast agents to view the digestive processes (oral administration) or blood flow (intravenous administration). A typical example is a cardiac angioplasty. It uses fluoroscopy with a contrast agent to guide an internally threaded catheter

to help open clogged arteries [2].

This technique depicts a 2D image of a body region, and only from a single angle. This produces a superposition of densities, which represents major limitations in the analysis of what needs to be investigated. Recent medical imaging technologies produce data that are integrated and reconstructed to produce 3D images without superposition. Despite the recent developments, X-ray radiography is still widely used due to its low radiation dose.

Computed Tomography

Computed Tomography, most commonly known as CT, is based on the same principle as X-ray imaging. A narrow X-ray beam is scanning the patient with a radiation detector on the opposite side of the patient. This process generates 2D images at different angles that are used to form a 3D image of the body, using an image reconstruction algorithm (see Section 2.2).

CT serves a similar purpose as an X-ray, but it provides much more information, and it has a higher contrast compared to conventional X-ray imaging (see Figure 1.2). CT is frequently used in diagnosis, monitoring and treatment planning (especially for radiotherapy treatment planning). Because of its widespread availability and excellent system performance, CT has become the modality of choice for most institutions for the work-up of different diseases and an easier tool for initial cancer evaluation [3].

On the other hand, the patient is exposed to radiation. The more of the patient's body that is scanned, the more radiation they are exposed to. Even though CT-scanners are designed to minimize the radiation dose while generating acceptable image quality, the total radiation exposure is considerably higher than for X-ray radiography. Moreover, compared to MRI, X-ray based methods offer relatively low soft-tissue contrast.

Ultrasound

In ultrasound imaging, high-frequency acoustic pulses are sent into the body reflecting at discontinuities such as the boundary between differ-

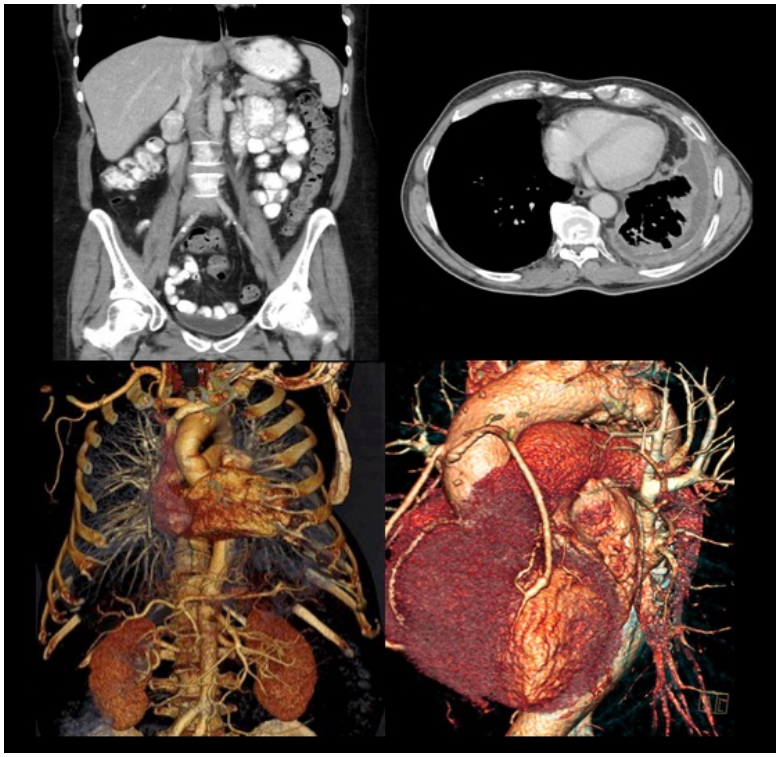

Fig. 1.2: A CT scan of the chest and abdomen. At the bottom, the two images are a 3D rendering and the aper pictures are cross-sectional slices through the 3D image. Note that the principle is the same as X-ray imaging, but with more detailed information.

ent tissues. As the ultrasound waves pass through the tissue and are reflected back, local images can be created and tissues can be characterized. These local images can be reconstructed (in 2D and 3D) by measuring the time delay and the intensity of the reflected pulses. Ultrasound is also useful for the non-invasive imaging of the abdomen and pelvis, including imaging the fetus during pregnancy (see Figure 1.3).

Although other techniques give more detail and accuracy, ultrasound is still very commonly used because the instruments are relatively cost-effective, quick to perform and it emits no ionizing radiation.

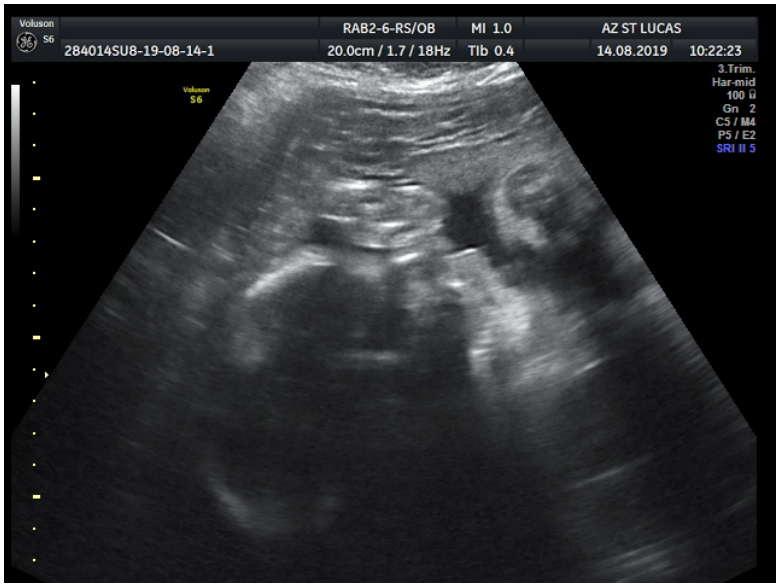

Fig. 1.3: An example of an image obtained by ultrasound, an "echo" of my lovely daughter **Esther Caribé** with 32 weeks of life.

Magnetic resonance imaging

Magnetic resonance imaging is a non-invasive biomedical imaging technique based on nuclear physics with a high spatial resolution (>0.1 mm) and different contrast weightings. MR image is based on the measurement of the emitted radio signal by protons exposed to the magnetic field and excited by radio waves and on the differences in relaxation times between protons, which are induced by the underlying distribution of hydrogen atoms and the magnetic susceptibility of surrounding tissues in the body [2, 4].

An MR image allows us to distinguish different soft tissues much better than any other modality, including the difference between normal and pathological soft tissue, with a very high resolution, and without exposing the patient to ionizing radiation. Some of its most common applications are in neurological and musculoskeletal imaging. It also allows the integration of many different imaging features such as anatomy, physiology, metabolism and function. The main drawback of MR imaging nowadays is its high maintenance cost. Part of this thesis will focus

on the system characteristics and improvement of image quality of an integrated PET/MR, allowing simultaneous PET and MR imaging measurement, so we will discuss this modality more in detail in the following chapters.

Nuclear imaging modalities

Nuclear imaging modalities allow the *in-vivo* measurement of biological processes at the cellular and molecular levels [4]. Like X-ray and CT modalities, it makes use of ionizing radiation. However, instead of having a radiation beam going through the patient, a small amount of radioactive isotope is injected into the patient's bloodstream and the photon emissions as a result of the radioactive decay are measured and used for imaging. By combining this radioactive isotope with a molecule with binding affinity and high selectivity for a specific target, many different cellular function parameters can be assessed. As such tumours can be detected and located, blood flow can be measured and many more applications. In Section 2.1.2, an overview is given of the most common and widely used diagnose and radiotherapeutic tracers.

PET and SPECT

The two main nuclear imaging techniques used for the detection of gamma radiation are Positron Emission Tomography (PET) and Single-Photon Emission Computed Tomography (SPECT). In the case of PET imaging, the radioisotopes decay emitting positrons (β^+). The most widely and clinically used positron emitter is ^{18}F, which almost exclusively decays via β^+ (see Tables 2.1 and 2.2). When the positron is emitted, it travels for a few millimetres through the body until it interacts with a free-electron resulting in an annihilation and producing two back-to-back gamma photons with energy of 511 keV each (these photons are emitted in almost opposite direction starting from the interaction point, see section 2.1.4 for more) defining a line through the patient along which the annihilation event must have occurred. Since PET is based on the coincident detection of these two opposite gamma photons along the line-of-response (LOR), a pair of detectors is needed (clinical PET systems use a full ring of detectors surrounding the pa-

tient). If the two back-to-back gamma photons are detected within a certain short time window (depending on the PET system settings) it is assumed that they originate from the same annihilation event. This information is saved in sinograms or list-mode that can be used to reconstruct 3D images of the distribution of the PET tracer in the body. However, a drawback of PET is the positron range and non-collinearity of the two annihilation photons, which constitute physical limitations on the image quality of PET (see Chapter 4). Section 2.1 will provide a full and detailed background of PET systems for the main chapters of this thesis.

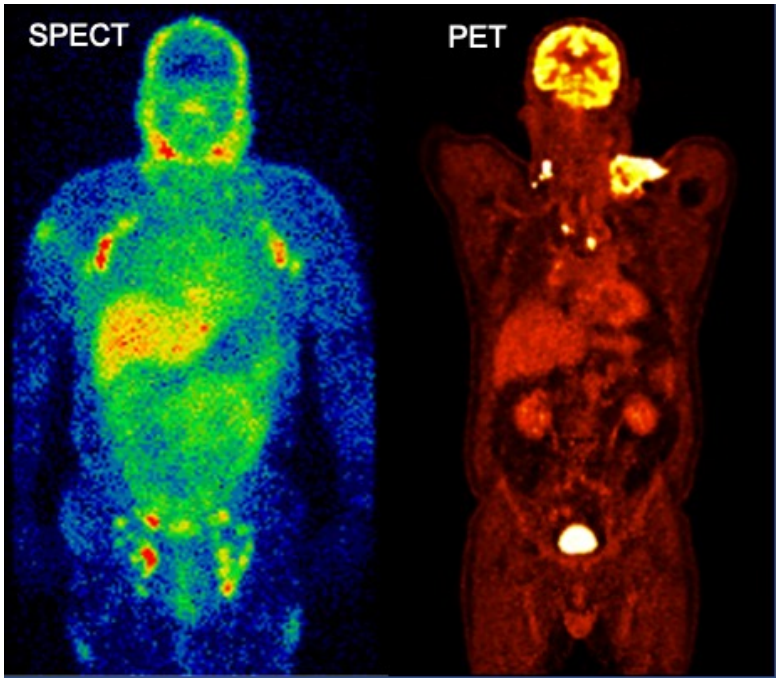

Fig. 1.4: An example of a coronal whole-body SPECT and PET image showing the radiopharmaceutical distribution in the body. Note that SPECT imaging yields a relativity low image resolution (typically around 10 mm in clinical systems) compared to PET imaging

Compared to PET systems, SPECT is based on the detection of a radioisotope that emits gamma photons (γ), which are directly emitted upon a nuclear de-excitation of one of the short-lived excited nuclei. Because of its physical properties (141 keV and half-life of 6.02 hours),

^{99m}Tc is the most commonly used SPECT radioisotope (predominantly in bone and brain scans). Both PET and SPECT system detectors use a scintillator coupled through a light guide to a photodetector. The general propose of the scintillation is to stop the gamma rays and convert the absorbed energy into visible light (wavelength of light from 380 nm to 780 nm). Subsequently, the absorbed energy is collected by the photodetector and converted into an electrical pulse. Each modality uses a dedicated scintillation based on the range of energies of the radioisotope (see 2.3). PET radioisotopes have a gamma photon energy of 511 keV, while in SPECT, the energy varies (depending on the radioisotope) from 110 keV to >350 keV. The energy of the gamma photo and scintillator material used (in case of SPECT, also the collimator design), have a significant impact on the spatial resolution. Moreover, the different radiotracers to which PET and SPECT are sensitive (dual gamma-emission per nuclear decay for PET and single gamma-emission per nuclear decay for SPECT) will also determine the type of system geometries used. Instead of using a full ring of detectors around of the patient, SPECT systems may consist of one to three rotating detectors, but normally there are only two detectors fixed at 90° or 180° on a rotating gantry (there are several SPECT systems with singular configurations specially designed for specific organs). Each rotating detector has a collimator positioned in front of the scintillation crystal designed to attenuate all but the near-perpendicularly incident gamma photons, where are used to record 2D images of the radioactivity (see Figure 1.4). By rotating the detector heads around the patient, 3D images of the radiopharmaceutical distribution in the body can be obtained.

The most important advantage of PET imaging over SPECT is that of exhibiting a much higher sensitivity (approximately 10^2 to 10^3 times higher). This is because the collimator attenuates photons that are not within a small angular range (see Figure 1.5).

Regarding the image resolution, PET scanners have an almost 4 times higher image resolution (about 2.5 – 4.0 mm in current clinical systems) than standard SPECT scanners (typically around 10 mm) [4, 5]. In addition to its clinical role, PET and SPECT continue to play a major role in the biomedical research community. Rapid growth is now occurring in the number and diversity of PET and SPECT molecular

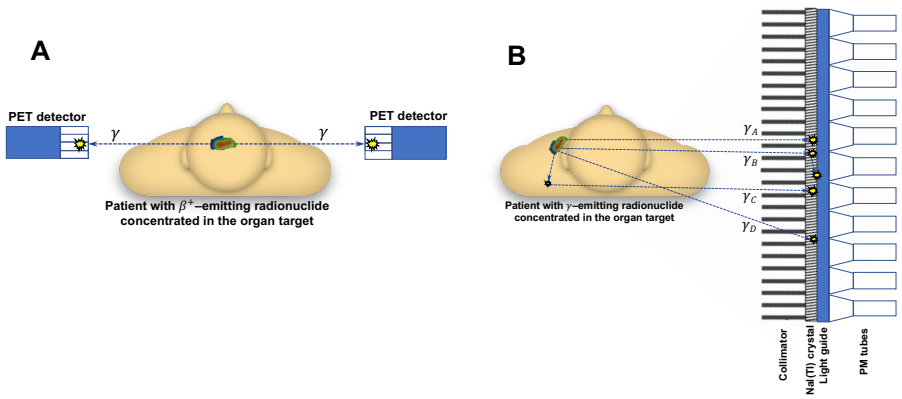

Fig. 1.5: ***A*** General schematic diagram of a PET coincidence detection of a dual-photon emission per nuclear decay. ***B*** Illustration of different types of events that may be detected by a gamma camera. Yellow stars indicate locations of gamma ray interactions.γ_A, Valid event. γ_B, Detector scatter event. γ_C, Object scatter event. γ_D, Septal penetration.

imaging tracers targeted to specific proteins and molecular pathways implicated in disease [5].

Multi-modalities imaging

The combination of multiple imaging modalities can substantially increase the benefit for physician and patient. Nowadays PET scanners, and a rapidly growing number of SPECT systems, are sold with an integrated CT scanner in combined PET/CT and SPECT/CT configurations. These systems enable the correlation of structure (CT) and function (PET or SPECT), yielding better diagnostic insight in many clinical indications. The CT data can furthermore be used to apply a correction for attenuation and scattering of the photons [5]. In the case of SPECT/CT, the main advantage is the increased specificity achieved through a more precise localization and characterization of functional findings. Another advantage is the shorter overall patient setup, image time and therefore the patient throughput [4], (Section 2.3 shows an overview of the currently most used hybrid systems).

On the other hand, the performance of PET/CT systems will always be limited by the low soft-tissue contrast of the CT and by the organ

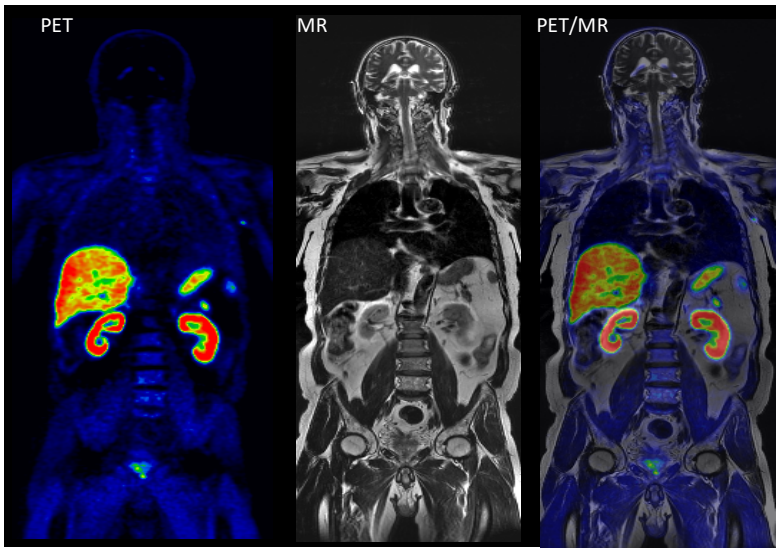

Fig. 1.6: A coronal whole-body PET, MR imaging and PET/MR image comparing the ^{18}F choline prostate imaging (55 min uptake and 6 bed positions). Note that the integrated PET/MR provides superior soft tissue contrast for oncological applications such as prostate cancer (*Courtesy University Hospital Zurich*).

motion artefacts [2, 4]. Therefore, the combination of PET with MRI provides several oncological applications (see Figure 1.6), such as brain tumour evaluation with ^{11}C-acetate and ^{68}Gallium-DOTA-D-Phe1-Tyr-octreotide (^{68}Ga-DOTATOC) as radiotracers, prostate cancer with ^{11}C-choline PET and accurate correction of motions artefacts. All of this can be done without the use of additional radiation dose to the patient. Chapters 3 and 4 will discuss the technical challenges of PET/MR compared to PET/CT systems because of interferences between the PET and MR imaging system and its impact on the imaging of different PET radioisotopes.

1.2 Outline

The essential background for this dissertation is presented in **Chapters 1 and 2**, We start with a brief history of the medical imaging modalities, followed by a detailed explanation of the differences between these

modalities. Since this work evaluates image quality and reconstruction parameters in recent hybrid systems, we go into more details on the PET system performance parameters and the important characteristics to be considered, with particular emphasis on NEMA performance measurements for different radioisotopes. Subsequently, a detailed explanation of the physics of positron emission, the PET scanner and PET image degrading effects are presented. Next, we explain the basics behind several techniques used throughout this thesis: image reconstruction, acceptance tests for PET and system modelling using GATE Monte Carlo simulations.

In **Chapter 3**, we present the important aspects of a fully integrated PET/MR system performance characteristics and the impact of using different radioisotopes. NEMA NU 2–2007 performance measurements are performed for characterizing the spatial resolution, sensitivity, image quality, and the accuracy of attenuation and scatter corrections for ^{18}F, ^{68}Ga, and ^{90}Y. Scatter fraction and noise equivalent count rate tests are performed using ^{18}F and ^{68}Ga. Subsequently, we report the effect of the 3T MR field on spatial resolution and sensitivity. Next, the impact of different reconstruction parameters on image quality and peak NECR are evaluated and discussed.

In **Chapter 4**, a realistic Monte Carlo model of the integrated GE Signa PET/MR is implemented in GATE to simulate NEMA sensitivity and NECR measurements. We first give a full description of the different components of the PET/MR geometry, the physics and the radioisotope sources used in this study. The NEMA sensitivity and NECR results reported in chapter 3 are used to validated the GATE PET/MR Monte Carlo model. Further, we use this model to predict the performance of PET/MR for the radioisotopes ^{18}F, ^{11}C, ^{15}O, ^{13}N, ^{82}Rb and ^{68}Ga and to evaluate the effect of the 3 T MR field on positron range in different tissue types such as lung, soft tissue, cortical bone and for tissue boundaries.

In **Chapter 5**, the resolution, noise and quantitative accuracy of the state-of-the-art PET/CT are evaluated using different reconstruction methods. The NEMA IQ phantom and a whole-body patient study are acquired in list-mode on a GE Discovery MI PET/CT which have 3 rings of detectors and 15 cm axial FOV PET system. Different datasets

with varying noise levels are generated. Phantom data are evaluated for four different contrast ratios (8:1, 6:1, 4:1 and 2:1). These are reconstructed with a block sequential regularized expectation maximization (BSREM) algorithm using different β-factors and with a clinically used ordered-subset expectation maximization (OSEM) algorithm including point spread function (PSF) modelling and time-of-flight (TOF) information. Contrast Recovery (CR), background noise levels and contrast-to-noise ratio (CNR) are used to determine the system performance using the phantom data. Findings based on the phantom data are compared with clinical data to confirm whether and to what extent noise can be reduced by using BSREM instead of OSEM. The results obtained from this image quality evaluation are presented and discussed at the end of this chapter.

Finally, in **Chapter 6**, we give an overview of the most important results of this dissertation, along with a conclusion and some future perspectives.

2 Background

A general overview is presented of medical imaging to provide the reader with enough background knowledge to understand the topics that will be studied in this thesis. We start with the concept of positron emission tomography (PET), magnetic resonance imaging (MR), the basics physics involved, and the various parameters that contribute to the image quality. This is followed by a description of the National Electrical Manufacturers Association (NEMA) performance measurements for PET scanners. Finally, section 2.5 is dedicated to Monte-Carlo simulations.

2.1 Positron Emission Tomography

PET has proven a very valuable imaging tool to explore a variety of cellular and molecular processes *in-vivo*. Because of its high sensitivity, only very low amounts of a PET tracer (a compound labelled with a PET isotope) need to be administered and therefore pharmacological effects and physiological changes are avoided. This way, PET can provide images with high contrast and quantitative functional information about the disease state or therapy response, complementary to information provided by anatomical imaging modalities such as CT or MRI (see Figure 1.6).

A typical PET study involves the intravenous injection of a PET tracer, which is delivered by arterial blood flow to the target tissue.

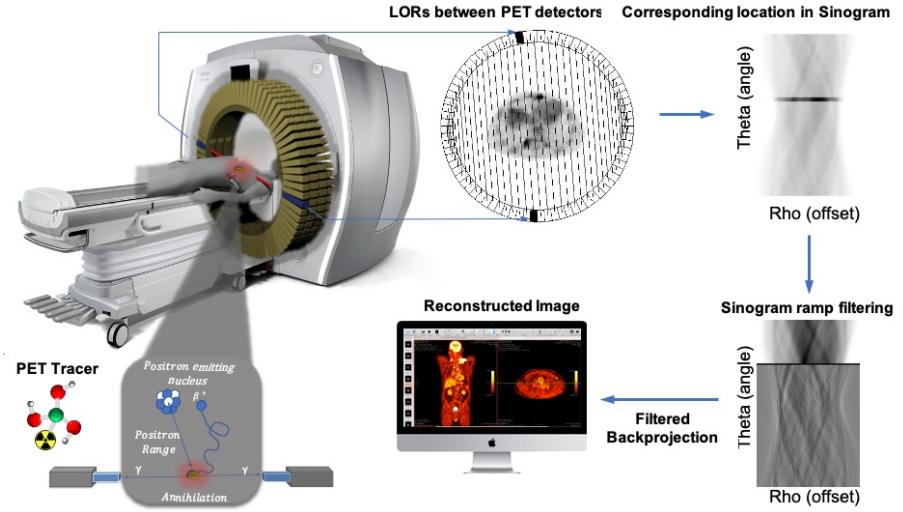

Fig. 2.1: The principle and workflow of positron emission tomography: After producing an appropriate PET tracer and the radiotracer injection, positrons are emitted within the subject's body, combine with nearby electrons and annihilate. The result is a pair of 511 KeV gamma photons released in opposite directions. PET scanners use pairs of radiation detectors to measure the nearly simultaneous, coincident interaction of the 511 KeV photons. The data recorded by the scanner is a collection of coincidence detections. In the reconstruction step, a mathematical procedure is implemented to convert the acquired data to tomographic images

While the PET tracer binds (ir)reversibly to or is being trapped by its physiological target, the radioactive label will decay, emitting a positron which will annihilate with a nearby electron resulting in two simultaneous 511 keV photons in opposite direction. These photon pairs are detected by the PET scanner as a pair of coincident detections within a predefined timing window (about 4.9 ns for almost all commercial PET scanners available today) such that the line on which the annihilation occurred-the so-called line-of-response (LOR), can be determined (see Figure 2.1). During the acquisition of the scan emission data, physical effects such as attenuation, scatter, dead time and detector response can happen. The acquired data are then, (most often) corrected during the reconstruction process. There are two widely used reconstruction algorithm methods: analytical or iterative (see Section 2.2).

This way a 3D image of the radiotracer distribution in the body is

generated at one or various time points after tracer injection. Combined with the activity level in the arterial blood and percentage of intact tracer in arterial plasma, this temporal and spatial distribution of radiotracer concentration allows accurate quantification of the underlying physiological tissue characteristics such as blood flow, metabolism, cell proliferation, receptor density or enzymatic activity.

More details on the physics, radiopharmaceutical production, instrumentation and image reconstruction of PET can be found in the following sections.

2.1.1 Physics of nuclear medicine imaging

Nuclear medicine imaging uses ionizing radiation, which is capable of carrying and depositing energy when interacting. There are different types of ionizing radiation, which interact differently with matter. The principal forms and the basics of ionizing radiation found in most imaging modalities available in a modern hospital will be briefly introduced in the following sections.

Radiation forms in nuclear medicine

Radiation is an energy carrier and when it propagates in a medium, it can interact with the constituent atoms of that medium. The interaction occurs through a process of energy transfer from radiation to the medium. This transfer process, in turn, varies greatly and can be affected by many factors, such as the type of radiation, its energy, the type and density of the environment, among others.

β particle radiation

There are two types of beta particles radiation: β^- (*beta-minus*) and β^+ (*beta-plus*). In this section, we conveniently choose to discuss only the β^+ decay because of the PET imaging formation. The β^+ (or positron) is the antiparticle of the electron, which has the same mass and the same but positive charge. It originates from a nuclear process in which a proton (p) of the nucleus becomes a neutron (n). This process can be expressed by the Eq 2.1:

$$ {}^{1}_{1}\beta \longrightarrow {}^{1}_{0}\, n + {}^{0}_{1}\, \beta^{+} + \nu_{neutrino} \tag{2.1} $$

A second particle is emitted, which is a neutrino. As the daughter nucleus has an atomic number one less than the parent, one electron is also ejected through an internal conversion from the daughter nuclei to balance charge. Positron emitting nuclei may also decay by electron capture. β^{+} radiation is mainly used in nuclear medicine for PET imaging. The most widely used radioisotope for PET imaging is ^{18}F (fluorine-18). It has a positron emission branching ratio of 96.86 % with a 0.6335 MeV of maximum positron energy. The other 3 % of decays via electron capture.

Annihilation radiation

Annihilation radiation is the foundation of PET imaging modality. After a positron is ejected from the nucleus, it loses its kinetic energy in collisions with atoms of the surrounding body tissues until it collides with an electron. The combination of these particles momentarily forms a metastable "atom" called *positronium*, which exist for around 10^{-10} seconds. By an annihilation reaction their mass is converted into energy (see section 2.1.4, Figure 2.9). In the form of two photons of 511 keV (rest mass of e^{-} and e^{+}) travelling in opposite directions to allow for conservation of energy and momentum. Because the rest-mass energy of an individual particle is 511 keV, the total transition energy of 1.022 MeV is required [4]. At the time of annihilation, the positronium has a residual momentum, which leads to the non-collinearity of the two annihilated photons (a degradation factor in PET systems performance). This will be discussed in detail in section 2.1.4.

γ radiation

γ photons are an important form of electromagnetic (EM) radiation. It consists of photons with wavelength below 3×10^{-11} m and energy greater than 41.4 keV (which is capable of causing ionization when interacting with the atoms of the environment). Unlike X-rays, γ rays result from nucleus process such as spontaneous nuclear decay. Despite

different origins, X-ray and γ ray are essentially high energy photons. γ rays emission have a characteristic energy determined by the difference in energy levels between the initial and final state of the nucleus [4, 6].

X-ray radiation

Another type of EM radiation are X-rays. In an X-ray medical device, an X-ray tube is used to produce X-ray radiation. By applying a strong potential difference (from 20 kV to 100 kV) between a cathode and anode, electrons are accelerated across at very high speed from the cathode to the anode. X-rays are produced by colliding electrons with the atoms in a metallic anode target. There are two particular radiation types coming from this particular event: Bremsstrahlung (with a continuous energy spectrum) and characteristic X-rays (present in the spectrum as several peaks). Bremsstrahlung is caused by the deceleration of the emitted electron in the electromagnetic field (by electrostatic attraction) of the nucleus. When a charged particle (e^-) is decelerated, X-ray radiation is emitted. The maximum X-ray energy (which depends only on the potential difference applied) is defined as $E_{max} = eV_{Tube}$, where V_{Tube} is the potential difference between the anode and cathode.

Differently of Bremsstrahlung radiation, the characteristic X-rays are produced when an electron of the outer shell loses energy to fill the hole when is released by the absorption of an X-ray. The frequency of a characteristic X-ray is determined by the change in energy level (quantum state) of the electron according to $E = h\nu$. This particular energy value depends upon the anode material used (usually tungsten or molybdenum). For X-ray tubes based on a tungsten anode, there are two particular emissions with energies of 59.3 keV and 67.2 keV. For the anode based on molybdenum (typically used for mammograms), the emissions have energies of 17.5 keV and 19.6 keV. As briefly discussed in 1.1, X-ray radiation has significant importance in the history of the medical image because the fist radiology images were made using X-rays [4].

Interaction of β^+ particles and Photons with matter

The β^+ particle loses kinetic energy through interactions with the surrounding matter (tissue, in case of the human body). The distance from the positron-emitting nuclei to the point of annihilation is called the positron range (see subsection 2.1.4, Figure 2.9) [4, 7]. It also indicates the location of the radiation origin.

Contrary to β particles, photons can pass through material without or with only few interactions. As a result, photons are more difficult to stop than particles. *Rayleigh scattering*, *photoelectric effect*, *Compton effect*, and *pair production* are the most common interactions of photons with matter. Predominating interactions according to the photon energy and atomic number are shown in Figure 2.2.

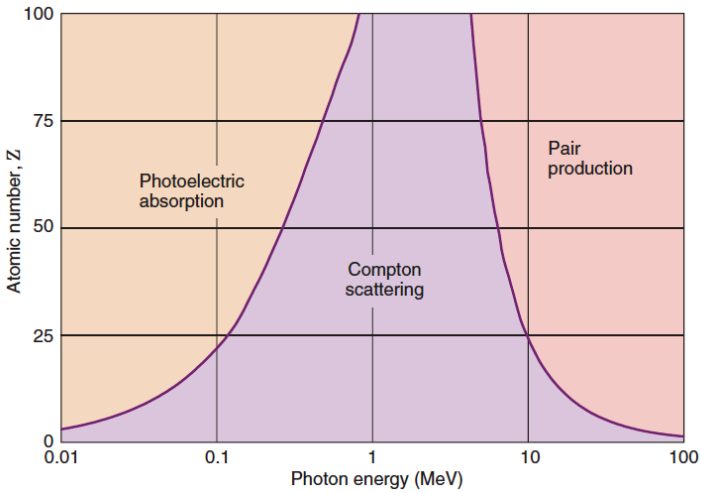

Fig. 2.2: Dominance of effects according to photon energy and atomic number of the material. Rayleigh scattering is not represented as it is not significant in nuclear medicine imaging. Image obtained from [4].

- The *Photoelectric effect* corresponds to the interaction of photons with electrons in the higher energy shells of the atom. The incident photon transfers all of its energy to the electron, which is released by the atom. The removal of an inner electron brings the atom in an excited state. The excited atom returns to the ground state

by emitting a characteristic X-ray or by releasing another electron, which is called an *Auger* electron. The probability of this process (σ_{PE}) decreases with increasing photon energy (E_γ) but increases with the increasing atomic number (Z) of the material. The following approximate relationship holds:

$$\sigma_{PE} \propto \frac{Z^3}{E_\gamma^3} \tag{2.2}$$

The photoelectric effect is predominant in human tissues at energies below approximately 100 keV (see Figure 2.2) and is crucial for X-ray and CT imaging where attenuation of photons in the bones (high density tissues) is the source of the image contrast.

- The *Compton effect* corresponds to the interaction of the photon with the electron in one of the lowest energy shells. This effect is predominant in human soft tissues at energies between 100 keV and 2 MeV. The potential energy of the electron is very low compared to the photon energy and can be considered as negligible. After the interaction, the photon is scattered and the electron is released from the atom. The energy lost by the photon comprises the binding energy of the electron and the kinetic energy it acquires. The transferred energy does not depend on material properties or electron density. The scattered photon can interact again with the matter by either the Compton effect or photoelectric effect, or simply not interact with the matter again. The scattering angle is dependent on the energy loss of the photon ($E_\gamma^{'} = E_\gamma - K_{kineticE}$), and can be expressed as:

$$E_\gamma^{'} = \frac{E_\gamma}{1 + \frac{E_\gamma}{m_e c^2}(1 - \cos(\theta))} \tag{2.3}$$

Where $m_e c^2$ is the total rest mass energy of an electron. Compton scattering is of prime importance to radiobiology, as it happens to be the most probable interaction for the gamma rays and high-energy X-rays used in radiotherapy [6, 7].

- The *Pair production* refers to the production of an elementary particle and its antiparticle. Due to the energy conservation, this process can only happen when the photon has an energy equal to the total mass-energy of the two particles ($2m_e c^2$). This minimum energy is 1.022 MeV to produce an electron-positron pair. As shown in Figure 2.2, *Pair production* becomes especially relevant at high energies and in the presence of heavy nuclei, as its probability, or cross-section, is dependent on the energy of the photons and the atom's atomic number, according to Equation 2.4:

$$\sigma_{pair} \propto Z \ln(E_\gamma) \tag{2.4}$$

- The *Rayleigh scattering* consists of the electromagnetic wave passing near the electron and setting it into oscillation. The oscillating electron irradiates the energy at the same frequency as the incident electromagnetic wave. These scattered x-rays have the same wavelength as the incident beam. This effect predominates at energies less than 50 keV. This scattering is of interest for low-energy (or dual-energy) CT imaging. Because *Rayleigh scattering* is never the dominant process in interaction of photons with matter, is of little to no importance in nuclear medicine and, particularly, PET imaging.

2.1.2 PET radionuclides

In nuclear medicine, radiopharmaceuticals are unique medicinal formulations containing radioisotopes which are used in major clinical areas for diagnosis and (or) oncology therapy. Knowing the physical characteristics of the commercially available PET radioisotopes is a key to the radiopharmaceutical preparation.

The choice of radioisotope for a particular application is therefore dependent on many factors. For diagnostic imaging applications, for example, the imaging modality (gamma or a positron emitter), the biological half-life (i.e. the time that it takes for half to be removed by biological processes) should be in line with the physical half-life of the radionuclide used. On the other hand, the therapeutic application is

Tab. 2.1: Properties of pure positron emission radioisotopes. Data from the National Institute of Standards and Technology [8], Laboratoire National Henri Becquerel [9], and Brookhaven National Laboratory [10]. Range of positrons (R) is in water [11].

Isotope	Half-life	Branching β^+ (%)	E_{max} (MeV)	E_{mean} (MeV)	R_{max} (mm)	R_{mean} (mm)
^{18}F	110 min	96.9	0.634	0.250	2.4	0.6
^{11}C	20.4 min	99.8	0.960	0.386	4.2	1.2
^{13}N	10 min	99.8	1.119	0.492	5.5	1.8
^{15}O	2 min	99.9	1.732	0.735	8.5	3.0

Tab. 2.2: Properties of prompt gamma positron emission radioisotopes. Only the positrons and prompt gammas with the two highest branching ratios are listed. Data from the National Institute of Standards and Technology [8], Laboratoire National Henri Becquerel [9], and Brookhaven National Laboratory [10].

Isotope	Half-life	Branching β^+ (%)	β^+ E_{max} (MeV)	Branching γ (%)	γ E (PG) (MeV)
^{68}Ga	67.8 min	87.7, 1.2	1.899, 0.821	3.2	1.077
^{82}Rb	1.3 min	81.8, 13.1	3.378, 2.601	15.1	0.777

mainly dependent on the physical properties of the radionuclide, such as emitted energy radiation, radioactivity half-life and type of decay (by α or β). As an example, ^{131}Iodine (potassium iodine), ^{90}Y and ^{177}Lu is used to label antibodies and peptides (a short chain of amino acids).

Most positron emitting radioisotopes are cyclotron-produced. Before being suitable for the use in medicine, radioisotopes must be attached to an organic molecule or compound to form a radiopharmaceutical or radiotracer, so that the radioisotopes can be carried to the target place of the examination, through the metabolism of the organic molecule. Some PET isotopes have relevant contribution of prompt gammas, such as ^{68}Ga, ^{82}Rb, ^{90}Y and have complex decay schemes with a variety of gammas in coincidences (see Table 2.2 and Chapter 3 to find out how these high-energy prompt gammas influence the system performance). Others commonly used PET radioisotopes, such as ^{18}F, ^{11}C, ^{13}N, and ^{15}O have short half-lives and high branching ratios for β^+ decay. The

main properties of these radioisotopes are summarized in Table 2.1.

β^--emitting radionuclides are being used more and more in targeted radionuclide therapy. ^{131}I therapy is widely used for thyroid, parathyroid, and salivary glands. The major advantage of ^{131}I are its low price and ready availability. ^{131}I has a physical half-life of 8.04 days and emits by 81% abundance γ photon of 364 keV. The maximum and mean β energy are 0.61 MeV and 0.192 MeV, respectively [12]. ^{177}Lu is another therapeutic radionuclide frequently used for neuroendocrine and prostate tumours. With a maximum β energy of 0.5 MeV and half-life of 2.7 days, ^{177}Lu also emits γ rays at 208 and 113 keV [13].

The administration of ^{90}Y-DOTATOC for treatment of tumours expressing somatostatin receptors has been widely introduced into routine clinical practice. ^{90}Y also has been used in radioembolization for primary and metastatic liver cancer [14]. Radioembolization is a trans-arterial technique that involves the injection of micron-sized embolic particles loaded with a radionuclide.

^{90}Y is mainly a β^- emitter with a very small branching ratio for positron production. In 0.003186% of the decays there will be the emission of an e^+/e^- pair at 1.76 MeV. As the transition energy is 1.76 MeV, Here remains 738 keV of kinetic energy to be split between the electron and the positron in order to conserve the null momentum. With a half-life of 64.1h, ^{90}Y can produce a weak but usable PET signal [6, 15, 16].

The practices of nuclear medicine and radiopharmacy require the preparation of radioactive ligands for injection into patients. Figure 2.3 summarizes the currently used diagnostic and radiotherapeutic tracers.

Practices in radiopharmacy for both industries and hospitals are regulated (in case of the European Union) by the European Medicines Agency (EMA). In Brazil, the radiopharmaceutical production must be attested by the National Nuclear Energy Commission [17] and the National Health Surveillance Agency [18].

With PET becoming more widely used, the transport logistics have allowed faster shipments of radioisotopes to small imaging centres. The majority of PET studies in clinical routine are still being performed with ^{18}F, because of its physical properties combined with efficient transportation logistics which widely increase its availability. The same holds for ^{68}Ge (a long-lived radionuclide used to produce via a generator the

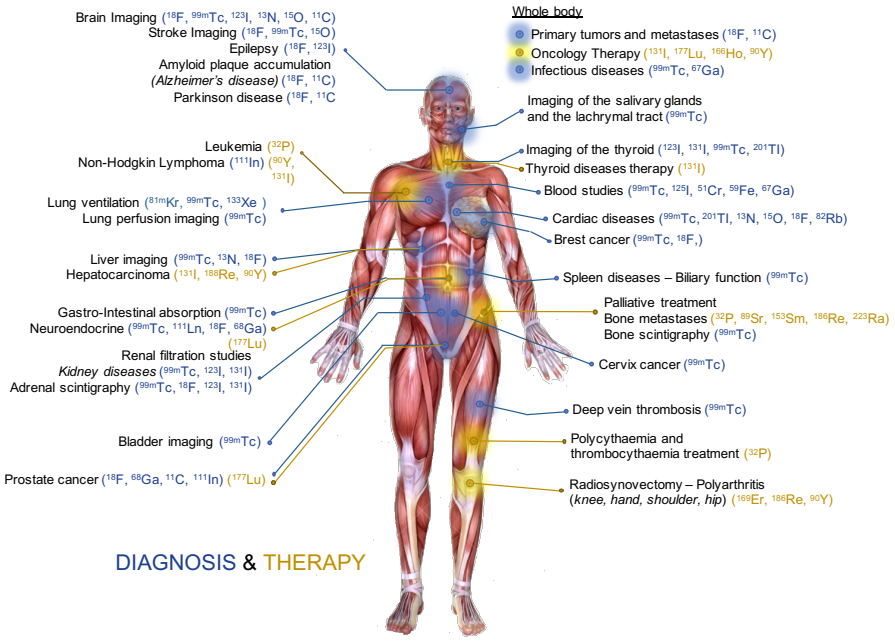

Fig. 2.3: Diagnostic and radiotherapeutic tracers [19].

short-lived radionuclide ^{68}Ga) and ^{90}Y, for which the user is not dependent on the availability of a cyclotron [20].

2.1.3 PET instrumentation

As mentioned before in Section 2.1, PET imaging is based on the detection of gamma radiation. To visualize a specific function with PET, the patient must be injected intravenously with a substance (marked with a positron β^+ emitting radionuclide), which distributes in the body such that it correlates with the function of the organ target. Once the radioisotope has been distributed in the body, the patient is positioned in the PET scanner, which essentially consists of a cylindrical configuration of detector blocks (Section 2.3 shows the most recent commercially available PET systems). The image formation consists of localizing the positron emitter. After its emission, a positron travels a short distance (few mm, depending on the energy of the emitted positron) through surrounding tissue while losing energy. When it has lost sufficient en-

ergy, the positron annihilates with an electron. After annihilation, two 511 keV photons are emitted in (nearly) opposite directions. When two interactions are simultaneously detected within a pair of detectors, it is assumed that an annihilation occurred on the LOR connecting the interactions, as shown in Figure 2.7. By recording many LORs the activity distribution can be reconstructed (see section 2.2).

PET detector: Photon detection with scintillation detectors

The quality of the PET detector has a large impact on image quality. Therefore, an optimum detector performance requires the photodetector to detect scintillation photons as efficiently and accurately as possible. The photodetection efficiency (PDE) is the probability that an incident photon is converted to a measurable signal, at the emission wavelengths of the scintillator.

Scintillators

Scintillation detectors are used in PET scanners as detector elements. They couple inorganic scintillation crystals that emit visible or near-ultraviolet light after interaction with an incident 511 keV photon, to photodetectors that detect and measure the scintillation photons. Then, this information collected by the photodetector is converted into an electrical signal pulse.

The most commonly used PET scintillators are listed in Table 2.3. A detector block generally consists of an array of crystals separated by reflecting material to confine the light in each crystal when an interaction takes place. The crystal size is directly related to the reconstructed spatial resolution, but small crystals may require a significant number of photodetectors to accurately decode the gamma interaction position, and this increases the total cost of the PET system.

Scintillators have several physical properties that affect the efficiency, time, and energy resolutions of PET detectors. The density and atomic number determine the efficiency of the detector, which impacts the detector sensitivity (the fraction of photoelectric and secondary Compton interactions increase with the atomic number). The light yield determines the number of optical photons generated from each gamma-

Tab. 2.3: Scintillators used in PET scanners. Note that decay time determines scanner deadtime and random coincidences rate as well as ability to measure time-of-flight (TOF) PET imaging (discussed in subsection 2.1.3) [21].

Scintillator	Density (g/cm^3)	Light yield (Ph/MeV)	Emission wavelength (nm)	Decay time (ns)	Cost
LSO(Ce) (or LYSO)	7.40	27.000	410	40	more expensive
BGO	7.13	9.000	480	300	expensive
La3Br(Ce)	5.29	61.000	358	35	more expensive
NaI(TI)	3.57	38.000	415	230	cheap (relatively)

interaction within some range (9 ph/keV and 26 ph/keV for BGO and LSO respectively) and determines the time and energy resolution. The decay time determines how fast the luminescence signal decays after a detection. Finally, the emission wavelength is the wavelength of the produced optical photons, which needs to be compatible with the wavelength of the photodetector [4, 22]. The quantum efficiency of the photodetector (QE), is defined as the probability that a photon absorbed in the active area of the photodetector gives rise to a signal, determines the fraction of the produced photons that are converted into electrons in the photodetector.

There are several types of photodetectors, but the most used in a PET detector are photomultiplier tubes (PMT) and silicon-photomultipliers (SiPM) [4, 23]. There is also a new PET detector based on monolithic scintillator crystal that is currently under investigation by the biomedical research community, meant to provide the highest scanner sensitivity possible while still providing a spatial resolution adequate for high-resolution imaging (see subsection 2.1.3).

PMTs

A photomultiplier tube consists of a vacuum tube with a photo-cathode at one end, a series of dynodes at successively higher voltages, and an anode at the other end of the PMT (see Figure 2.4). When the optical photons (visible light) are emitted by the scintillator, the photodetector detects, and by the photoelectric effect, produces electrons that are emitted in the direction of the dynodes. Then these electrons are accelerated by the existing electric field and amplified. The resulting electrical current is proportional to the number of initial scintillation photons and therefore to the energy deposited in the scintillation crystal by the incident photon.

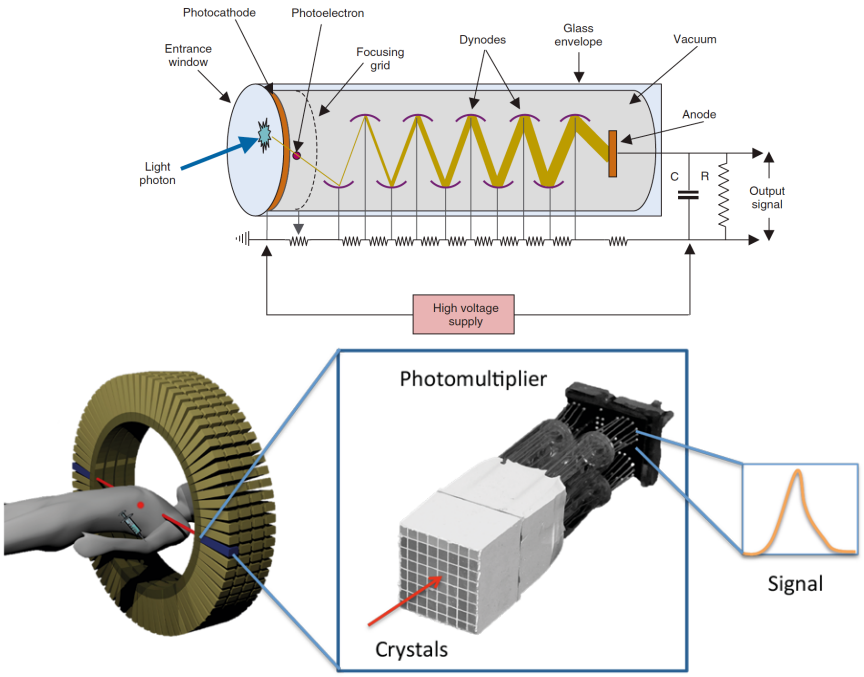

Fig. 2.4: Basic principles of PET imaging: a radioactive tracer is injected into a patient and emits two 511 keV photons after the positron annihilates with an electron. Using a ring design, photons are detected and measured with crystals and photomultiplier tubes (PMTs) surrounding the patient (at the top). Image obtained and edited from [4, 24], under creative commons attribution unported license.

As shown in Figure 2.4, a full PET scanner consists of a cylindrical assembly of block detectors in a ring structure. A block detector consists of small individual scintillation crystals, a few millimetres in size, oriented towards the patient, and tightly packed into blocks, which are typically coupled to four or more small photo-multiplier tubes [4, 25]. The advantage of using this block detector is that PMTs have excellent timing (∼1 ns) and gain properties (∼ 10^6). However, there are some limitations which need to be considered. The QE of a PMT is somewhat poor (from 25% to 43%) [26]. These devices are bulky and operate at high voltages (typically 200-400 V), and the electron multiplication along the dynodes does not function in the presence of electromagnetic fields (this is the main challenge in PET/MR detectors). Several approaches have been applied to solve this challenge. The Siemens Biograph mMR uses avalanche photodiodes (APDs) instead of PMTs in PET detector. Compared to PMTs, APDs has a significantly higher QE (from 55% to 90% at higher wavelengths). However, APDs have a relatively low timing resolution (∼ 5 ns), low gain (∼ 10^2 - 10^3) and require low-noise electronics for successful operation [26]. Philips Ingenuity TF PET/MR and GEs integrated Signa PET/MR are based on a silicon-PM detector technology.

SiPMs

A new generation of digital detectors based-on silicon photomultipliers (SiPM) has been replacing the analogue PMTs in recent years (see Figure 2.5). SiPMs are considered the semiconductor analogue of PMTs. A photon passing through the silicon layer may transfer its energy to a bound electron. This absorbed energy causes the electron to move from the valence band into the conduction band, creating an electron-hole pair. SiPMs are based on a densely packed array of ∼ 10^3 - 10^5 individual avalanche photodiodes of ∼20 μm - 100 μm operating in Geiger mode. Each detected photon generates a fast (time ∼ 1 ns), well-defined single-photoelectron pulse with a high gain (∼ 10^6). In other words, it operates in reverse bias to set up an electric field across the depletion region that will cause these charge carriers to be accelerated towards the anode (holes) and the cathode (electrons). All photodiodes are con-

nected through a polysilicon quenching resistor and are read in parallel. When a photon from the scintillator interacts with a photodiode, it causes a breakdown discharge that results in a pulse of high gain. Therefore the output of SiPM is the sum of all the pulses from every photodiode that detected a photon [23, 26, 27].

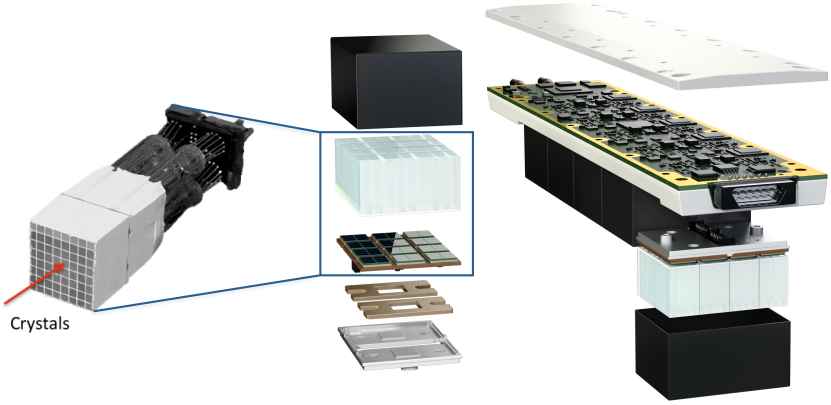

Fig. 2.5: *Right* GE signa integrated PET/MR detector with 25 mm deep crystal lutetium-based scintillator and 25 cm FOV. *Left* Not that the traditional photomultiplier tube is replaced by MR compatible SiPM. Image obtained and edited from [24, 28], under creative commons attribution unported license.

Compared to the analogue PMTs, SiMPs have comparable gain while operating in low voltages. Moreover, it combines the advantage of the compactness, the cost-effective semiconductor technology, the low power consumption, and the magnetic field insensibility of the APDs. The drawback is that SiPMs are more sensitive to temperature that PMTs [29, 30].

Monolithic scintillator detectors

In recent years monolithic scintillator detectors emerged as the next technology as a promising alternative to the state-of-the-art clinical PET detector blocks [31]. Detectors based on a monolithic scintillation crystal read out by pixelated photosensors are considered as alternatives to the clinical PET detectors used today (based on segmented crystals). The advantages are better spatial resolution with intrinsic depth-of-interaction (DOI) information (the light distribution changes if the

interaction takes place closer to the surface of the detector), improved light output and better timing properties [32]. This indicates that in principle a significantly better image resolution can be obtained (see Section 2.1.4).

However, in practice, eventual implementation of these monolithic scintillator detectors would require overcoming a number of technical challenges [31, 32]. While commercial preclinical systems already make use of monolithic, the research for clinically applicable monolithic PET detectors is ongoing [33, 34, 35, 36]. The biggest challenge and limitation is considered to be the lengthy calibration procedure that is necessary to obtain high-resolution detectors.

Time-of-flight information

Time-of-flight (TOF) information was early tested in different prototypes system during the 1980s. These PET systems used *Barium fluoride* (BaF2) or *cesium fluoride* (CsF) as a scintillator. However, because of the limited stopping power of the used scintillators, these systems had limited spatial resolution and sensitivity [37]. Over the last 10 years, TOF-PET/CT has vastly improved PET imaging quality and capabilities, with all commercial manufacturers offering a TOF-PET/CT scanner model (see Section 2.3). Current PET systems provide scintillators with a higher density (see Table 2.3), shorter decay time and modern electronics (see Figure 2.6).

Faster detectors may calculate the time interval (Δt) between the arrivals of the two annihilation photons and can more accurately estimate the origin of the annihilation process. The positioning accuracy Δx depends directly on the detector coincidence resolving time that is related via the relation: $\Delta x = (c\Delta t)/2$, where c is the speed of light in vacuum and (Δt) the timing accuracy. A new generation of TOF-PET scanners based-on SiPM detectors achieved a coincidence time resolution of fewer than 400 ps FWHM, making it capable of advanced TOF performance [23, 30]. Recently, a TOF resolution of 214 ps obtained with a SiPM-based detector with 3.2 mm LSO crystals was reported by Siemens Healthineers [38, 39].

As a result, TOF information leads to faster and more uniform con-

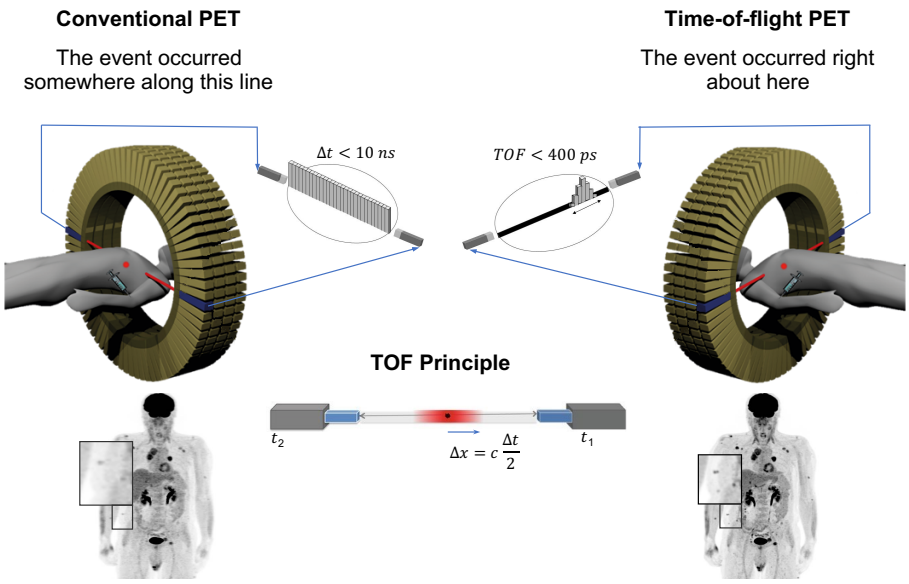

Fig. 2.6: Conventional PET vs TOF PET. The estimated time-of-flight difference (Δt) between the arrival times of photons on both detectors in TOF-PET allows localization (with a certain probability) of the point of annihilation on the line of response. In TOF-PET, the distance to the origin of scanner (Δx) is proportional to the TOF difference via the relation; Δt: $\Delta x = (c\Delta t)/2$, where c is the speed of light. t_1 is the arrival time on the first detector, and t_2 is the arrival time on the second detector. Image obtained and edited from [24, 37], under creative commons attribution unported license.

vergence of the reconstruction, improved lesion detectability, more homogeneous image quality, and more accurate quantification [40, 41, 42]. It has been shown in a number of studies that TOF leads to a significant improvement of the signal-to-noise ratio (SNR) and contrast recovery in both phantom, and as well as inpatient studies [21, 15, 43]. Furthermore, if a CT imaging data of the phantom/patient is available, TOF can be used to discard the possibility of events outside of the patient reducing the number of randoms [24, 4].

Coincidence Timing Resolution

Since a PET scanner relies on the coincidence detection of a pair of 511 keV photons, the PET system performance is highly influenced by the

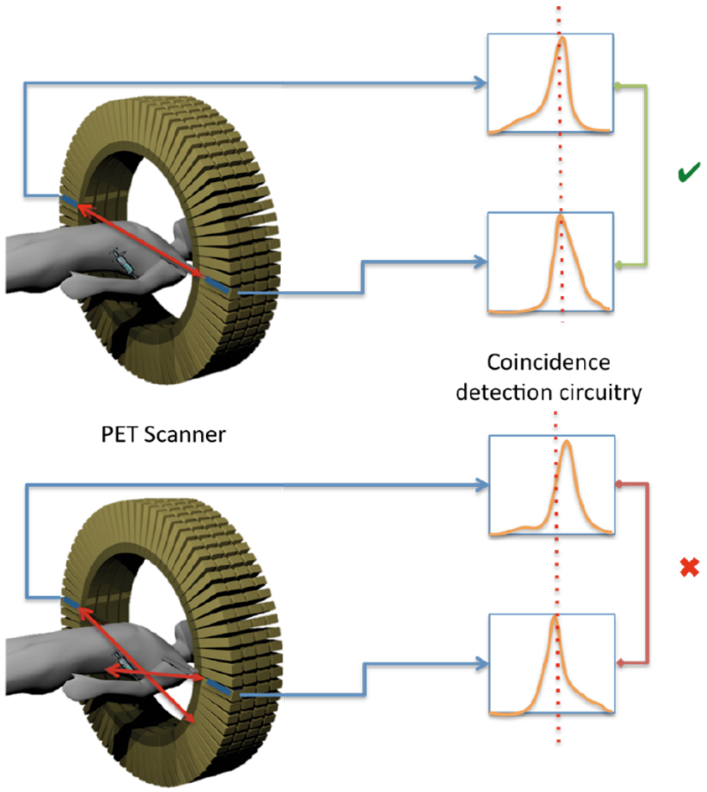

Fig. 2.7: Illustration of coincidence detection. For an annihilation event, the two annihilation photons are detected. A pulse is formed on each detector channel and only if two events t are detected within a few nanoseconds, these events are considered to have originated from the same annihilation event. Otherwise, both detections are discarded. Image obtained from [24].

scintillation and photodetector used. An important advantage of PET is the fact that due to the positron annihilation it expects to observe two photons at roughly the same time (in coincidence) in the detector ring are expected. In other words, the annihilation event will be located somewhere on the LOR connecting the interactions. By recording many LORs the activity distribution of the organ target can be reconstructed [4, 24]. Due to the fact that the detector cannot determine if the detected photons are from the same annihilation event, a short-acceptance timing window of typically a few nanoseconds (4.9 ns for a TOF-PET system) is predefined for the detection of both events (see Figure 2.7).

The concept of measuring 2 events from 1 annihilation with in the coincidence window is called coincidence detection, and a valid detection is called a coincidence. Fundamentally, three types of events can occur: true, scattered and randoms, as shown in Figure 2.10 (as will be discussed in the following sections). Since a PET scanner acquires different coincidence events that contribute to the image formation, there are also several degradation factors in the image quality correlated to these coincidences that need to be discussed.

2.1.4 System characteristics

Limitations of PET are due to various physical degradation factors, such as the positron range, non-collinearity of the annihilation photons, crystal penetration, inter-crystal scattering, photon attenuation, randoms and scatters [21, 44].

Spatial resolution

Spatial resolution is the ability of the PET scanner to accurately resolve spatially separated radioactive sources [45, 46]. In other words, it represents the minimum distance between two points such that they in principle can be resolved in a PET image as two separate spatial locations. It depends on a number of factors such as the physical processes of the positron decay and annihilation, the design of the scanner, the detector size and on the image reconstruction algorithms.

Detector spatial resolution: Crystal penetration and inter-crystal scattering

Currently, the largest degrading factor of the image spatial resolution in clinical PET systems is the limited accuracy by which the positions, where each of the annihilation photons interact with the detectors, can be determined. The positioning error increases for gamma photons that have a large angle of incidence on the detector and, thus may first penetrate one or more adjacent detector elements before being detected. The error caused by crystal penetration is also called the parallax error (see Figure 2.8).

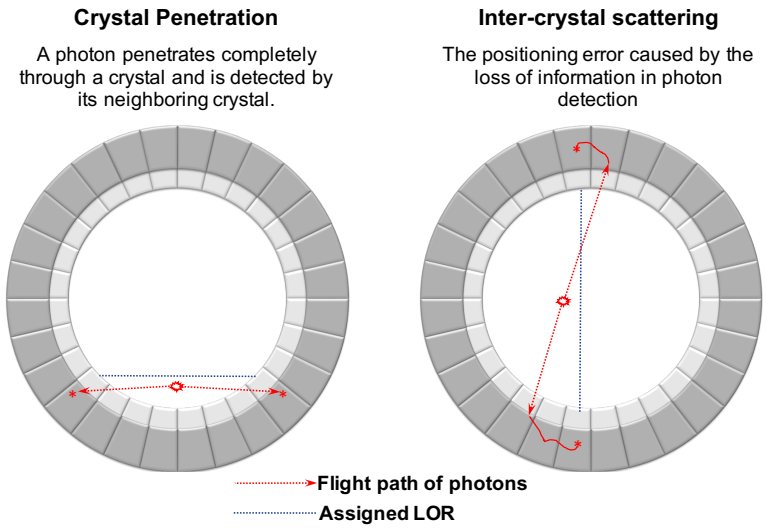

Fig. 2.8: *Left* Crystal penetration causes the parallax error. This effect can be found in a PET ring scanner of pixelated block detector and most notable for LORs at the edge of FOV. *Right* Illustration of the inter-crystal scattering.

In case an event would be assigned to the centre of the firing detector, the LOR may not pass through the annihilation point [47]. This effect is geometric and can be modelled analytically. By using depth-of-interaction (DOI) detector design the parallax error may be reduced.

Another factor that contributes to the image quality degradation is the inter crystal scattering (see Figure 2.8). The photon scatters in multiple crystals in a pixelized detector (small scintillation crystals) block. Thus the crystal that contains the first interaction site, may not be identified and processed by the system [48, 49].

For all PET detectors based on segmented crystals, the intrinsic resolution of the scintillation detector $R_{intrinsincR}$ is strongly related to the crystal size d. $R_{intrinsincR}$ is given by $(d/2)$ on the scanner axis at mid-position between the two detectors and by (d) at the face of either detectors. Thus, it is the best at the centre of the FOV and deteriorates at the edges of the FOV. It may contribute to the loss of spatial resolution due to the errors in the event localization caused by statistical fluctuation in the photodetector signals, scatter within the detector and imperfections in the block decoding scheme [50].

Positron range

A positron travels some distance through the surrounding tissue while losing kinetic energy. When it has lost sufficient energy, the positron captures an electron and subsequently decays into a pair of 511 keV annihilation photons (nearly in opposite directions), as is shown in Figure 2.9.

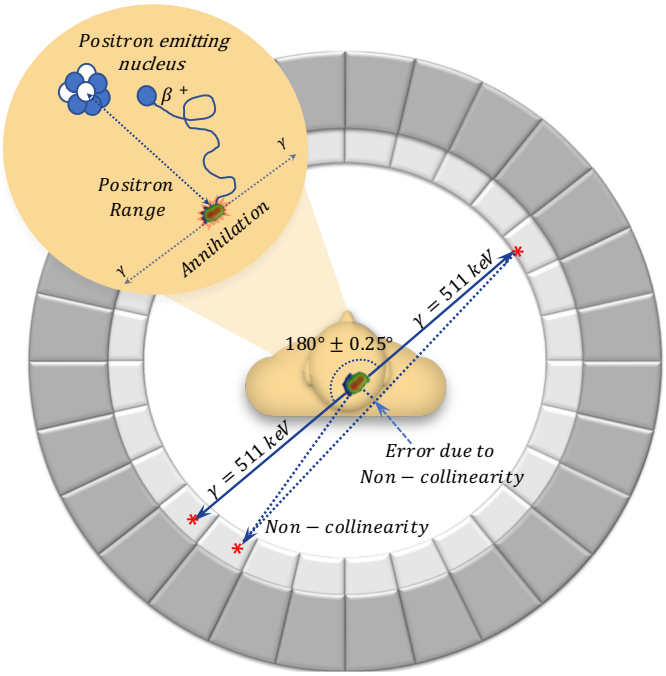

Fig. 2.9: After annihilation of a positron and an electron, two 511 keV photons are emitted in (almost) opposite directions. Non-collinearity leads to positioning errors. Note that the positron range is the distance between the positron emitting nucleus and the annihilation point event.

The maximum distance between the original emission point and the position of annihilation depends on the atomic number of the material and on the initial kinetic energy of the positrons, which in turn depends on the radioisotope used. Chapter 4 gives an overview of the positron ranges of different PET radioisotopes used in a clinical setting.

$R_{positron}$ is of minor concern for ^{18}F, ^{11}C, and ^{13}N imaging but it becomes a more prominent issue for high energy isotopes such as ^{15}O

^{68}Ga, and ^{82}Rb (see Chapter 4, Table 4.4). Since coincidence detection is related to the location of annihilation (not to the location of β^+ emission), an error occurs in the localization of true position of the positron emission thus resulting in the degradation of spatial resolution. The contribution of positron range ($R_{positron}$) on the image spatial resolution is expressed in terms of the full width at half maximum (FWHM).

In case of integrated PET and MRI systems, the presence of a strong magnetic field (3 Tesla for most of the clinical PET/MR systems) will cause the positron to travel in a helical path, therefore reducing the positron range in the plane transverse to the magnetic field but extending it in the direction along the main magnetic field. Several studies have already proven a reduced positron range due to the presence of a magnetic field [11, 51, 52]. This is discussed in more detail in Chapters 3 and 4, where a realistic GATE Monte Carlos model of the PET/MR is used to evaluate the effect of the MR field on positron range.

Non-collinearity

As the total momentum is preserved in the annihilation process, the 511 keV gamma photons may not be emitted in exactly opposite directions. The width of the angular distribution of this deviation, referred to as non-collinearity, is usually assumed to be in the order of $\pm$ 0.25° [53]. As a consequence, the detected LOR may not intersect the real annihilation point (see Figure 2.9). The effect of non-collinearity on the image resolution $R_{non-collinearity}$ is largest in the centre of the scanner, where its effect in terms of FWHM can be estimated as:

$$R_{non-collinearity} \approx \left(0.25 \times \frac{\pi}{180^\circ}\right) \frac{D_{scanner}}{2} \tag{2.5}$$

$$R_{non-collinearity} \approx 0.0022 \cdot D_{scanner} \tag{2.6}$$

where $D_{scanner}$ is the scanner diameter. The effect of $R_{non-collinearity}$ in the image resolution is directly proportional to the $\mathrm{D}_{scanner}$ [24, 53]. Therefore, the $R_{non-collinearity}$ worsens with large diameter. For a clinical scanner with a ring diameter of 70 cm and 90 cm, this effect is in the order of ∼1.5 mm to ∼2.0 mm, respectively.

Image spatial resolution

In most cases, multiple factors contribute to spatial resolution and image blurring. Combining the contributions mentioned, the image spatial resolution $R_{imageSR}$ of a PET image for events in the centre of the scanner can be estimated by using Eq 2.7:

$$R_{imageSR} \approx k_{recon} \cdot \sqrt{R^2_{intrinsincR} + R^2_{non-collinearity} + R^2_{positron}} \quad (2.7)$$

Where k_{recon} is an experimental factor that takes into account imperfections resulting from the reconstruction method (usually a factor of 1.2 to 1.5, depending on the reconstruction settings) [54, 53]. An overview of the performance characteristics of PET scanners available on the market is given in Table 2.4.

Sensitivity

PET scanner sensitivity is defined as the fraction of detected positron annihilation events relative to the activity present in a source (usually expressed in cps/MBq). To obtain a high scanner sensitivity, a high gamma photon efficiency of the detectors is essential. Since both annihilation photons have to be detected, the scanner sensitivity is correlated to the square of the detector's detection efficiency (i.e what fraction of the annihilation photons that pass through the detectors are actually absorbed, converted and detected). It is also important to mention that detector detection efficiency is highly dependent on the material and the thickness of the scintillation crystal [27] and the type of used radioisotope (see Chapter 3). Because the radiation is being emitted isotropically the solid angle coverage of the scanner is also a limiting factor (i.e. how much of the solid angle around the patient is being covered). The sensitivity of a point source at the centre of a single ring scanner can be expressed by:

$$S_{sensitivity} = \frac{A \cdot \varepsilon^2 \cdot \exp^{-\mu t}}{4\pi r^2} \quad (2.8)$$

where A is the detector area is seen by each point of the object to be imaged, ε is the detector efficiency, μ is the linear attenuation, t is the thickness of the detector and r is the radius of the detector ring [5].

The scanner sensitivity improves with increased geometry efficiency. This can be done by reducing the scanner diameter and/or by increasing its axial FOV [23, 30]. As a result, a high sensitivity scanner will reduce imaging time or permit imaging at lower activity concentration, thereby decreasing the injected activity. It will also permit dynamic scans with short-lived isotopes and repeated longitudinal studies without concerns over administered dose.

Noise sources: randoms, scattering, and photon attenuation

As discussed in 2.1.3, if both 511 keV photons originating from a single emitted positron are detected in two nearly opposite directions, this is referred to as a *true coincidence* (or simply a *true*) (see Figure 2.10). However, due to several effects, the determined LOR does not pass through the voxel in which the annihilation took place and in general corrections are required in the acquisition and reconstruction.

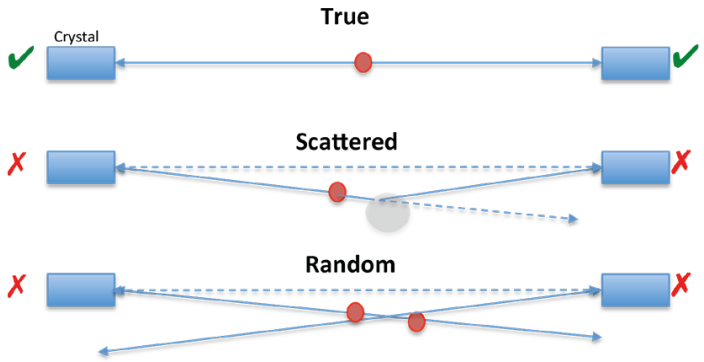

Fig. 2.10: Three possibilities exist for such a measurement: true, scattered and random coincidence. In the last two types, the annihilation event (marked with a red circle) does not lie on the apparent line of response between the two photon detections. Image obtained from [24].

The first noise source originates from *scattered coincidences*, when

one or both photons from a single positron decay undergo single or multiple Compton scattering in the patient's body. As a result, one (or both) annihilation photons might be deflected from their initial trajectory and will either not be detected or they will be detected by a different detector pair than expected. This wrong spatial association highly contributes to the deterioration of the image signal-to-noise (SNR) ratio [55]. Since the annihilation photons lose energy in a Compton event, scattered photons can be identified and rejected by applying an energy threshold, if the energy of a detected photon can be determined with a high enough accuracy [56].

A second type of image SNR deterioration originates from *random coincidences* (or simply *random*). They occur when two unrelated photon annihilation are registered on a detector pair within the set energy and timing window. The proportion of randoms increases with increasing energy window, coincidence timing window, and increasing activity injected (especially for non-pure radioisotopes, see section 2.1.2). These randoms directly affect image SNR. Random coincidence (R) can be measured by measuring the single count rate on each detector for a given time window and then corrections are made by subtracting it from the prompts between a detector pair [57]. This is given by the Eq 2.9:

$$R = 2\tau \cdot S_1 \cdot S_2 \tag{2.9}$$

where τ is the time width of the pulses in nanoseconds for the system and S_1 and S_2 are the single count rates in *counts/s* on each of the two detectors along the LOR [57]. Another method to measure the randoms is to employ two coincidence circuits, one with the standard time window and another with a delayed time window [58].

The third source of error is (somewhat related to the first one), the photoelectric absorption of one or both annihilation photons in the patient's body [59], known as attenuation. As a result, these photons (from annihilation deep inside the body) have a lower probability to reach the detector. Without corrections, it will result in a hampering quantification and a reduction of SNR in the reconstructed image.

One method to correct attenuation and scattering is to calculate patient-specific attenuation and scattering coefficient maps [59]. In prac-

tice, this is done by using the measured patient data from CT.

2.1.5 PET data acquisition

In PET data acquisition, the electrical pulse produced by the PET detector undergoes signal conditioning and processing before being handled by the data acquisition system. Thus, the PMT/SiPM outputs are routed to an amplifier and shaper first, before being digitized by an analogue to digital converter (ADC) [60]. The position, energy, and the TOF information (if it is the case) for all valid events will be stored by the data acquisition module to be used later for performing data corrections and reconstructions. The digital image is represented by a matrix of digital values that can be read by a computer and displayed or modified in order to emphasize the diagnostic information.

Frame vs list-mode

Data are acquired in either frame mode or list mode. In *frame-mode*, digitized signals are collected and stored in a matrix of given size and depth for a specified time or a total number of counts. In other words, one frame of data represents a set of sinograms during a given acquisition. In *list-mode*, digitized signals are coded with time marks as they are received in sequence and stored as individual events. After the acquisition is completed, data are manipulated to form images. This permits retrospective framing with frame duration chosen after the data are acquired. This allows more flexibility as additional information such as photon energy and timing can be included [61]. Furthermore, the list-mode acquisition provides fast acquisition speeds at the expense of data volume [62].

Sinograms

In the scanner, coincidence events are observed and identified along their LORs between pairs of detector elements (see Figure 2.1). To organize these raw data, the LORs are stored in such a way that all the LORs passing through a single point form a sinusoid curve in the raw data

histogram. Each point in image space will, therefore, result in a sinusoid on the sinogram containing the data for a single transaxial section through the patient [4].

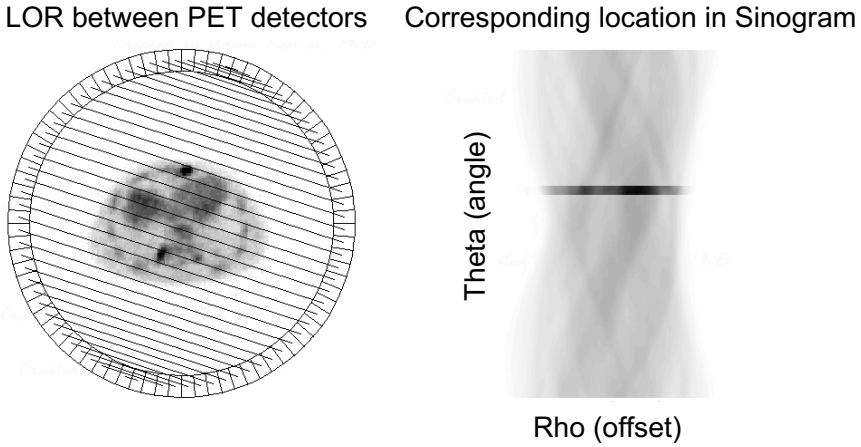

Fig. 2.11: The 2D (also can be acquired in 3D mode) image of the tracer distribution is collected by sorting each event into its appropriate location in sinogram space where each line of response has a corresponding angle and offset to indicate its location in the sinogram. Image obtained and edited from [63], under creative commons attribution unported license.

At this level (see Figure 2.11), the sinogram is normally corrected and reconstructed by using a reconstruction algorithm. Image reconstruction is in this sense aiming to resolve the inverse problem of the acquisition, in which the final product will be a three-dimensional representation of the tracer distribution, as it is in reality.

2.2 PET reconstruction

After the acquisition of PET data, the next stage in the PET processing chain is to reconstruct an estimate of the *in-vivo* tracer distribution. The image reconstruction process is the most mathematically complex step and is well described elsewhere. This section will point out the differences between the two (analytical and iterative) most common methods: *filtered-backprojection* (FBP), which is a well-established method,

ordered-subsets expectation maximization (OSEM), which is the widely used reconstruction algorithm in nuclear medicine and the more recent iterative approach the Bayesian penalized likelihood reconstruction algorithm, which uses a *block sequential regularized expectation maximization* (BSREM) as an optimizer. A full chapter will be dedicated to evaluating the impact on the image quality by using different reconstruction methods. (see Chapter 5).

2.2.1 FBP

Filtered-back projection is an analytical reconstruction method, which consists of back-projecting the raw data (rows and columns representing angular and radial samplings) across the imaging matrix. Once a sinogram is created, an image of the tracer distribution can be mathematically obtained as shown in Figure 2.12.

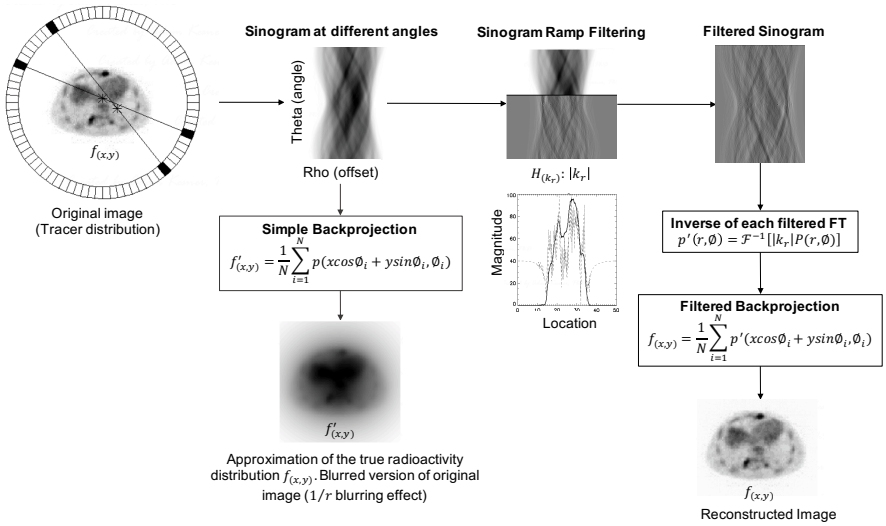

Fig. 2.12: Illustration of the difference between Simple Backprojection and Filtered Backprojection. Image obtained and edited from [63], under creative commons attribution unported license.

The simple back-projection has the problem of blurring effect ($\frac{1}{r}$) artefacts caused by "shining through" (as described by [4]) radiations from adjacent areas of increased radioactivity. It results in an approx-

imation of the original image (true activity distribution $f'_{(x,y)}$). This result in a blurred version of the original image $f_{(x,y)}$ (see Figure 2.12). The blurring effect is minimized by applying a ramp filter to the acquisition data, and filtered projection data are then Backprojected to produce an image that is more representative of the original image $f_{(x,y)}$. Applying the ramp filter H_{k_r} in Fourier space produces a modified Fourier transform for each projection, which is given by $P'(_{k_r,\phi)} = |k_r|P(_{k_r,\phi)}$. $P(_{k_r,\phi)}$ is the unfiltered Fourier transform. Finally, the inverse Fourier transform is performed to obtain filtered projection data in the spatial domain, which are then back-projected in the same way as in the Simple Backprojection $f_{(x,y)}$.

This reconstruction method requires continuous sampling of the projection data (both linear and angular projections related to r and ϕ of the sinogram) for an accurate back-projection. Additionally, data noise, positron range, non-collinearity, scattering, and random events are not taken into consideration in the method [64]. These reasons combined with the advance of computer processing, make the iterative methods (see next section) a more attractive reconstruction method. (Note that FBP still widely used as the optimal reconstruction method for NEMA spatial resolution test, see Section 2.4).

2.2.2 OSEM

The most common and widely used iterative reconstruction algorithm in PET clinical imaging is OSEM, an accelerated variant of the maximum likelihood expectation maximization (MLEM) algorithm. In MLEM, the maximum likelihood (ML) formulation gives an indication of which solution $\hat{\mathsf{f}}$ has greatest statistical consistency with the observed data by maximizing the likelihood $\hat{\mathsf{f}} = \arg\max_{\mathsf{f}} \mathcal{P}\{\mathsf{p};\mathsf{f}\}$. $\mathcal{P}\{\mathsf{p};\mathsf{f}\}$ is the probability of detecting pi counts on LOR i, given the tracer distribution f.

OSEM accelerates the convergence of ML by performing updates based only on a portion of the data, which approximates the MLEM solution in much less reconstruction time. This technique divides the data into several subsets following a certain order. Equation 2.10 is applied to each subset

$$\hat{f}_j^{(k+1)} = \frac{\hat{f}_j^{(k)}}{\sum\limits_{m \in S_\circ} h_{mj}} \sum_{i \in S_\circ} h_{ij} \frac{p_i}{\sum\limits_n h_{in} \hat{f}_n^{(k)}}, \tag{2.10}$$

where k is the iteration number, i the LOR index and j, m, n the voxel indices (Figure 2.13 shows a schematic illustration of how iterative reconstructions estimate the radiopharmaceutical distribution in the patient's body).

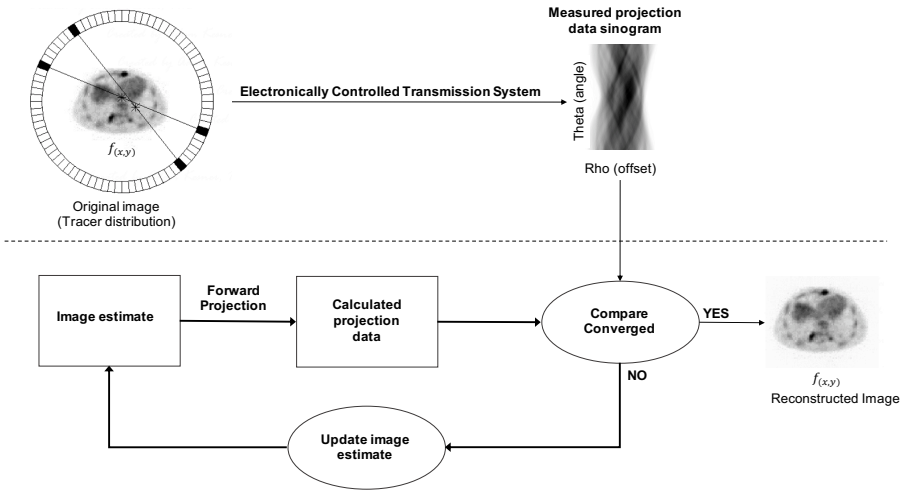

Fig. 2.13: Schematic illustration of the steps in iterative reconstruction. An initial image estimate is made and projections are calculated by forwarding projection. The calculated forward projection profiles for the estimated image are compared to the profiles actually recorded from the object and the difference is used to modify the estimated image to provide a closer match. Image obtained and edited from [63], under creative commons attribution unported license.

The term $\sum\limits_n h_{in} \hat{f}_n^{(k)}$ is the forward projection that gives an estimate of the measured data p_i. The estimated projections and measured data are compared by calculating the ratio:

$$\frac{p_i}{\sum\limits_n h_{in} \hat{f}_n^{(k)}} \tag{2.11}$$

The error is backprojected into the image space by Equation 2.12 and then the backprojected data is normalized, as it is given by Equation

2.13.

$$\sum_{i \in S_\circ} h_{ij} \frac{p_i}{\sum\limits_n h_{in} \hat{f}_n^{(k)}} \tag{2.12}$$

$$\frac{1}{\sum\limits_{m \in S_\circ} h_{mj}} \sum_{i \in S_\circ} h_{ij} \frac{p_i}{\sum\limits_n h_{in} \hat{f}_n^{(k)}} \tag{2.13}$$

The back-projection is only performed for the projection data belonging to a subset $S_\circ$. At each update, a different subset is selected. This accelerated convergence through the use of subsets, allows the OSEM algorithm to generate PET images in clinically feasible times [65]. However, one drawback to MLEM and OSEM is that it generally cannot be run to full convergence because the noise in the image grows with each iteration (see Figure 3.6 in Chapter 3). In order to reduce image noise, the OSEM algorithm is usually stopped before the convergence occurs, in order to prevent excessive image noise amplification. In clinical practice, the algorithm is stopped after 2-4 iterations and 20-30 subsets to make sure the full image is close to convergence and all high-frequency components are reconstructed. Additionally, these images are typically post-smoothed after reconstruction using a low-pass filter to reduce noise levels [66].

2.2.3 BSREM

As discussed above, one drawback of the maximum likelihood reconstruction in emission tomography is the excessive noise propagation. An effective way to suppress this noise propagation is to use the maximum a posteriori approach [67]. The prior most often used is a Gibbs distribution which penalizes absolute differences between neighbouring pixels. The Bayesian Penalized Likelihood (BPL) reconstruction algorithm uses a Sequential Regularized Expectation-Maximization (BSREM) to improve the image quality by controlling noise amplification during image reconstruction. It makes use of the Relative Difference Penalty (RDP), which has the advantage of providing activity-dependent noise control [2, 68]. BSREM formulation uses the Maximum a Posteriori (MAP) criterion that can be expressed as:

$$\hat{\mathsf{f}} = \underset{\mathsf{f}}{\mathsf{argmax}} \mathcal{P}\{\mathsf{p};\mathsf{f}\} = \underset{\mathsf{f}}{\mathsf{argmax}} \frac{\mathcal{P}\{\mathsf{p};\mathsf{f}\} \cdot \mathcal{P}\{\mathsf{f}\}}{\mathcal{P}\{\mathsf{p}\}} \tag{2.14}$$

By taking the logarithm and ignoring $\mathcal{P}\{\mathsf{p}\}$ (not a function of f) the MAP criterion is modified:

$$\hat{\mathsf{f}} = \underset{\mathsf{f}}{\mathsf{argmax}} [\log \mathcal{P}\{\mathsf{p};\mathsf{f}\} + \log \mathcal{P}\{\mathsf{f}\} \tag{2.15}$$

An energy function $U(\mathsf{f}) = \log \mathcal{P}\{\mathsf{f}\}$ can now be utilized to penalize image solutions that do not possess expected properties (the energy function $U(\mathsf{f})$ is designed, so that the expected image configurations are those for which neighbouring pixels have similar intensities). The solution can be found using the following MAP algorithm:

$$\hat{f}_j^{(k+1)} = \frac{\hat{f}_j^{(k)}}{\sum\limits_m h_{mj} + \beta \frac{\partial U(\mathsf{f})}{\partial f_j}|_{f_j=\hat{f}_j^{(k)}}} \sum_i h_{ij} \frac{p_i}{\sum\limits_n h_{in} \hat{f}_n^{(k)}}, \tag{2.16}$$

with β with a positive weighting parameter which controls the influence of the penalty. As a result, the BSREM only needs to set a penalty strength instead of the iterations and subsets in conventional OSEM reconstruction. This allows the algorithm to reach full convergence without increasing noise while preserving edges [69]. Therefore, filters for post-smoothing are not necessary. However, there is a minor risk of using BSREM when the primary requirement is to detect small lesions. This will be discussed in Chapter 5.

2.3 Hybrid systems

Hybrid systems have recently become commercially available with the potential to change medical imaging by providing combined anatomical-metabolic image information. In this section, I will describe some commercial state-of-art PET/CT and PET/MR hybrid imaging systems.

Tab. 2.4: NEMA data on PET/CT scanners based-on SiPM detectors available on the market.

Parameters	GE			Siemens	Philips
	DMI 3 Rings	DMI 4 Rings	DMI 5 Rings	Biograph Vision	Vereos Digital
Axial FOV (cm)	15	20	25	26.1	16.4
Transverse FOV (cm)	70	70	70	78	67.6
Crystal T. (mm)	25	25	25	20	19
Spatial R. (FWHM)					
Rad, 1 cm	4.69	4.1	3.68	3.7	4.11
Tang, 1 cm	4.08	4.19	4.01	3.7	4.11
Axial, 1 cm	4.68	4.48	4.28	3.8	3.96
Rad, 10 cm	5.58	5.47	4.79	4.6	NA
Tang, 10 cm	4.64	4.49	3.83	3.9	NA
Axial, 10 cm	5.08	6.01	4.9	4.3	NA
Rad, 20 cm	7.53	7.53	NA	6.0	5.79
Tang, 20 cm	5.08	4.9	NA	3.6	5.79
Axial, 20 cm	5.47	6.1	NA	4.6	6.2
Sensitivity (cps/kBq)	7.3	13.7	20.28	16.4	5.7
Counting rate statistics					
Peak NECR (kcps)	102.3	193.4	268.9	306	171
Peak NEC Activity (kBq/ml)	23	21.9	21	32.6	50
Peak NEC SF (%)	41.2	40.6	41.5	38.7	30
Maximum Error (%)	3.88	3.14	3.2	1.25	NA
Timing R. (ps)	375.6	375.4	376	NA	316
Energy R. (%)	9.3	9.4	9.6	NA	11.1

2.3.1 PET and CT

As explained in Section 1.1, the PET modality as a diagnostic tool is limited by its spatial resolution and the absence of clear anatomical landmarks. However, integrating PET images with anatomical information provided from CT can improve diagnostic accuracy. Several studies have shown the benefit of PET/CT hybrid imaging. Bar-Sholam et al. assessed the additional value of hybrid PET/CT over stand-alone PET and stand-alone CT with a study of 204 cancer patients with 586 sites suspicious of disease [70]. An improved diagnostic interpretation of 49% of cancer patients and 30% of sites were reported. The additional value includes precise lesion characterization, lesion localization and lesion detection. In 14% of cancer patients, combined PET/CT had an impact on the patient management which included referral and planning of surgery, chemotherapy, radiotherapy, exclusion of cancer and guidance in invasive diagnostic procedures. Another study with 2847 prostate cancer patients using ^{11}[C]choline PET/CT has reported a significantly increased accuracy of prediction of prostate cancer [71].

The ability of hybrid PET/CT systems to accurately identify the anatomic location of focal lesions and to provide attenuation-corrected images led to the rapid introduction of commercial systems by the major medical imaging companies (all systems nowadays are combined PET/CT systems). Table 2.4 shows the PET performance and specification of the last generation of PET/CT scanners based-on high-resolution SiPM detectors currently available on the market.

2.3.2 PET and MRI

There are many clinical situations in which MR imaging, rather than CT, is the anatomic imaging technique of choice (such as the paranasal sinuses, salivary glands, oral cavity, and brain). Furthermore, the high resolution as well as high contrast, allows to distinguish different soft tissues much better than any other modality without exposing the patient to ionizing radiation. As shown in Figure 2.14, over the last decade, the combination of PET and MRI in one system has proven to be highly successful in basic preclinical research, as well as in clinical research.

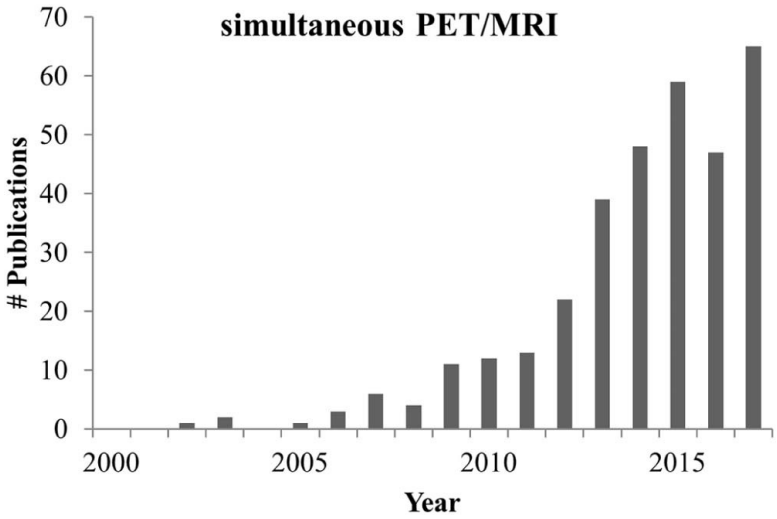

Fig. 2.14: Number of publications regarding simultaneous PET/MR imaging starting in the year 2000. Image obtained from [72]

Despite the great potential of the fully integrated PET/MR systems, there were major issues that had to be solved before being used into clinical practice. The first was to make the PET detector MR-compatible. Secondly, a proper design for the integration of the PET and the MRI scanner, and finally, the development of MR based attenuation maps for accurate PET imaging.

MR-compatible PET detector design

Traditional PET detectors are usually made of inorganic scintillation crystals, lutetium oxyorthosilicate (LSO) or LYSO being the most used, coupled to PMTs. However, these detectors are sensitive to magnetic fields. The magnetic field causes the electrons to deviate from their original path, causing a tremendous loss in gain and rendering PMTs essentially useless in the magnetic field of several mT [72]. In the early stages, the focus was mainly on separating the detector crystals from the PMTs and coupling them via fibre optics, placing all the PMTs in a magnetic field-free environment. This solution was very impractical and raised many problems, such as the handling of such a large quantity of fibre optics, and poor energy and timing resolutions due to light loss [73].

Tab. 2.5: Comparison of different types of photodetectors used in PET/MR systems [4].

	Gain	Bias Voltage	Size	Efficiency	Temporal Resolution	Cost
PMT	10^6	800V-1kV	Larger	∼30%	<600 ps	High
APD	10^2	10V-1kV	Small	∼80 %	∼1 ns	Medium
SiPM	10^6	30V	Small	<40%	∼100 ps	Low

Avalanche photodiodes (APDs) have been proposed as an alternative to the standard PMT because these devices are compact and rugged as well as insensitive to the magnetic field [44]. However, they have a small gain, large excess noise, and large performance fluctuation according to bias voltage and temperature (see Table 2.5). The focus shifted to the development of a new generation of detectors that could replace PMTs and perform well under magnetic fields. SiPM have been proposed. It allows the integration of fast PET detectors in an MR environment and enables TOF information timing resolution (below 400 ps) [74]. Compared to APDs, SiPMs have a much higher gain at much lower voltages, providing a high SNR [75]. More technical detail on both types of photodetectors is shown in Table 2.5.

Fully integrated system design

A fully integrated PET/MR system integrates the PET and MRI scanners in a single gantry. The smaller detector bore and long axial extent (25 cm) of the PET ring (in comparison to state-of-the-art PET/CT) results in a superior sensitivity of 21 cps/kBq (See Table 2.4), thus allowing a lower PET tracer dosing besides the evident dose reduction from omitting the CT. However, this configuration has some technical challenges associated with the mutual interference between the two imaging modalities including a major redesign of MRI. Most issues with this design option are related to the limited space available leading to significant constraints on the PET system. On the other hand, this system design allows for shorter acquisition time and precise temporal and spatial registrations, resulting in simultaneous PET and MR image

acquisition. The reader is referred to Chapter 3 for more details.

Attenuation correction

For quantitative PET imaging, the reconstructed data need to be corrected for attenuation. Contrary to PET/CT, the attenuation map can not directly be derived from the MRI data acquired by the integrated PET/MRI. This is due to the fact that MR signals correlate with proton densities and relaxation properties of tissues. The available methods for MR-based attenuation correction can be grouped into three categories including segmentation-based methods, template or atlas registration-based methods, and joint estimation-based methods [76, 77]. As explained at the beginning of this chapter, a full description of this topic is out of the scope of this book.

At this stage, the reader might wonder about the details of the attenuation correction methodology used for phantom studies performed in this work. NEMA Image Quality measurement (See section 2.4) uses attenuation correction. The GE PET/MR uses a CT-based template attenuation correction for the NEMA IQ phantom. Attenuation coefficients for the phantom housing and its fluid fillings are derived from a predefined μ-map based on CT data. The μ-map is registered to the non-attenuation corrected reconstructed time-of-flight (TOF)-PET image and subsequently used during PET reconstruction with attenuation correction [78].

2.4 Acceptance tests for PET systems

In this section, the National Electrical Manufacturers Association (NEMA) performance measurement tests for PET scanners are described. It covers the different tests performed in this dissertation, as well as additional ones commonly performed. See Chapter 3 for more details.

2.4.1 NEMA Performance measurements

In order to reliably compare PET and PET/MR scanner's performances amongst different models, it is necessary (or at least recommendable)

that all manufacturers follow the same set of guidelines for testing of their scanners. The latest NEMA Standards Publication is NU 2-2018 [46] and provides the procedures to perform the necessary measures to characterize and classify PET scanners. The publication includes many different tests, such as spatial resolution, sensitivity, scatter fraction, count losses, random measurement and image quality, which will be described below.

2.4.2 Spatial Resolution

Spatial resolution (SR) is defined as the ability to distinguish between two points in the final, reconstructed image. FBP reconstruction is commonly used for this test without any post-processing. Resolution can mean both Full-Width Half Maximum (FWHM) and Full Width Tenth Maximum (FWTM), so it is important to clarify which one is being referred to. In both cases, the values are obtained through linear interpolation of the values of adjacent pixels corresponding to half or a tenth of the maximum value of the image's point spread functions. SR is determined in all directions, through radial, tangential and axial slices. For this test, glass capillary tubes are used, with sub-millimetric internal radius and length such that the activity is not spread out for more than 1 mm.

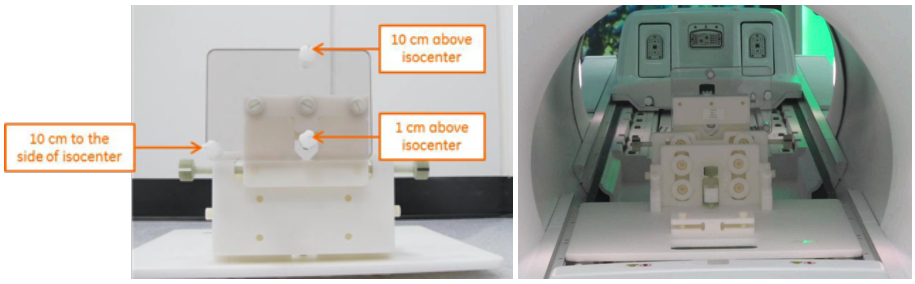

Fig. 2.15: *Left* Spatial Resolution phantom with 3 point source locations. *Right* Fixture positioning for spatial resolution scan.

A dedicated phantom that holds the capillaries in precise coordinates is shown in Figure 2.15. The test is performed at the center of the FOV and repeated at ¼ of the FOV of that distance. Deferentially of the NEMA NU-2-2007 where the SR measurement is reported at 1 and 10

cm above the isocenter (See Figure 2.15, left) NEMA NU-2-2012 requires 1, 10 and 20 cm above the isocenter SR measurement.

2.4.3 Sensitivity

Sensitivity is the efficiency of a scanner in obtaining coincidence data and is usually measured in counts per seconds per kilo becquerel (cps/kBq). It depends greatly on the geometry of the scanner (geometric efficiency) and also on the detection efficiency intrinsic to the detectors (intrinsic efficiency). The geometric efficiency is dependent on the width and length of the scanner, more specifically on the detectable solid angle, inside which coincidences can be detected. The sensitivity test for PET scanners is performed with very low levels of activity spread out throughout a 70 cm plastic tube, to minimise the effect of dead time. This low injected activity, allows the count losses and random events rate to be at less than 1% and 5%, respectively. For ^{18}F, NEMA recommends an activity between 5 to 10 MBq at scan start time.

Successive measurements are taken, adding a layer of attenuating material (aluminum) between each scan (Figure 2.16, *A*). The tubes are positioned parallel to the axial direction and are held in place by a phantom holder (Figure 2.16, *B*), to minimize movement of the source between each scan. The procedure is repeated two times, at different radial positions: at the centre of the FOV and with a 10 cm offset from the centre. The attenuation-free sensitivity is obtained by extrapolating the value from the multiple attenuated measurements. The NEMA sensitivity data are then collected for a period of time to ensure that at least 10.000 trues per slice are collected. To obtain the system sensitivity, the data for each of the 5 layers should be made to fit the following equation 2.17:

$$S_i = S_0 \times \exp^{-2\mu_{Al}X_i} \tag{2.17}$$

where μ_{Al} is the attenuation coefficient of the material, X_i is the accumulated layer thickness and S_0 is the attenuation-free sensitivity. This procedure is done for measurements at the centre of the FOV and with a 10 cm radial offset from the centre. The final reported sensitivity value is the average of both values.

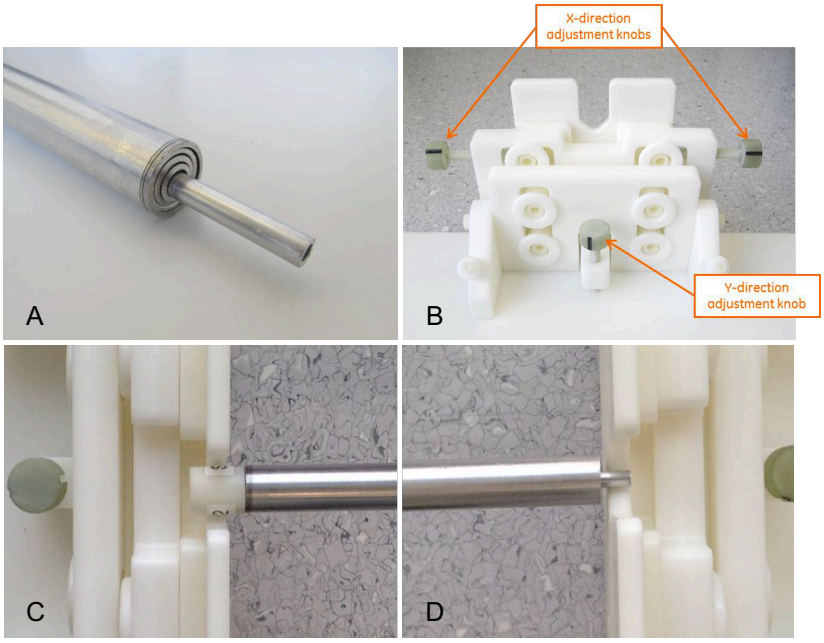

Fig. 2.16: *(A)* Five layers of attenuating material (aluminium) of 2.5 mm thickness each,*(B)* shows X and Y adjustment knobs (one full turn approximately 1 mm of adjustment),*(C)* Support one side with White knob and in *(D)* Support other side with the smallest tube.

2.4.4 Scatter fraction, Count losses and Random

The scatter fraction, count losses and random measurements also referred to as count rate statistics test, are obtained from a single test that aims to calculate a system's ability to measure high activity sources and to recognize scattered radiation, as opposed to radiation coming directly from the positron annihilations. Peak NECR and the activity at which it occurs is the output of this test.

This test is performed overnight with a scatter phantom, a long, 70 cm polyethylene cylinder through which a 70 cm line source runs all through its height, 4 cm below the center (Figure 2.17). The scatter phantom is positioned parallel to the axial direction of the scanner and the line source is filled with very high levels of activity (between 850 - 900 MBq). Successive measurements are obtained to measure each rate (total prompts and true, random and scattered coincidence rates)

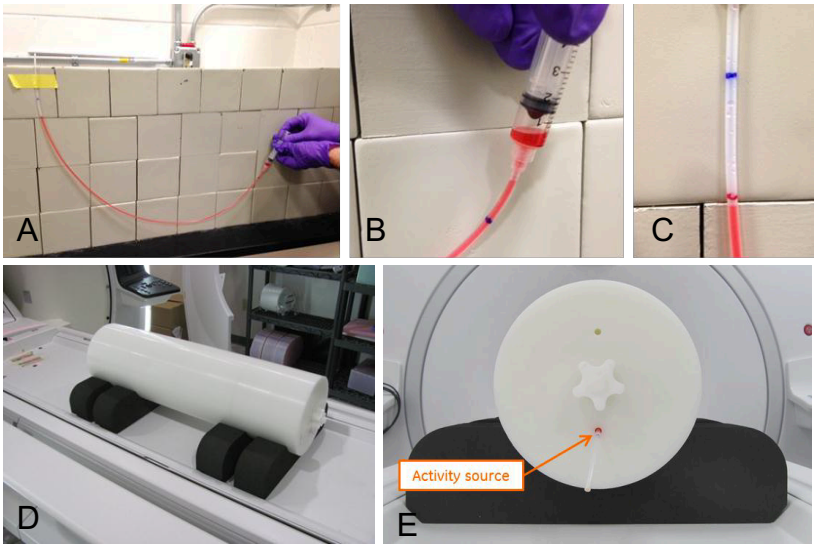

Fig. 2.17: In *(A, B, and C)* shows the steps on how to add activity to the red mark in the line source. *(D)* shows the PET scatter phantom positioned on the cradle, and in *(E)* shows the rotated scatter phantom (drilled hole for line source directly below central axis of cylinder).

for multiple levels of activity. The rates are plotted against the activity concentration. For each activity concentration A, the *total*, $R_{Total,A}$ *true* $R_{True,A}$, *random* $R_{Random,A}$, and *scattered* $R_{Scatter,A}$ events count rates are calculated, respectively by:

$$R_{Total,A} = \frac{C_{Total,A}}{Total_{acquisition,A}} \tag{2.18}$$

$$R_{True,A} = \frac{C_{Total,A} - C_{r+s,A}}{Total_{acquisition,A}} \tag{2.19}$$

where $C_{r+s,A}$ is the number of random plus scatter counts.

$$R_{Random,A} = R_{Total,A} - \frac{T_{True,A}}{(1 - ScatterFraction)} \tag{2.20}$$

$$R_{Scatter,A} = \frac{T_{True,A}}{(1 - ScatterFraction)} \times R_{True,A} \tag{2.21}$$

The scatter fraction (SF) is obtained only for the lowest activity acqui-

sitions, where the count losses and randoms rate are expected to be less than 1% of the trues rate.

$$SF = \sum_{A} \frac{C_{r+s,A}}{C_{Total,A}} \tag{2.22}$$

2.4.5 Image Quality

Image quality is determined from a test that aims to simulate the whole body. It used two phantoms: a body phantom that simulated soft tissue, hot and cold lesions and lung tissue and the scatter phantom used previously (Figure 2.17). The background volume of the phantom is usually filled with an activity concentration of 5.3 kBq/ml (52 MBq of ^{18}F for 9800 ml as the NEMA recommendations). For the six spheres (10 mm, 13 mm, 17 mm, 22 mm, 28 mm, and 37 mm) in diameter the sphere to background ratio is recommended to be 4:1 or 8:1 (depending on the context of the measurement). A central cylinder is filled with foam beads to simulate lung tissue (Figure 2.18, *A*). A dedicated image quality study using four different contrast ratios (8:1, 6:1, 4:1, and 2:1) is reported in Chapter 5. By coupling the scatter phantom to the body phantom the test becomes more realistic, as the scatter phantom simulates the scattered radiation that comes from body parts that stay out of the scanner. The phantom data experiments are obtained during a single bed position scan (usually 5.0 to 10 min) in the full FOV of the TOF PET/CT. The central slice contained the six spheres and the adjacent slices are also used for the background ROIs. 60 background ROIs of each slice of the reconstructed image (12 ROIs on each of five slices) are drawn on the slices as close as possible to ± 1 cm and ± 2 cm on either side of the central slice. The contrast recovery (CR) is determined for each hot sphere j by:

$$CR_{H,j} = 100 \times \frac{\left(\frac{C_{H,j}}{C_{B,j}} - 1\right)}{\left(\frac{a_H}{a_B} - 1\right)} \tag{2.23}$$

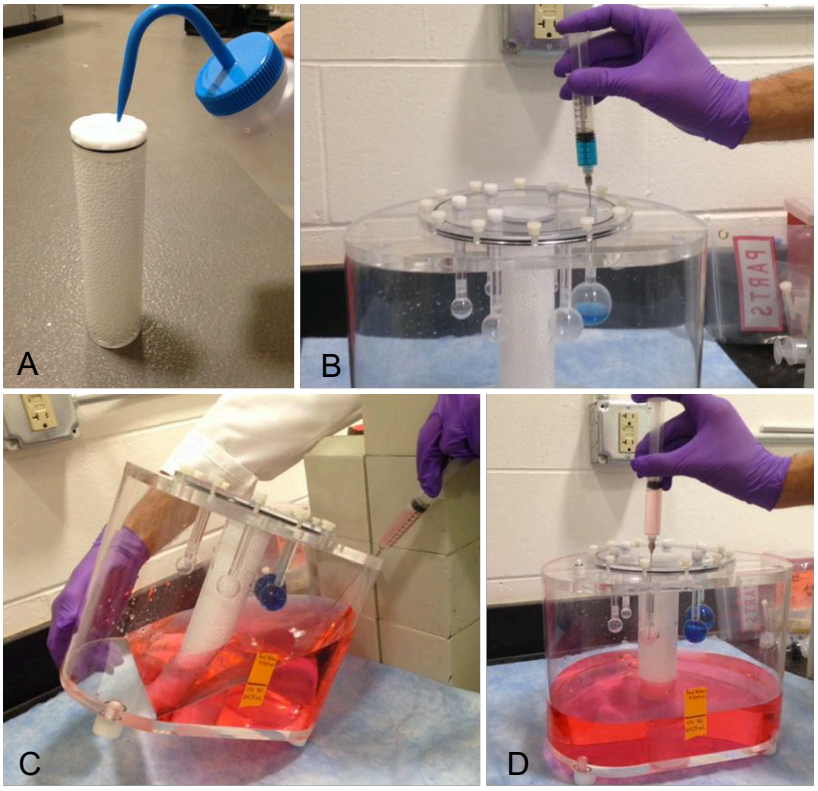

Fig. 2.18: Preparing NEMA IQ Phantom. After filling lung region with foam beads *(A)*, the remaining spaces are filled with water to simulate lung attenuation.*(B)* the "cold" (non-radioactive) spheres (28 and 37 mm) are filled with water and blue food coloring. In *(C)* after stirring well the activity injected in the background (according to respective contrast ratio), part of the activity is removed and *(D)* then inserted into four hot spheres (usually 10 mm, 13 mm, 17 mm, and 22 mm).

where $C_{H,j}$ is the average number of counts in the ROI in the transverse image slice that contains the centre of the sphere j. $C_{B,j}$ represents the average number of counts in the background ROI for sphere j. The terms a_H and a_B are the actual activity concentrations in the hot spheres and background respectively. The phantom has also 2 large spheres which are not usually filled with isotope. For each non-radioactive sphere j the

percentage contrast recovery $CR_{C,j}$ was calculated by:

$$CR_{C,j} = 100 \times \left(1 - \frac{C_{C,j}}{C_{B,j}}\right), \tag{2.24}$$

where $C_{C,j}$ and $C_{B,j}$ are average counts in the ROI for sphere j and average of all background ROI counts for sphere j. The background coefficient of variance (COV) is calculated as:

$$Background_{COV,j} = \frac{SD_j}{C_{B,j}} \tag{2.25}$$

where SD_j is the standard deviation and $C_{B,j}$ is the average of all counts for of the 60 background ROI counts for sphere j. The residual lung error (LE) calculation is defined by NEMA as:

$$L_{E,j} = \frac{C_{lung,i}}{C_{B,i}} \times 100\% \tag{2.26}$$

where $C_{lung,i}$ is the average counts for an ROI drawn in the lung insert on slice i, and $C_{B,i}$ the average background counts for slice i.

2.5 Monte Carlo methods

A Monte Carlo (MC) method can be described as a statistical method that uses random numbers as a base to perform a simulation of a specified situation. They are usually applied to simulate complex, nondeterministic processes which are difficult or impractical to reproduce with real experiments. The applications of the Monte Carlo method in medical physics cover almost all topics, including radiation protection, diagnostic radiology, radiotherapy and nuclear medicine [79, 80].

2.5.1 Relevance of MC to nuclear medicine

In nuclear medicine [80], The Monte Carlo method is a widely used research tool for different areas of diagnostic nuclear imaging, such as detector modelling and systems design, image correction and recon-

struction techniques, internal dosimetry and pharmacokinetic modelling. With the advent of high-speed supercomputers, the Monte Carlo method has received considerable attention, particularly in nuclear medicine, and a large number of applications were the result of such investigations [81, 82, 83]. Several researchers have also used Monte Carlo simulation methods to study potential designs of dedicated small animal positron tomographs [84, 85, 86]. Another promising application is the development and evaluation of image reconstruction algorithms and correction methods for photon attenuation and scattering in nuclear medicine imaging [87]. It allows a detailed investigation of the spatial and energy distribution of Compton scatter, which would be difficult to perform using present experimental techniques.

2.5.2 GATE Monte Carlo simulations

In this dissertation and a large portion of the current literature on PET, Monte Carlo simulations of the imaging process are performed using the simulation software GATE, the Geant4 Application for Tomographic Emission [83]. Figures 2.19 and 2.20 show an example of a PET/MR system configuration and NEMA IQ phantom obtained using GATE.

This is open-source software and continues to be developed by multiple internationally recognized research groups, together forming the *OpenGATE collaboration*. It builds upon Geant4 [88], a simulation toolkit collaboratively developed in C++ for comprehensive modelling of the physics of particle interactions. It is specifically developed to facilitate the use of certain Geant4 libraries for nuclear medicine applications, and it allows the design of standard geometries but also a significant amount of freedom in the system design. It also allows for the source and scanner components to move, and models the source decay evolution in time. It tracks the trajectory of the photons and simulates effects that occur as it goes through the phantom and detector materials, such as photoabsorption, *Compton scatter* and *Rayleigh scattering*. From running a program in GATE, the time and position of all photon detections are recorded, and with this information, we can produce the system performance that a real scanner would obtain. GATE simulation also gives more information about the processes occurring than a real

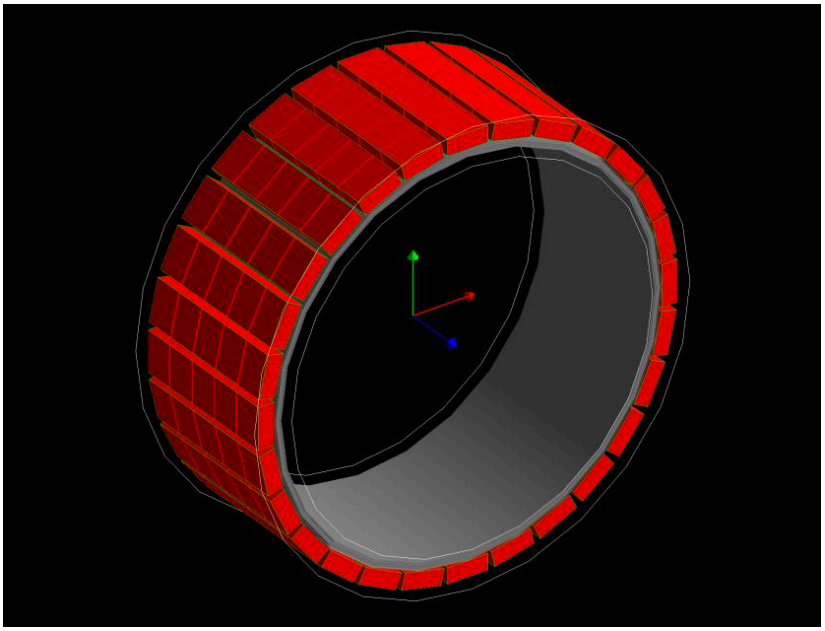

Fig. 2.19: Modelled GE Signa PET/MR geometry. CylindricalPET outline in white; rsector outlined in green; detector block and crystal represented in red; 12 attenuation layers represented in gray. For scale, the axis length is 10 cm is all directions.

experiment.

In this dissertation, GATE is used in Chapter 4 to predict the GE Signa PET/MR NEMA performance for different radioisotopes and to evaluate the effect of the MR field on positron range. The simulated data is validated using the measured data obtained in Chapter 3.

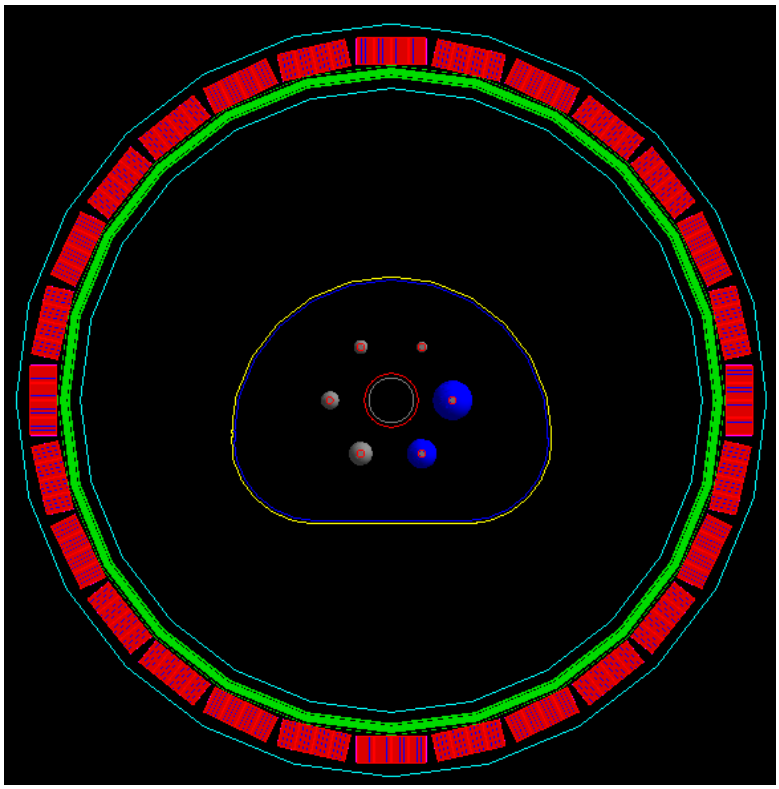

Fig. 2.20: Modelling of the GE Signa PET/MR system and NEMA IQ Phantom in GATE (axial slice at the center of the spheres). The detector material is shown in red, the attenuation media between scanner bore and crystal front face in green, and the NEMA IQ phantom placed in the center of the scanner.

3

Performance characteristics of PET/MR for different radioisotopes

In this chapter, we will discuss the important aspects of the fully integrated PET/MR system performance and the impact of using different radioisotopes.

3.1 Introduction

The Signa PET/MR has MR-compatible silicon photomultiplier (SiPMs) detector technology characterized by a superior light detection as compared to conventional PET technology [23, 28, 89]. The advantage of SiPMs versus avalanche photodiodes (APDs) is a faster response, enabling the combination of excellent Time-of-Flight (TOF) PET (close to 400 ps) imaging with MR scanning. The smaller detector bore and long axial extent (25 cm) of the PET ring (in comparison to state-of-the-art PET/CT) results in a superior sensitivity of 21 cps/kBq, thus allowing a lower PET tracer dosing besides the evident dose reduction by omitting the CT [90]. Hybrid PET/MR is a relatively new multimodality imaging technique, and offers the potential for combined structural, functional, and molecular imaging assessment of a wide variety of oncologic, neurologic, cardiovascular, and musculoskeletal conditions [50, 91]. However, the challenges beyond those of a technical nature remain for PET/MR imaging, including the standardization of appropriateness criteria, image acquisition parameters and clinically relevant and commercially available isotopes.

With PET becoming more widely used, the transport logistics have allowed faster shipments of radioisotopes to smalls imaging centers. The majority of PET studies in clinical routine are still being performed with ^{18}F, because of its physical properties combined with efficient transportation logistics which widely increase its availability. The same holds for ^{68}Ga and ^{90}Y, of which the use is not dependent on the availability of a cyclotron. However, the physical properties of the PET radioisotopes are quite different from ^{18}F. ^{18}F almost exclusively decays via positron emission (96.8%) and with a relatively low maximum energy of the positron of 0.6335 MeV. The maximum and mean range of ^{18}F are equal to 2.4 and 0.6 mm. The other 3% of decays is via electron capture [92].

The use of the generator-based isotope ^{68}Ga has seen a steady increase in the last years. It is obtained from a ^{68}Ge/^{68}Ga generator obviating the need for a cyclotron on site. One generator will typically be used for about 1 year [93] and the equilibrium between ^{68}Ga and ^{68}Ge is re-attained rapidly enough to allow multiple radiotracers preparations a day. ^{68}Ga is used for labeling both small compound and macromolecules, such as ^{68}Ga-PSMA targeting the prostate-specific membrane antigen or ^{68}Ga-labeled tracers targeting the somatostatin receptor expressed by neuro endocrine tumors, which are considered as key applications for combined PET/MR [94, 95, 96]. ^{68}Ga is not a pure positron emitter and has a more complex decay scheme than ^{18}F. Non-pure isotopes emit additional gammas that may even directly fall into the energy window accepted by the PET scanner. These high energy gammas have some probability of generating spurious coincidences after scattering in the patient or via e^+/e^- pair production in the detector or the patient [97, 98]. In 87.8% of the decays ^{68}Ga will emit a positron with a maximum energy of 1.899 MeV and a mean energy of 0.89 MeV with a halflife $t_{1/2} =$ 67.6 min. The much higher energy of the positron emission (compared to ^{18}F) leads to an increased maximum and mean range of 8.9 and 2.9 mm. It also emits additional gammas of 578.52 keV (0.034), 805.83 keV (0.094), 1077.35 keV (3.22), 1261.08 keV (0.094) and 1883.16 keV (0.137) (Note: number in parenthesis represents the mean energy, see A).

In the same way, ^{90}Y has gained attention in nuclear medicine for therapeutic and diagnostic applications. ^{90}Y is used in radioemboliza-

tion of liver tumors. Tiny glass or resin beads called microspheres are administered in the hepatic artery and are transported into the blood vessels at the tumor site. The spheres get physically trapped and the radioactive isotope ^{90}Y delivers a high dose (via electrons) of radiation to the tumor. Several centers also use their PET system to image the therapeutic isotope ^{90}Y. Studies have shown that ^{90}Y-DOTA and ^{90}Y-DTPA have a potential in intra-vascular radionuclide therapy and ^{90}Y can simultaneously work as an imaging agent and a therapeutic [16, 99, 100]. ^{90}Y is mainly a β^- emitter with a very small branching ratio for positron production. In 0.003186% of the decays there will be the emission of an e^+/e^- pair at 1.76 MeV. As the transition energy is 1.76 MeV, there remains 738 keV of kinetic energy to be split between the electron and the positron in order to conserve the null momentum. With a halflife of 64.1h, ^{90}Y produces a weak but useable PET signal [6, 15], as illustrated by several clinical and phantom studies.

Furthermore, these isotopes may be of particular interest for PET/MR in prostate cancer, liver studies and follow up of radionuclide therapy. Therefore, it is relevant to determine the performance of PET/MR for these clinically relevant and commercially available isotopes in order to ensure correct functionality and optimal image quality. For PET scanners in particular, the National Electrical Manufacturers Association (NEMA) has defined a standard to assess the performance of the tomographic system, which is widely accepted by manufacturers [101]. The NEMA NU 2-2007 standard identifies ^{18}F as the radionuclide to be used for all tests. Due to factors such as positron range, interference with magnetic field and non-pure emissions with additional gammas the results may be different when non-conventional radioisotopes, such as ^{68}Ga and ^{90}Y [102, 103] would be used.

The aim of this study is to assess the impact of using different PET isotopes for the NEMA Tests performance evaluation of the GE Signa integrated PET/MR. NEMA NU 2–2007 performance measurements for characterizing spatial resolution, sensitivity, image quality, accuracy of attenuation and scatter corrections (IQ), noise equivalent count rate (NECR) were performed using ^{18}F and ^{68}Ga. For ^{90}Y all tests except NECR tests were also performed.

3.2 Materials and Methods

All phantom experiments were performed on the MP24 version of the GE Signa integrated PET/MR whole-body hybrid system, installed in UZ Leuven, Belgium. The MR component of the hybrid system consists of a 3.0 Tesla static magnetic field, a radiofrequency (RF) transmit body coil and a gradient coil system which provides a maximum amplitude of 44 mT/m and a maximum slew rate of 200 T/m/s. The PET component is comprised of 5 detector rings, each consisting of 28 detector blocks. Total axial FOV is equal to 25 cm. Table 3.1 contains a summary of important design and performance parameters.

Tab. 3.1: Design and PET performance specifications.

	PET
Axial PET	25 cm
Transaxial FOV	60 cm
Photodetector	SiPM
Scintillator	LYSO
Crystal element size	25x4.0x5.3 mm3
Electronics	Integrated in-bore
Time resolution	<400 ps
Energy window	425-650 keV
Coincidence timing window	4.57 ns (± 2.29 ns)
NEMA NU 2-2007 PET test*	
Sensitivity	22.5 cps/kBq
Peak NECR	212.2 kcps
Activity at Peak NECR	18.1 kBq/ml
Scatter Fraction at Peak NECR	44.1 %
Spatial Resolution (Axial)	(5.53 – 6.95) mm @ 1 and 10 cm
* GE healthcare acceptance tests [101]	

The PET detectors are based on a Lutetium-based scintillator (LYSO) readout with MR-compatible Silicon Photomultiplier technology [23]. Before NEMA testing, a well counter calibration scan was performed with ^{18}F in a uniform cylindric phantom. As recommended calibration, the activity injected was measured using two dose calibrators (Capitec

- CRC-55tR) with settings for different isotopes. The following measurements were performed according to the NEMA NU 2-2007 protocol. In this study, we conveniently choose to evaluate the PET/MR using NEMA NU-2 2007 because GE Healthcare have reported their acceptance testing on this version [101].

3.2.1 Spatial Resolution

A high activity concentration of approximately 200 MBq/ml was used to generate point sources (drop of activity raised in a capillary). In total, more than 500,000 counts were acquired. Both axial and transaxial resolution were measured at two different positions in the axial z-direction: in the central position of the FOV and at a position a quarter of the total axial FOV away from the center. The source point position was adjusted until all x-y-z values fall between $\pm$ 2 mm from the required position. At each of these axial positions, the resolution was measured centrally in the FOV (1 cm horizontal offset relative to the center) as well as 10 cm horizontal offset and 10 cm vertical offset relative to the center. Data was reconstructed with filtered back-projection. The Full Width at Half maximum (FWHM) and Full Width at Tenth of Maximum (FWTM) of the point source response function in all three directions were determined by one-dimensional response functions along profiles through the image volume in three orthogonal directions. In order to report the limitation of the NEMA SR test, a new alternative approach using molecular sieve (with 2.5 mm of diameter), placed at the top of the capillary glass will be tested for ^{68}Ga.

3.2.2 Sensitivity

Sensitivity was tested with the NEMA sensitivity phantom, composed of a line source with 5 different thicknesses of aluminium. The 70-cm-long line source was filled with a volume of approximately 2.3 ml. The activity level was equal to 10.7 MBq and 8.7 MBq at scan start for ^{18}F and ^{68}Ga (ensuring that the scan acquired at least 2,000,000 counts). For ^{90}Y, the activity level was adjusted to 444.9 MBq, to compensate for the low positron abundance and to keep the scan time acceptable.

Using this activity, the total number of counts collected was above 2 million counts. This measurement was done in the center of the FOV and at 10 cm away from the center of the FOV. Data was collected for a period of time to ensure that at least 10.000 trues per slice were collected. The system sensitivity was calculated by fitting the decay corrected count rate of each acquisition to an exponential function of the aluminium thickness and extrapolating the value for a hypothetical acquisition with no aluminium tubes over the source (no attenuation). Axial sensitivity profiles were generated by calculating the sensitivity of each slice for the transaxially centered data acquisitions that used only the smallest aluminium tube.

3.2.3 Scatter fraction, Noise Equivalent Count Rate

A 70 cm long plastic tube line source (3.2 mm in inner diameter) was filled with a calibrated activity of 905 MBq and 871 MBq in a 5.0 ml of solution for ^{18}F and ^{68}Ga respectively. The line source was inserted 4.5 cm below the central axis of a 70-cm-long cylindrical polyethylene test phantom. The center of the NEMA scatter phantom was positioned at the FOV center and the data were acquired overnight. After wards twenty-nine frames of data were extracted from the list mode data, NEMA specifications were used to derive the trues, randoms, scatter, and NECR from the prompts dataset in each frame after a long overnight scan acquisition. The results were plotted as a function of effective activity concentration. In addition, the accuracy of count losses and randoms corrections was determined by extrapolating image results from low count rates (Note: the overnight NECR scan requires between 850 and 900 MBq of activity at the beginning of scanning).

3.2.4 Image Quality, Accuracy of Attenuation and Scatter Corrections

Image quality was measured by acquiring the NEMA image quality phantom. A 5 cm diameter cylindrical insert filled with styrofoam pellets was positioned in the center of the phantom to simulate lung tissue. The warm background volume of the phantom was filled with an activ-

ity concentration of 5.3 kBq/ml. Four hot spheres with diameters of 10, 13, 17, and 22 mm were filled with an activity concentration 4 x the background for ^{18}F and ^{68}Ga. For ^{90}Y a higher 8:1 ratio was used since typical contrasts in liver therapies are normally higher than 4:1. The two cold spheres with diameters of 28 and 37 mm were filled with water (except for the ^{90}Y image quality test, in which all of the spheres were filled with an 8:1 ratio of activity). Background activity from outside the scanner FOV was generated by a line source inserted into the same cylindrical phantom as used in the scatter fraction, count losses, and randoms measurement. It contains a 116 MBq solution of the isotope used in the measurement and was placed on the bed axially adjacent to the body phantom. The percent contrast recovery for the hot and cold spheres and the background variability were calculated, as defined in the NEMA standard. The percentage contrast recovery (in an ideal case = 100 %) is determined for each hot sphere j by Eq. 2.23. $C_{S,j}$ is the average counts of regions of interest (ROIs) on the spheres (a circular ROI with a diameter equal to the inner diameter of the sphere). These are positioned in the transverse image slice that contains the centers of the spheres. $C_{B,j}$ represents the average counts in the background ROI. The terms a_H and a_B are activity concentration in the hot spheres and background respectively. The phantom has also 2 large spheres which are not filled with isotope. For each non-radioactive sphere j the percentage contrast recovery $CR_{C,j}$ was calculated by Eq. 2.24. In order to determine the percentage background variability N_j as a measure for the image noise for sphere j (in an ideal case = 0 %), the following Eq. 2.25 was used. SD_j is the standard deviation of the background ROI counts for sphere j. In addition, the central cylinder of the phantom did not contain any activity, and the relative error was calculated to determine the accuracy of scatter and attenuation correction as described by Eq. 2.26. $C_{lung,i}$ is the relative error per percentage units for each slice i, $C_{lung,i}$ is the average counts in the lung insert ROI and $C_{B,i}$ is the average of the 60 (37 mm) background ROIs drawn for the image quality analysis [19].

Image-quality phantom images

The phantom data were obtained with a 10 min scan for ^{18}F and ^{68}Ga acquisitions. For ^{90}Y, a long 15h scan time and a shorter 30 min representing a clinical acquisition were obtained using list mode data selection. The image quality phantom was reconstructed in a volume of 89 images using Ordered Subset Expectation Maximization reconstruction algorithm (OSEM) including Time-Of-Flight (TOF) and scatter corrections with 2, 3, and 4 iterations of 28 subsets. The scatter correction for ^{68}Ga and ^{90}Y were defined as "dirty" emitters to account for the gamma photons. These isotopes allow an additional fitting parameter in the scatter tail scaling process [104]. All reconstruction schemes have a matrix size of 256 x 256 with 2.08 $\times$ 2.08 $\times$ 2.78 mm^3 voxel size including TOF information. In order to evaluate different reconstruction settings, the images were reconstructed using 2 mm and no post-smoothing filter with and without Point Spread Function (PSF). The GE PET/MR uses a system-generated approach that include a CT-based template attenuation correction for the NEMA IQ phantom.

3.3 Results

3.3.1 Effect of the 3T MR field on Spatial Resolution

The spatial resolution (FBP reconstruction) results for each isotope are presented in Table 3.2. As a double check, the ^{18}F-measured values (at the same equipment across all isotopes) was used as a reference for all measurements performed on the GE Signa PET/MR. The FWHM radial and tangential resolution is slightly degraded for ^{68}Ga and ^{90}Y.

In comparison with the ^{18}F measured values, the relative differences were 17.8% and -1.3% at 1 cm and 27.9% and 3.5% at 10 cm in the axial direction for ^{68}Ga and ^{90}Y respectively. With regards to the FWTM in the axial resolution at 1 and 10 cm off center, the percentage difference relative to ^{18}F values were 70%, and 3.3% at 1 cm and 57.3%, and 12.3% at 10 cm off center for ^{68}Ga and ^{90}Y respectively. Figure 3.1, shows the

Tab. 3.2: Spatial resolution tests: FHWHM and FWTM for 1 cm and 10 cm off center of FOV

FWHM (mm)	^{18}F	^{68}Ga	^{90}Y
At 1 cm			
Transverse*	4.05	4.18	4.42
Axial	6.08	7.16	6.00
At 10 cm			
Radial	5.75	5.80	5.79
Tangential	4.38	4.46	4.44
Axial	6.85	8.76	7.09
FWTM (mm)			
At 1 cm			
Transverse*	8.62	8.68	9.02
Axial	11.97	20.35	12.36
At 10 cm			
Radial	10.68	10.70	10.78
Tangential	8.61	8.78	8.84
Axial	14.01	22.04	15.73
* Transverse (radial and tangential values are averaged together).			

limitation of the NEMA SR test. The spatial resolution has increased for ^{68}Ga using the molecular approach by 9.1% and 19.2% at 1 cm and 10 cm off centre.

3.3.2 The primary factor for the Sensitivity

Sensitivity test results for ^{18}F, ^{68}Ga and ^{90}Y, are 21.8, 20.1, and 0.653 $\times 10^{-3}$ cps/kBq at the center position and 21.2, 19.7, and 0.667×10^{-3} cps/kBq at 10 cm off-center. Table 3.3 gives the measured average sensitivity values at the transaxial center and 10 cm off-center. Also, data are compared to the average ^{18}F measured and theoretical values.

These estimated values were calculated based on the difference in branching ratio relative to the ^{18}F. The sensitivity values are in line with the lower positron fraction of the isotopes.

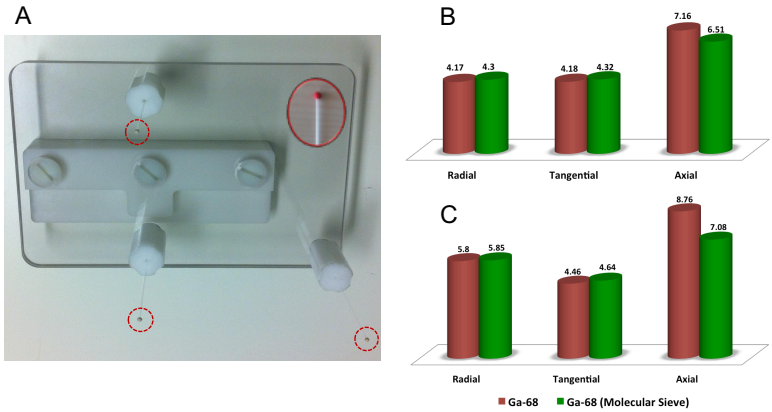

Fig. 3.1: Alternative approach to measure the SR using molecular sieve instead of capillary glasses for higher positron energy emitters, such as ^{68}Ga. (*A*) molecular sieve was placed in the SR phantom at the top of the capillary tube. Comparison of the SR results with and without using molecular sieve at 1 cm (*B*) and at 10 cm (*C*).

Tab. 3.3: Sensitivity test results: comparision between the average sensitivity measured and theoretical values relative to ^{18}F.

Isotope	Branching ratio	Average Sensitivity measured	Theoretical values (cps/kBq)*
^{18}F	0.968	21.5	-
^{68}Ga	0.879	19.9	19.5
^{90}Y	31.86×10^{-6}	0.66×10^{-3}	0.71×10^{-3}
* Values relative to ^{18}F measured value			

3.3.3 Count rate performance and accuracy measurements

The peak NECR, the corresponding activity concentration and scatter fraction at peak NECR are presented in Table 3.4 and Figures 3.2 and 3.3 for ^{18}F and ^{68}Ga. Table 3.4 summarizes the comparison between ^{18}F and ^{68}Ga in terms of scatter fraction at peak NECR, peak NECR, activity concentration at peak NECR, and maximum absolute error.

For ^{18}F the NECR has a maximum of 216.8 kcps at an activity concentration of 18.6 kBq/ml. At the peak, the scatter fraction was

Tab. 3.4: Scatter Fraction, peak NECR, and soucer activity test results for ^{18}F and ^{68}Ga.

Scan Type	Unit	Measured Values	
Isotopes		^{18}F	^{68}Ga
Scatter Fraction at Peak NECR	%	43.3	42.9
Peak NECR	kcps	216.8	205.6
Activity at Peak NECR	kBq/ml	18.60	20.40
Maximum Absolute Error	%	3.0	6.0

43.3 %, comparable to the results obtained on three separate scanners installed in three institutions [24].

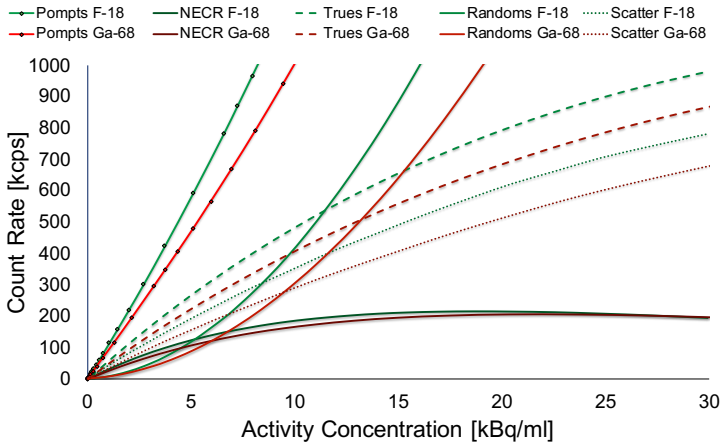

Fig. 3.2: NEMA counting rate measurements: count rates vs activity concentration for both radioisotopes ^{18}F and ^{68}Ga. Notice than peak of the NECR curve of ^{68}Ga is lower (at clinical NECR) and appears at higher activity concentrations.

For ^{68}Ga the trues, random and scatter count rates at the same activity concentration are lower in comparison to ^{18}F. The measured NECR peak for ^{68}Ga was also clearly lower and peaks at 205.6 kcps. This peak is obtained at a higher activity concentration of 20.4 kBq/ml. The scatter fraction at peak NECR was below 1% lower compared to value measured for ^{18}F (Figure 3.3 and Table 3.4). After the full 15h acquisitions (for both isotopes) the maximum absolute value of the slice error was 3.0% and 6.0% for ^{18}F and ^{68}Ga.

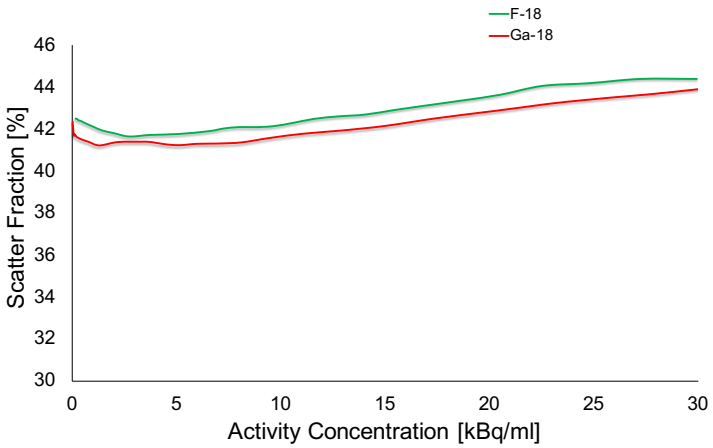

Fig. 3.3: NEMA counting rate measurements: scatter fraction vs activity concentration for both radioisotopes ^{18}F and ^{68}Ga

3.3.4 Image Quality: Positron range effect

The results for contrast recovery versus sphere diameter of the image quality phantom are shown in Figures 3.4 and 3.5. In the Figure 3.4A, the contrast recovery of the reconstructed image of the phantom without PSF and post-smooth filter was lower for ^{68}Ga and ^{90}Y as shown in Figure 3.5A the relative difference to ^{18}F measured values.

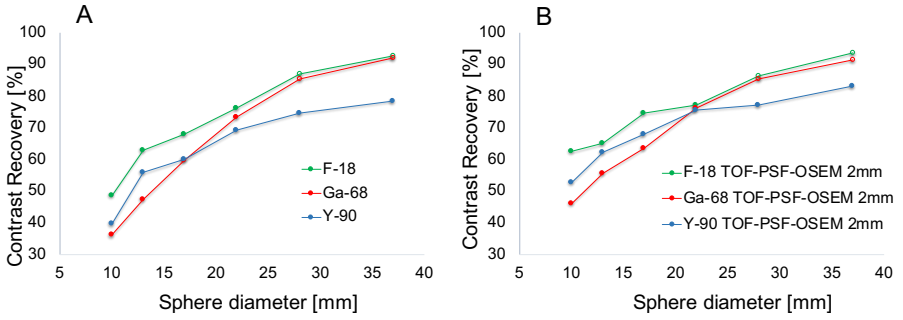

Fig. 3.4: Contrast recovery of TOF-OSEM 4 iteration and 28 subsets as a function of sphere size for 10 min (^{18}F and ^{68}Ga) and 15 h (^{90}Y) acquisition times and different isotopes. The cold and radioactive spheres are indicate using open (^{18}F and ^{68}Ga) and filled circles (^{90}Y), respectively. **A** without PSF and post-smoothing filter and **B** with PSF and 2 mm post-smoothing filter

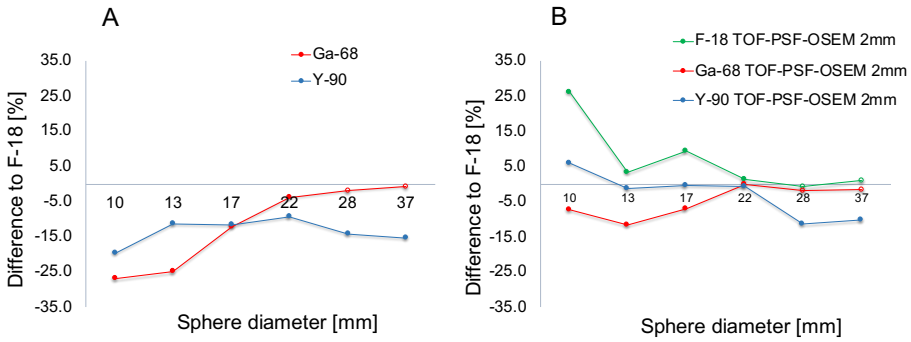

Fig. 3.5: Percentage difference relative to ^{18}F for each sphere size: **A** without PSF and post-smoothing filter and **B** with PSF and 2 mm post-smoothing filter. (Note: *(A)* The contrast recovery is affected by the mean magnetic field, the CR difference relative to ^{18}F is higher for the CR of the small spheres. *(B)* The resolution modelling improves CR.)

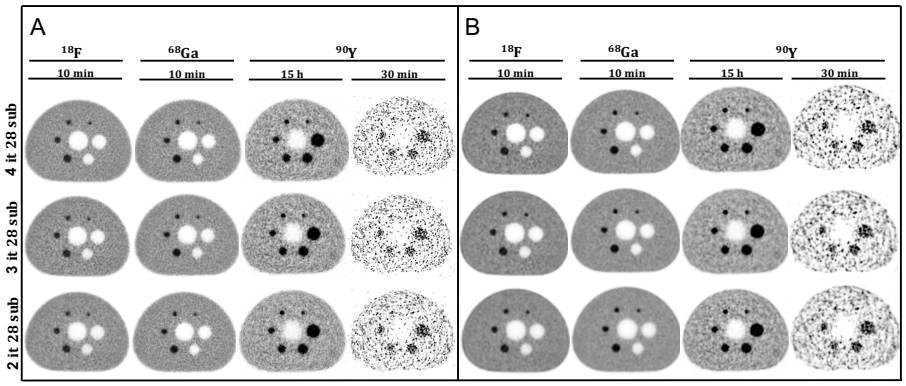

Fig. 3.6: Axial slices of the phantom reconstructed using TOF-OSEM for 2, 3, and 4 iterations and 28 subsets for different acquisition times and different isotopes: **A** without PSF and post-smoothing filter and **B** with PSF and 2 mm Gaussian filter.

The contrast recovery increased when compared using TOF, PSF and post-smooth filter, as showed in Figures 3.4B and 3.5B. The background variability, and the lung region relative error for ^{18}F, ^{68}Ga and ^{90}Y are shown in Table 3.5 for different sphere sizes. ^{90}Y has a much lower image quality and suffers from low counts. The residual lung error is clearly higher than for ^{18}F and ^{68}Ga. This is also visually confirmed by the clinical reconstructions (30 min acquisition) in Figure 3.6.

When compared in terms of number of iterations (Figure 3.6), the noise level increased with increasing the number of iterations for all isotopes.

Tab. 3.5: Background variability and residual lung error of TOF-OSEM 4 iteration and 28 subsets image reconstructed, with and without PSF and 2mm post-smooth filter for ^{18}F, ^{68}Ga, and ^{90}Y respectively.

	*TOF-OSEM			TOF-PSF-OSEM 2mm		
	^{18}F	^{68}Ga	^{90}Y	^{18}F	^{68}Ga	^{90}Y
Background Variability [%]						
10 mm	6.1	7.5	9.0	7.4	7.2	8.6
13 mm	5.0	5.8	7.9	6.2	6.0	7.7
17 mm	4.2	4.4	7.0	5.0	4.7	6.9
22 mm	3.3	3.3	6.3	4.0	3.5	6.2
28 mm	3.1	2.7	5.9	3.6	2.6	5.7
37 mm	2.7	2.1	4.9	3.0	2.0	4.7
Lung Error [%]	1.6	1.1	6.4	1.4	1.0	4.3
*4 iterations and 28 subsets						

3.4 Discussion and future work

The aim of this study was to assess the impact of using different PET isotopes for the NEMA Tests performance evaluation of the GE Signa integrated PET/MR. The performance and characteristics of PET/MR have been investigated based on NEMA NU-2 2012 with regard to ^{18}F [102, 103, 105], but not for different PET isotopes. Furthermore, the NEMA NU-2 2012 version is only slightly different from the 2007 version. The most substantial changes are relatively minor, mostly designed to make the test easier to conduct, more reproducible, or more clearly defined [101]. In this study, we conveniently choose to evaluate the PET/MR using NEMA NU-2 2007 because GE Healthcare have reported their acceptance testing on this version [105].

The system performance of the GE Signa integrated PET/MR was substantially different, in terms of NEMA spatial resolution and image quality for ^{68}Ga and ^{90}Y PET imaging test as compared to ^{18}F. In the transverse plane the magnetic field reduces the effective positron range, the dominant factor on spatial resolution seems to be the detector pixel size and the transverse resolution is therefore comparable with the result of ^{18}F. This effect was confirmed by other studies with simulations for different isotopes and field strengths [52, 106]. The main magnetic field along the axial direction leads to an increased positron range in this direction and a pronounced reduction of the range in the transversal plane for high-energy positrons. On the other hand, the positron range effect of the magnetic field is not significant for ^{18}F [107] and no significative effect was found for ^{90}Y. In agreement with these studies, the FWHM difference relative to ^{18}F measured values were 17.8% and -1.3% at 1 cm and 27.9% and 3.5% at 10 cm off center in the axial direction for ^{68}Ga and ^{90}Y respectively, as shown in Table 3.2. However, the NEMA spatial resolution test is designed to characterize the detector, rather than the isotope, which leads to limitations to account for the effect of magnetic field on positron range on the transaxial resolution measurements. The capillary is very small, and any positron that escapes the capillary is not accounted for in the measurements. In addition, axially the annihilation could occur in the tube sealing compound and beyond that, the axial test is slightly poor due the rebinning process and larger pixel size in the z-axis. On the other hand, the spatial resolution has increased for ^{68}Ga using the molecular approach by 9.1% and 19.2% at 1 cm and 10 cm off centre. In the last version of the NEMA NU 2-2018 protocol, the spatial resolution test point source is specified in terms of point source dimensions as opposed to capillary tube dimensions. The capillary tube now is specified as an option [46]. The NEMA image quality test was also substantially different in the measured contrast recovery, as shown in Figures 3.4 and 3.5. It seems that the inferior resolution also affects the contrast recovery of the radioactive spheres in the NEMA quality phantom for ^{68}Ga and ^{90}Y. While the results look visually (Figure 3.6) similar between ^{18}F and ^{68}Ga for TOF-OSEM without resolution modelling and post-smooth filter, there is (Figures 3.4A and 3.5A) a clearly lower contrast recovery for the smaller spheres in ^{68}Ga and also lower

contrast recovery in ^{90}Y, which is probably caused by the increased positron range and loss in resolution. A similar approach using different PET isotopes in a brain phantom measured at different field strengths was conducted by Shah et al. [107]. The contrast of the reconstructed image of the brain phantom filled with ^{68}Ga was significantly affected by the magnetic field in the axial direction more than ^{18}F (low-energy positron emitter). At the current time, GE PET/MR system allows a extra fitting parameter for radionuclides labelled "dirty" in the reconstruction settings. However, errors in scatter correction and the use of different sphere to background ratios might have influenced these results [23, 108, 109, 110]. A low-frequency offset of the data makes the images appear to have more or less contrast recovery. And different ratios lead to different contrast recovery. This can explain the crossing of the ^{90}Y curve (ratio 8:1) in Figure 3.4. Regarding the noise level and the average lung residual error (Table 3.5), the results were comparable between ^{18}F and ^{68}Ga, but for ^{90}Y the background variability and the lung error are clearly higher than for ^{18}F and ^{68}Ga, which is also visually seen (15h and 30 min acquisition) in Figure 3.6. However, when comparing the reconstructed images using resolution modelling and 2 mm post-smooth gaussian filter to reduce the noise, the contrast recovery increased with acceptable noise level, as shown in Figure 3.4B and 3.6B. Although high-energy positron emitters are affected by the field strengths, recent developments in reconstruction methods including dedicated positron range correction have successfully corrected this effect [111]. A new Bayesian penalized likelihood reconstruction algorithm which uses a block sequential regularized expectation maximization as an optimizer (including TOF and PSF), was introduced in the last few years by GE Healthcare (Q.Clear) on their PET scanners in order to improve clinical image quality. Unlike traditional OSEM reconstruction, which increases the noise with the number of iterations (Figure 3.6), this algorithm improves image quality by controlling noise amplification during image reconstruction [30]. The performance characteristics of Q.Clear will be tested in Chapter 5. The mean sensitivity results shown in Table 3.3 are in line with theoretical values as expected for ^{68}Ga and ^{90}Y test. The primary factor for the sensitivity change is the scale factor related to the positron emission fraction (96.7%, 87.9%, 0.003186%

for ^{18}F, ^{68}Ga, and ^{90}Y respectively). The low branching ratio of ^{90}Y explains the substantial quality difference of the reconstructed transverse image quality phantom as compared with ^{18}F and ^{68}Ga images, as shown in Figure 3.6. Several design factors (Table 2) including Compton scatter recovery [30, 21], the longer axial FOV and reduced detector ring diameter lead to higher count rates and an increased sensitivity, both in stand-alone operation and with simultaneous MR image acquisition [112]. NEMA count rate performance and accuracy measurements summarized in Table 3.4 and Figure 3.2, suggest that the scanner provides excellent accurate quantitative measurements and utilizes effective randoms and dead time correction methods for ^{18}F [108]. For ^{68}Ga, the scatter fraction at NECR peak (Table 3.4 and Figure 3.3) was slightly lower compared to values measured for ^{18}F. This is primarily due to the fact that 1.2% (1.883 MeV) fraction of ^{68}Ga that decays by β^+ results in a prompt gamma (1.077 MeV) [97, 98] contamination into the PET data. The prompt gammas of ^{68}Ga can directly fall into the energy window and be accepted by the PET scanner. This happens when the 1.077 MeV scatters in the phantom and generates an energy falling in the main energy window. In this case there will be a coincidence with a true 511 keV resulting from the same decay [15]. Contributions in which only the gamma is detected would add to randoms which does not affect the calculation for scatter fraction. The ^{68}Ga NECR test was clearly lower than measured for ^{18}F and appears at a slightly higher activity concentration (Figure 3.2). The lower peak NECR can be explained by the additional 1.077 MeV gamma which leads to additional detections increasing the deadtime of the detector blocks. These can also lead to additional randoms or scatter when they lose enough energy for falling into the energy window. However, the effect from these prompt-gammas is clearly very small from a scatter fraction perspective and for all activity concentration values below NECR (Table 3.4), the maximum absolute value of the slice error is 2.9% and 6.0% for ^{18}F and ^{68}Ga, respectively. There is also no appreciable impact in the measured residual activity of the lung insert in the IQ phantom (Table 3.5).

In summary, the overall GE Signa PET/MR system performance with TOF capability based on SiPM detectors, shows substantially different system characteristics for each of these commercially available

isotopes. However, the NEMA spatial resolution test is designed to characterize the detector, rather than the isotope, which needs to be adapted in order to well account for the effect of magnetic field on positron range on the transaxial resolution measurements. The variety of prompt gammas in coincidence of these isotopes and the interference of the MR field on positron range however, seems to have been compensated by the PET scanner technologies, which, in combination with recently developments in reconstruction methods (regularized TOF OSEM and PSF), lead to a comparable noise-equivalent count rate and a good scatter fraction.

3.5 Conclusion and original contribution

NEMA NU 2–2007 performance measurements using ^{18}F, ^{68}Ga, and ^{90}Y resulted in substantially different system characteristics, specifically in terms of spatial resolution and recovery coefficients of the image quality measurements. NEMA spatial resolution test needs to be adapted in order to correctly account for the difference in positron range in the transaxial resolution measurements. And when NEMA image quality test is compared using TOF-OSEM-PSF and post-smooth gaussian filter, the contrast recovery increased with acceptable noise level. The primary factor for the sensitivity change can be explained by the scale factor related to the positron emission fraction of the isotopes. Scatter fraction and NECR differences between the ^{18}F, ^{68}Ga are relatively small: for ^{68}Ga the peak NECR is lower and appears at higher activity concentrations. The maximum absolute value of the slice error is 2.9% and 6.0% for ^{18}F and ^{68}Ga respectively. These performance results are compensated by the PET scanner technologies and reconstructions methods.

The work described in this chapter resulted in several conference [113, 114, 115, 116, 117] publications and a *Springer Nature* - EJNMMI Physics publication [118].

4

GATE Monte Carlo model of the PET/MR: Modelling and Validation

In the previous chapter, the NEMA tests were performed on the GE Signa PET/MR system using different radioisotopes and those results will be used to validate our GATE Monte Carlo model. In this chapter, a realistic GATE Monte Carlo model of the PET/MR and the NEMA test are modelled and validated. This model is use to predict the NEMA performance of the GE Signa PET/MR for other radioisotopes and to evaluate the effect of the MR field on positron range.

4.1 Introduction

The simultaneous image acquisition of combined PET and MRI was first developed for small animal imaging in the late 90s [119] whereas the application in humans dates from a decade ago [120]. The development of compact PET detectors based on silicon photomultipliers (SiPMs) made it possible to integrate PET detector rings into the bore of an MR scanner and to develop fully integrated PET/MR systems, such as the GE Signa PET/MR [23, 37, 121].

Other than the advantage of simultaneous imaging in comparison to the PET/CT systems, the magnetic field could affect the positron range influencing the spatial resolution of the PET. The positron range stands for the distance from the emitting nucleus to the annihilation point with an electron and its value is proportional to the energy of the positron. A charged particle in a magnetic field with a strength, in the

order of some Tesla, will describe a helical path around the magnetic field lines, therefore reducing the positron range in the plane transverse to the magnetic field [106, 122].

Most of the studies done in PET are based on ^{18}F because it is the most relevant isotope in the clinic [92]. However, with the increasing clinical relevance of other radioisotopes, such as ^{15}O, ^{13}N, ^{11}C, ^{82}Rb and especially ^{68}Ga, the need arises to assess the scanners' performance with these radioisotopes due to their different decay scheme and physical properties. ^{18}F almost exclusively decays via positron emission with a branching ratio of 96.8% and has a relatively low maximum positron energy (0.6335 MeV). Properties of ^{15}O, ^{13}N, ^{11}C, are in line with ^{18}F properties and are considered pure β^+ emitters, with the probability of positron emission being close to 100% and with a maximum energy of 1.735 MeV, 1.198 MeV and 0.960 MeV respectively. On the other hand, ^{82}Rb and ^{68}Ga have more complex decay schemes with multiple positron emission branches with different energies and with a significant contribution of prompt gamma emissions [6, 93, 94]. In addition, these PET radioisotopes also have higher positron energies of 3.381 MeV and 1.8991 MeV respectively (energy of the most abundant positron). The impact of a high magnetic field during PET scanning needs to be evaluated, especially for high energy positron emitters.

Among the test most widely used, and accepted by the manufactures to evaluate a PET scanner capability, are the sensitivity and Noise Equivalent Count Ratio (NECR) tests. Sensitivity expresses the fraction of coincidences due to β^+ decay that is registered by the PET system for low activity concentration. NECR is an estimation related to signal-to-noise ratio and evaluates the impact of increasing the radiotracer dose on the PET signal. The aim of this study is to assess the impact of using different PET isotopes for the sensitivity and NECR performance evaluation of the GE Signa PET/MR and to investigate the effect of the magnetic field on the positron range of different PET radioisotopes. These figures of merit have been evaluated under the NEMA NU 2–2012 protocol [101].

This work has three blocks: (*A*) Develop a realistic GATE Monte Carlo model of the GE Signa integrated PET/MR (*B*) Validation of the model with the measured sensitivity and Noise Equivalent Count Rate

(NECR) under the NEMA NU 2–2012 on a 3T GE Signa PET/MR using ^{18}F and ^{68}Ga taken from [118]. (*C*) Use the GATE-model to predict the performance of the system for the isotopes ^{18}F, ^{11}C, ^{15}O, ^{13}N, ^{82}Rb, ^{68}Ga and to evaluate the effect of the 3T-MR field on positron range.

4.2 Material and Methods

The MR component of the GE Signa PET/MR system has a static magnetic field of 3.0 tesla with a maximum radiofrequency amplitude of 44 mT/m and a maximum slew rate of 200 T/m/s. The PET consists of 5 rings of 28 detectors ($25 \times 4.0 \times 5.3$ mm^3) based on lutetium-yttrium-oxyorthosilicate crystals with MR-compatible SiPM technology [27]. The composition results in a FOV of 25 and 60 cm in the axial and transaxial direction respectively. NEMA NU 2–2012 performance measurements using ^{18}F resulted in slightly different system characteristics compared to the other isotopes due to their physical properties. All results were compared to the acceptance testing results from literature data on a similar GE Discovery MI PET/CT system with 5-rings and on GE Signa PET/MR system for ^{18}F as shown in Table 2.4. The absolute sensitivity and NECR for ^{18}F, ^{11}C, ^{15}O, ^{13}N, ^{82}Rb and ^{68}Ga radioisotopes were estimated according to the NEMA test phantoms. The results were validated with published and measured values.

4.2.1 GATE simulations

Monte Carlo simulations were implemented in GATE and run on the high-performance computer *Vlaams Supercomputer Centrum* installed at Ghent University. GATE is a toolbox based on Monte Carlo simulations adapted for nuclear medicine applications [83].

4.2.2 GE Signa PET/MR Model

A model of the GE Signa Integrated PET/MR was implemented in GATE. The system has an axial and transaxial field-of-view of 25 cm and 60 cm respectively, an LYSO scintillator with crystal elements of

25 x 4.0 x 5.3 mm^3, uses an energy window of 425-650 keV and a coincidence window of 4.57 ns ($\pm$2.29 ns). The geometry was modelled using the cylindrical PET system in GATE, considering foam, plastic and copper shielding between the field of view and the detectors. The simulated system was used to calculate the annihilation distribution of the positrons in different tissues and includes the following physical processes: positron decay, multiple scattering, ionization, bremsstrahlung and electron annihilation. To characterize the effect of the 3 T MR field on the positron range, we simulated point sources of positron-emitting radionuclides including ^{18}F, ^{11}C, ^{15}O, ^{13}N, ^{82}Rb and ^{68}Ga positioned in the middle of a homogeneous 20 x 20 x 20 cm^3 cube with different tissue media (soft-tissue, lung-tissue and bone). For each isotope, 5 million events were simulated with and without a 3T-MR field applied in the z-direction (axial). The positron energy and the decay schemes of each radioisotope are shown in appendix A.

4.2.3 Sensitivity test

Sensitivity measurements were performed according to the NEMA NU 2–2012 protocol [101]. The sensitivity test is performed at two different locations in the FOV by multiple measurements of a 700 mm long source filled with low levels of activity while successively adding aluminum layers. The line source is placed inside the NEMA sensitivity phantom that consists of an aluminum cylinder of 2.5 mm thickness with accumulated 2.5 mm aluminum sleeves surrounding the line source. The low activity level minimizes random counts and effects of system dead time while the dense aluminum shielding of the source assures sufficient annihilation events to measure the PET signal.

Sensitivity is calculated by extrapolating to the attenuation-free count rate via exponential regression of the five measurements using the Eq. 2.17, discussed in Chapter 2. The simulations consisted of a low activity (5 MBq) line source, firstly positioned in the center of the FOV and secondly at a radial distance of 10 cm from the center. To measure the sensitivity, five different simulations with successive combined sleeve thickness (1, 2, 3, 4 and 5 sleeves) around the line source were acquired and the trues only count rate was obtained for each simulation. This

procedure is done for simulations at the center of the FOV and with a 10 cm radial offset from the center. The final reported sensitivity value is the average of both values. The sensitivity values at different readout levels were compared to the sensitivity profile measured on the scanner.

Post-processing sensitivity data

ROOT's "*Coincidences*" tree stores pairs of Singles that meet the conditions specified in the digitizer. Each pair is identified by an *eventID* for each particle (*eventID1* and *eventID2*), which identifies the radioactive decay the Singles comes from. Furthermore, the entire history for each particle of the pair is recorded, from their original position's coordinates to the interactions (Compton or Rayleigh scattering effect) they suffer before reaching the detector. A coincidence is considered to be random when the *eventID* for particle 1 differs from particle 2. When they are equal, a coincidence can still be considered scattered or true. True coincidences are obtained after checking for any Compton or Rayleigh scattering. When a true coincidence is found, its position along the z-direction (the position of where the radioactive decay took place) is stored into a 1D histogram, which can be used later to obtain an axial sensitivity distribution, or profile, for the scanner.

4.2.4 Noise equivalent count rate test

NECR is measured with a 700 mm long and 203 mm wide polyethylene cylinder over several levels of activity and thus considers the random counts and scanner dead time. Through a sinogram-based analysis, the peak NECR, corresponding activity and scatter fraction can be extracted from these measurements [101]. The scatter fraction was assessed by simulating a polyethylene cylinder containing a 70 cm long plastic tube line source (3.2 mm inner diameter) with high activity. To simulate the NECR in GATE, the activity in the line source was acquired using a total of 11 different activity levels (varying from 1 to 800 MBq) in order to reduce the computational time. The number of scattered and total coincidences was estimated for each slice as the integral of the summed radial profiles, as prescribed by the NEMA protocol.

Post-processing NECR data

The analysis is based on sinograms and is aimed at estimating the rate at which the scanner acquires coincidence data, be it true, random, or scattered coincidences. The sinogram data consists of the angle and the displacement of the LOR. The GATE output file ('.dat') file containing the columns of data are then read into MATLAB as a 2D matrix and transformed into a 2D histogram with 320 bins for the angle information in the vertical axis, which varies from 0 to π, and 640 bins for the displacement data in the horizontal axis, varying from -300 to 300 for the GE Signa. All the steps of the post-processing data are shown in Figure 4.1.

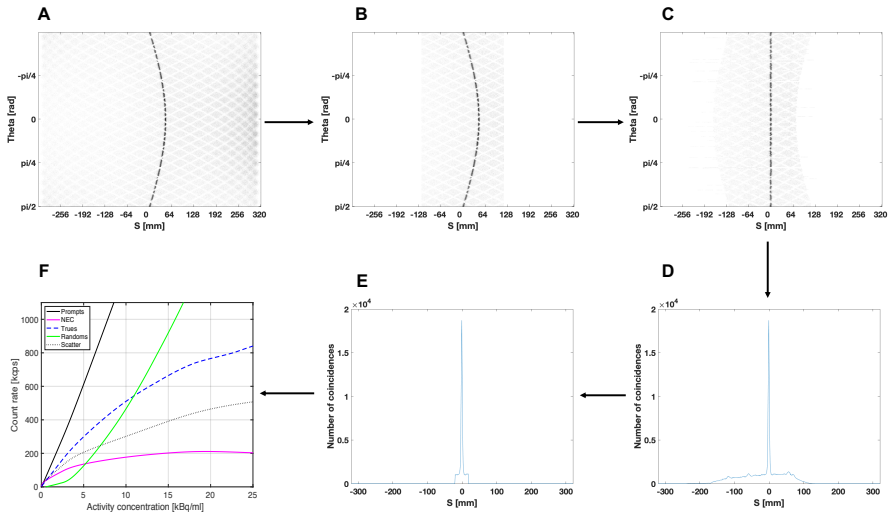

Fig. 4.1: Post-processing NECR data: *A* - Extract in ROOT the sinogram data for each coincidence, *B* - Set to 0 all pixels located further than 12 cm away from the center of the FOV, *C* - Sinogram after alignment according to the maximum values for each projection angle, *D* - Sum each projection of the sinogram, *E* - Select a 40 mm wide strip to Estimate random + scatter counts, *F* - Compute Scatter Fraction, Count Rates and NECR.

NEMA prescribes an alignment of the sinogram by finding the maximum value of the pixel for each projection, and shifting each angle so that the maximum value is at the center of the sinogram, with $S = 0$ *mm*, as shown in Figure 4.1C. After alignment, pixels in every projection

angle that have the same displacement are summed in order to obtain a sum projection, according 4.1.

$$C(r)_{i,j} = \sum \theta(r - S_{max(\theta),\theta})_{i,j} \tag{4.1}$$

where r is the pixel, θ is the projection, and S_{max} represents the location of the pixel with the maximum value in each projection, as shown in Figure 4.1D. In order to estimate the background counts, the NEMA procedure filters the sum projection of the total coincidences into a 40 mm wide strip (Figure 4.1E). The value of the left and right bins at the edge of the curve are then averaged and multiplied by the number of pixels in the strip. By adding this value to the number of coincidences outside the strip, the number of random plus scatter counts, C_{r+s} (see Chapter 2, section 2.4.4), is obtained.

4.2.5 Positron range evaluation

The GATE-model was also used to simulate the influence of the magnetic field on the positron range for lung tissue (0.26 g/cm3^3), soft tissue (1.00 g/cm3^3), bone (1.42 g/cm3^3) and for commercially available isotopes. To characterize the effect of the 3T-MR field on the positron range, we simulated point sources of positron-emitting radioisotopes including ^{18}F, ^{11}C, ^{15}O, ^{13}N, ^{68}Ga, and ^{82}Rb positioned in the middle of a homogeneous 20 x 20 x 20 cm^3 cube with different tissue media (soft-tissue, lung-tissue and bone). The point source was also positioned at the boundary of the lung and soft tissue. For each radioisotope, 5 million events were simulated with and without the 3T-MR field applied in the z-direction (axial).

The three-dimensional (3D) range of each recorded positron is calculated according to Eq 4.2, looping over the individual coordinate (x,y,z) variables.

$$R = \sqrt{x^2 + y^2 + z^2} \tag{4.2}$$

The mean 3D positron range is obtained using *numpy* function.

4.3 Results

The simulated results were compared to the NEMA measured values on the PET/MR published in Chapter 3.

4.3.1 GATE-model of the GE Signa PET/MR

The GATE-model of the GE Signa PET/MR including the MR-body (grey) and NEMA phantoms with the activity isotopically distributed on a 70-cm-line source (red) are presented in Figure 4.2 according to NEMA NU 2-2012 protocols.

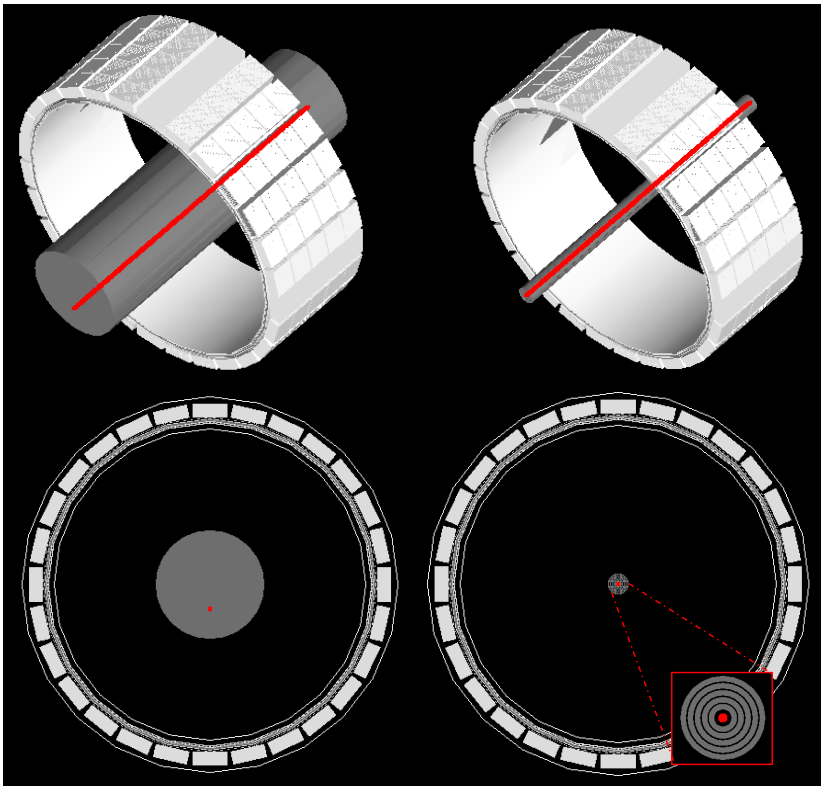

Fig. 4.2: Visualization of the GATE-model of the GE Signa PET/MR system including the NEMA sensitivity and NECR phantoms (*upper*) with a 70-cm-line activity source (*red*).

We have modelled the GE Signa PET/MR using GATE for Monte Carlo simulations. The simulated results were compared with published and measured NEMA sensitivity and NECR results for ^{18}F and for ^{68}Ga taken from Chapter 3.

4.3.2 Sensitivity

The results obtained for the simulated sensitivity measurement performed on GE Signa PET/MR with a 3T MR field using a ^{18}F and ^{68}Ga sources, (21.2 cps/kBq and 19.2 cps/kBq, respectively) are comparable to values measured following the NEMA protocols, 21.5 cps/kBq and 19.9 cps/kBq respectively as shown in Table 4.1.

Tab. 4.1: Sensitivity test results for ^{18}F and ^{68}Ga at 0 cm and 10 cm off center. These results are compared to the 18F and ^{68}Ga-measeured values [118]

	Measured (cps/kBq)		Simulated (cps/kBq)	
	0 cm	10 cm	0 cm	10 cm
^{18}F	21.831	20.063	21.205	21.112
^{68}Ga	21.173	19.689	19.098	19.017

Tab. 4.2: Averaged (1 cm and 10 cm off center) sensitivity test results for different isotopes [118]

	Branching Ratio (%)	Measured (cps/kBq)	Simulated (cps/kBq)	Theoretical values (cps/kBq)
^{18}F	96.76	21.5	21.2	
^{15}O	99.89	-	20.9	22.20
^{13}N	99.82	-	21.5	22.18
^{11}C	99.75	-	21.1	22.16
^{82}Rb	95.45	-	20.3	21.21
^{68}Ga	87.90	19.9	19.2	19.53

Table 4.2 shows the average of the simulated NEMA sensitivity test for ^{18}F, ^{15}O, ^{13}N, ^{82}Rb, ^{68}Ga at the transaxial center and 10 cm off-center. The theoretical values were calculated based on the 21.5 cps/kBq sensitivity measured value for ^{18}F taken from Chapter 3 and taking

into account each radioisotopes' total positron branching ratio. The simulated sensitivity values are in line with the measured and theoretical values for ^{18}F and ^{68}Ga. Thus validates the simulation model.

There is a limitation regarding the annihilation in the sensitivity phantom's attenuation layers, which significantly affects the regression method used to estimate the attenuation-sensitivity for ^{82}Rb. Figure 4.3A shows the limitation regarding the measurement with the first attenuation layer, that falls outside the trend of the rest of the measurements.

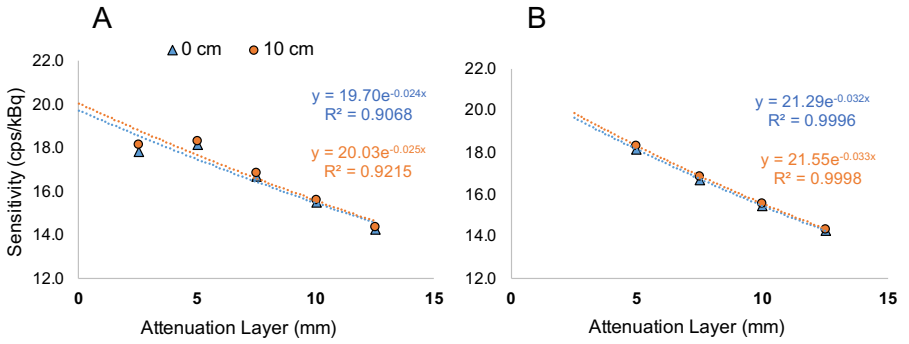

Fig. 4.3: Sensitivity data plotted against the accumulated attenuation layer thickness and exponential regression for ^{82}Rb. In *A* and *B* - Show the fitted equation and coefficient of determination for simulations at the center of the FOV (0 cm, blue) and for 10 cm radially off center (10 cm, orange) with 5 attenuation layers and with 4 attenuation layer, respectively.

Figure 4.3B, shows the attenuation-sensitivity profile without the first attenuation layer measurement and extrapolated the sensitivity based on the other measurements. The average sensitivity value (0 and 10 cm values) increased in Figure 4.3B to 21.4 cps/kBq, compared to 19.8 cps/kBq when measured with 5 layers (Figure 4.3A). NEMA sensitivity test needs to be adapted for ^{82}Rb.

4.3.3 Noise equivalent count rate

The results for the measurements of peak NECR, the corresponding activity concentration and the scatter fraction at peak NECR for ^{18}F, ^{11}C, ^{15}O, ^{13}N, ^{82}Rb, ^{68}Ga are presented in Table 4.3.

Tab. 4.3: Measured and simulated scatter fraction, peak NECR and source activity for different isotopes.

	Scatter Fraction at Peak (%)	Peak NECR (kcps)	Activity at Peak NECR (kBq/ml)
^{18}F [118]	43.3	216.8	18.60
^{18}Ga [118]	42.9	205.6	20.40
^{18}F	38.8	216.8	17.4
^{15}O	38.8	216.4	18.2
^{13}N	38.2	212.0	16.5
^{11}C	38.5	217.6	16.7
^{82}Rb	39.1	173.5	19.6
^{68}Ga	38.7	207.1	20.1

This table summarizes the comparison between simulated and measured values taken from PET/MR data in Chapter 3. Figure 4.4 shows the true, random and scattered coincidence rates as a function of the activity concentration. The curves and the acceptability of the test are presented for ^{18}F, ^{15}O, ^{13}N, ^{82}Rb, ^{68}Ga.

NEMA count rate statistics simulation results for ^{18}F and ^{68}Ga are in agreement with published, measured values in Chapter 3, thus validating the built GATE model, as well as the analysis method. ^{11}C, ^{13}N and ^{15}O offer similar results to ^{18}F in terms of peak NECR and scatter fraction.

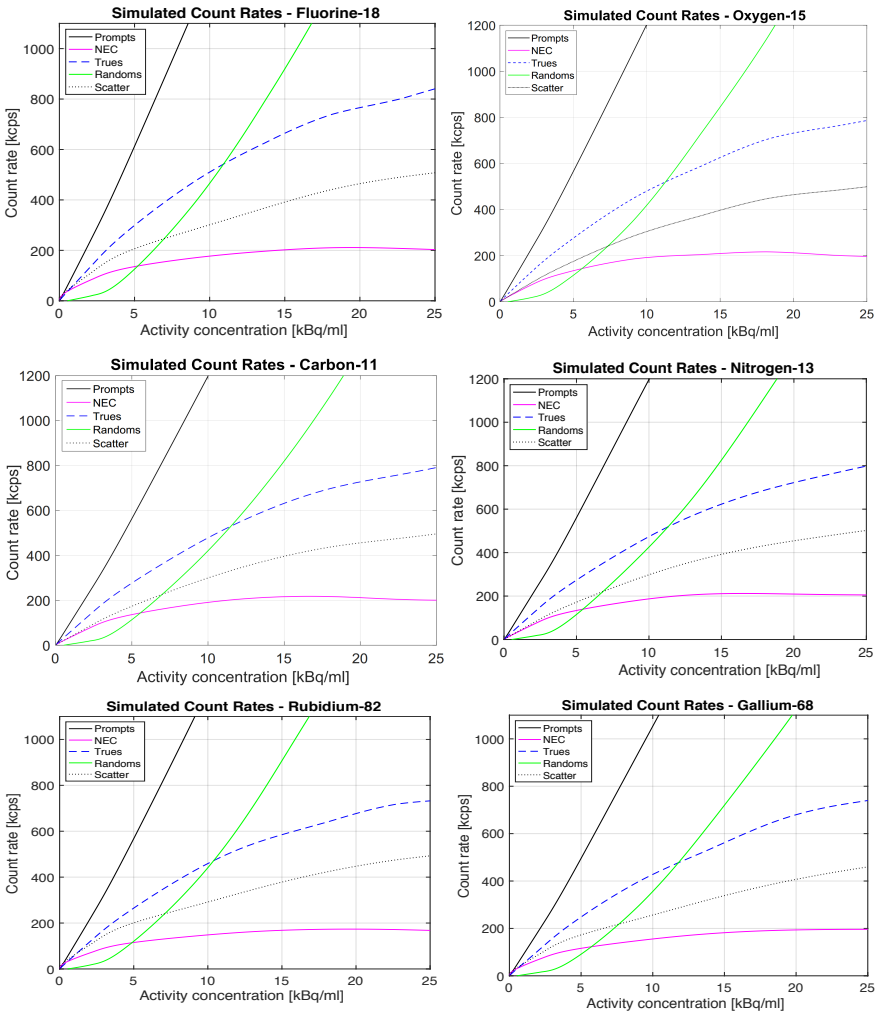

Fig. 4.4: Simulated NEMA count rates test for ^{18}F, ^{15}O, ^{11}C, ^{13}N, ^{82}Rb and ^{68}Ga, as a function of the activity concentration.

4.3.4 Positron range evaluation

The positron range of the high energetic radioisotopes was substantially affected by the 3T magnetic field. The variation of mean range between different tissues is enormous, especially in the case of lung-tissue, compared to soft-tissue and bone. The effect is more noticeable for high positron energy emitters, such as ^{15}O, ^{68}Ga and ^{82}Rb, reducing the range

in the transverse plane (x/y-direction) by a factor 3-4 when compared to the range in z-direction in lung-tissue. The transversal (x/y-directions) and axial (z-direction) positron range values are presented on Figures 4.5, 4.6, 4.7 and Tables 4.4, 4.5 and 4.6.

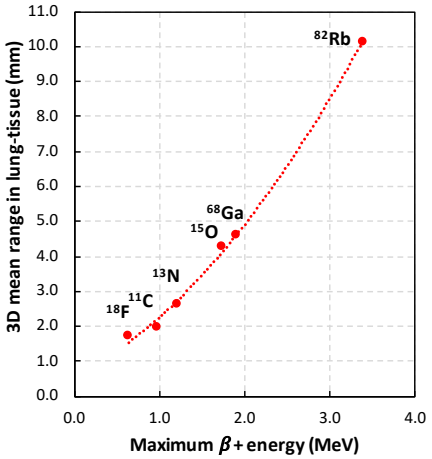

Fig. 4.5: Simulated 3D mean positron range for lung-tissue in a 3T static magnetic field.

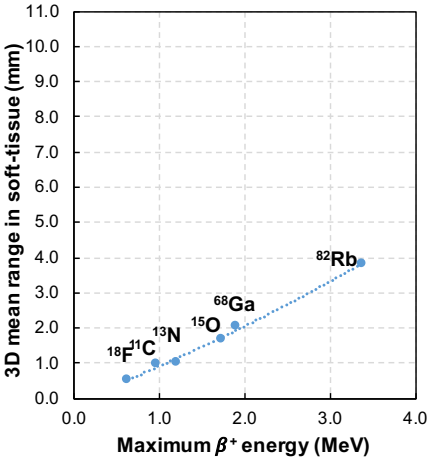

Fig. 4.6: Simulated 3D mean positron range for Soft-tissue in a 3T static magnetic field.

While significant changes are seen in the transversal plane, the mag-

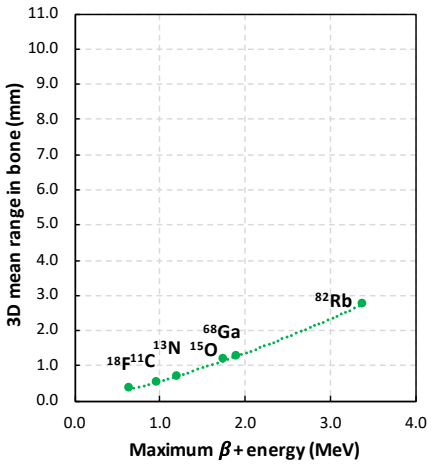

Fig. 4.7: Simulated 3D mean positron range for Bone in a 3T static magnetic field.

netic field does not show any impact of the magnetic field on the absolute values of the positron range in the axial direction. Annihilation point density distribution profiles are presented in Figure 4.8, showing a spread-out density distribution in the z-direction. Figure 4.9 confirms a strong dependency on the density of the tissue surrounding the source.

The effect of the magnetic field is also clearly seen all throughout the different radioisotopes and different tissues, although it is much more prominent for high energy emitters in less dense tissues.

Tab. 4.4: Mean 3D positron range for different tissues and radioisotopes in a 3T-MR field.

	Max Energy (keV)	Branching Ratio (%)	Mean 3D Range (mm)		
			Soft	Lung	Bone
^{18}F	633.5	96.86	0.52	1.70	0.34
^{15}O	1732.0	99.89	1.66	4.28	1.17
^{13}N	1198.5	99.82	1.01	2.63	0.69
^{11}C	960.2	99.75	0.96	1.97	0.51
^{82}Rb	3378.0	95.45	3.82	10.12	2.74
^{68}Ga	1899.0	87.90	2.04	4.59	1.26

Tab. 4.5: Mean positron range of the transversal direction (x or y-direction) for different tissues and radioisotopes with and without 3T-MR field.

Radioisotope	Max Energy (keV)	Mean x or y Range (mm)					
		Soft		Lung		Bone	
		0 T	3 T	0 T	3 T	0 T	3 T
^{18}F	633.5	0.27	0.26	0.95	0.73	0.17	0.17
^{15}O	1732.0	0.93	0.77	3.74	0.97	0.61	0.57
^{13}N	1198.5	0.54	0.49	2.15	0.74	0.35	0.34
^{11}C	960.2	0.48	0.39	1.52	0.63	0.26	0.25
^{82}Rb	3378.0	2.42	1.62	9.10	2.25	1.54	1.28
^{68}Ga	1899.0	1.01	0.95	4.04	1.00	0.66	0.61

Tab. 4.6: Mean positron range of the axial (z-direction) for different tissues and radioisotopes with and without 3T-MR field.

Radioisotope	Max Energy (keV)	Mean z Range (mm)					
		Soft		Lung		Bone	
		0 T	3 T	0 T	3 T	0 T	3 T
^{18}F	633.5	0.27	0.27	0.95	1.08	0.17	0.17
^{15}O	1732.0	0.93	0.93	3.75	0.374	0.61	0.61
^{13}N	1198.5	0.54	0.54	2.15	2.15	0.35	0.35
^{11}C	960.2	0.48	0.51	1.52	1.52	0.26	0.26
^{82}Rb	3378.0	2.42	2.42	8.95	8.96	1.54	1.55
^{68}Ga	1899.0	1.01	1.16	4.05	4.04	0.66	0.66

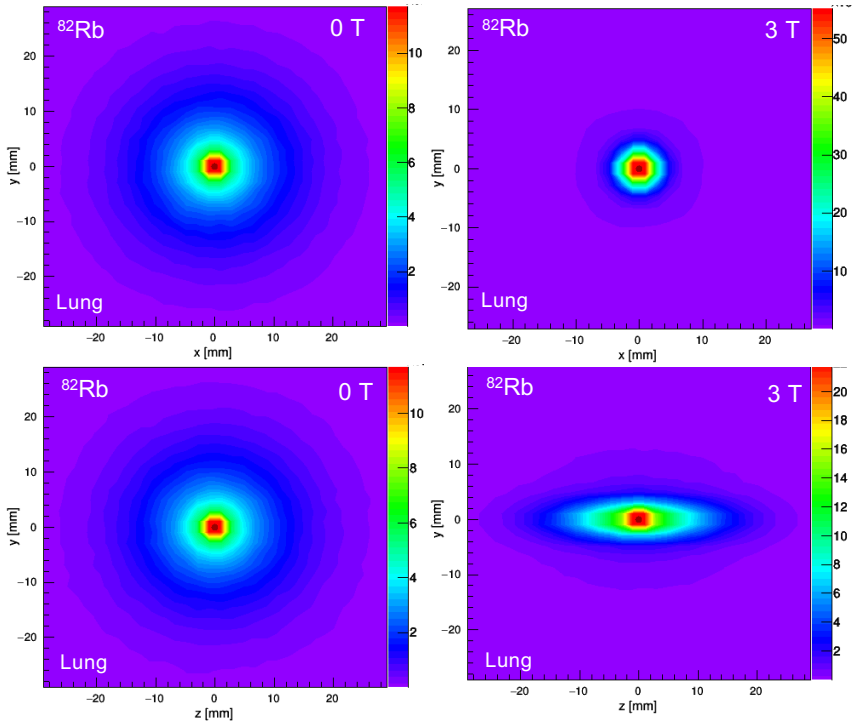

Fig. 4.8: Simulated annihilation endpoint coordinates (y/x and y/z) for an ^{82}Rb point source positioned in the middle of a homogeneous lung tissue at 0T (*left*) and 3T (*right*) static magnetic field in z-direction.

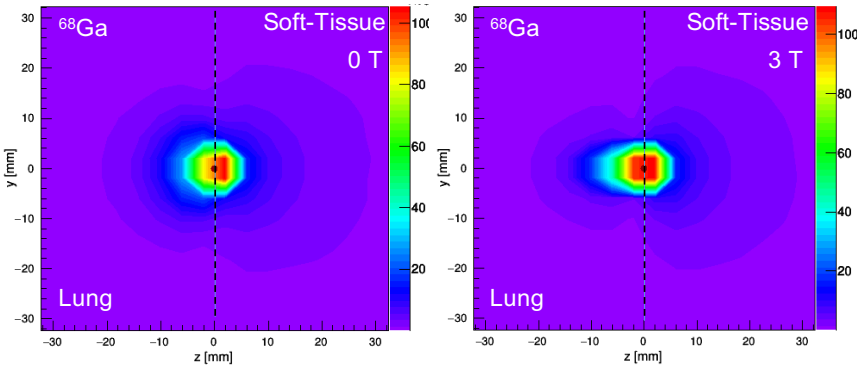

Fig. 4.9: Simulated annihilation endpoint coordinates (y/z) for an ^{68}Ga point source positioned between lung tissue and soft tissue (*dashed black line*) at 0T (*left*) and 3T (*right*) static magnetic field in z-direction.

4.4 Discussion and future work

In this work we have modelled and validated the GE Signa PET/MR to evaluate the performance and characteristics of the system for using different PET isotopes. The GE Signa PET/MR and the NEMA sensitivity and NECR measurements were modeled using GATE for Monte Carlo simulations. GATE-model was validated with published and performed measurements on the same scanner [118]. The effect of the 3T-MR field on positron range was also investigated in different tissue types (lung tissue, soft tissue and bone) for clinically relevant and commercially available isotopes such as ^{18}F, ^{11}C ^{15}O, ^{13}N, ^{82}Rb, ^{68}Ga.

Regarding the GATE Monte Carlo simulations, the NEMA sensitivity tests shown in Table 4.1 and Table 4.2 are in line with the theoretical values expected for all measured and simulated PET radioisotopes (compared to the 21.5 cps/kBq GE Signa PET/MR sensitivity measured value). Sensitivity changes correspond to the scale factor related to the branching ratios of the isotopes. Several design factors including Compton scatter recovery [21, 30, 118], longer axial FOV and reduced ring diameter lead to a higher count rate and an increased sensitivity [43].

For the pure β^+ emitters ^{11}C ^{15}O and ^{13}N the sensitivity was comparable to that of ^{18}F. However, ^{68}Ga and ^{82}Rb show considerable differences. For ^{68}Ga, this was to be expected as the literature values show lower sensitivity of about 2 cps/kBq less than ^{18}F [118], which is also seen in the simulations. The case of ^{82}Rb is quite particular. With a positron branching ratio similar to ^{18}F (<2% difference), the sensitivity is much lower than what was expected. Taking a closer look at the data reveals a difference in the behavior of the radioisotope regarding the annihilation in the sensitivity phantom's attenuation layers. The phantom design needs to be adapted (Figure 4.3). Due to the extremely high energy of 3.381 MeV of the emitted positrons, the measurement with only one attenuation layer might falls outside the trend of the rest of the measurements for this radioisotope, and the other radioisotopes. In addition (for ^{82}Rb in particular), a significant portion of the coincidences being detected outside the scanner bore, which, in theory, should not be possible as no LOR can be placed outside the scanner when two

photons are registered in the detectors. However, due to the additional 777 keV prompt-gamma emission, two gamma photons coming from the same particle can be registered inside the scanner, even when the source is outside of the scanner.

NEMA count rate simulated test summarized Figure 4.4 and Table 4.3, shows agreement with the measured values reported in chapter 3 and previous work using ^{18}F [27]. These results suggest that the GATE-model can be used to study the system performance of the GE Signa PET/MR. For ^{11}C, ^{13}N and ^{15}O (pure positron emitters), the results confirm a peak NECR similar to ^{18}F with the effective activity concentration scaled by the inverse of the positron fraction. These isotopes have short half-lives and high branching ratios for β^+ decay.

For the higher positron energy emitters (^{68}Ga and ^{82}Rb), the simulated count rates test was slightly lower compared to the ^{18}F measured and simulated values, as shown in Chapter 3 and Table 4.3. These is the primarily due to a 1.2% (1.883 MeV) and 13.1% (2.604 MeV) fraction of ^{68}Ga and ^{82}Rb that decays by β^+ and results in prompt gamma contamination into the PET data. These additional prompts lead to additional randoms, scatters and additional detections increasing the deadtime of the detector blocks. However, the recent developments in reconstruction methods (regularized TOF OSEM and PSF), have led to a comparable noise equivalent count rate and a good scatter fraction [118].

In concordance with other positron range studies [52, 106, 107, 118, 123, 124], we confirmed a strong tissue dependency of positron range. In addition, we found borders between different tissue densities to have a noticeable impact on its distribution, with positrons annihilating along the border in the denser tissue, as shown in Figure 4.9 (a point source placed between lung and soft-tissue with and without 3T-MR field in the z-direction). As expected, there is a preeminent 3T magnetic field effect on higher positron energy isotopes. This strongly reduces the positron range by a factor of 3-4 in the transverse plane (x/y) perpendicular to the magnetic field resulting in a significantly increased density distribution in z-direction, as shown in Figure 4.8 and Table 4.4, 4.5 and 4.6. This finding suggests, there may be some effect from the presence of magnetic field. However, this transverse positron range reduction effect will be only partially observed in the resolution properties of the PET/MR

system due to the limiting factor of the 4 mm spatial resolution of the PET detector.

There are limitations to consider in the simulations. The dead time digitizer settings have a certain degree of uncertainty as these values are not published by the manufacturer. The NEMA methods for data analysis of sensitivity via exponential regression can affect the sensitivity when applied to simulated data [125]. This might explain the slightly lower simulated sensitivity values compared to theoretical values. The scatter fraction determined directly from the event counts in the ROOT file slightly underestimates the one estimated using the NEMA method. For all of isotopes simulated the SF were around 38% to 40%, which is slightly lower compared to 43.3% measured for ^{18}F. The 75 second half-life of ^{82}Rb would make NECR experiments with real data difficult. This study has been limited to a 3T magnetic field, reflecting the mean MR field of the GE Signa PET/MR. Additional tests such as image quality may be necessary when to study the PET signal in air tissue boundaries such as lung nodules with high-energy positron emitters.

In summary, the results obtained for the simulated sensitivity and NECR measurement performed on GE Signa PET/MR with a 3T-MR field for different radioisotopes, are comparable to literature values measured following the NEMA protocols, thus validating the simulation model. With this validated GATE-model of the GE Signal Integrated PET/MR it is possible to evaluate different reconstruction algorithms settings using time-of-flight, attenuation or motion correction to estimate their attenuation maps.

4.5 Conclusion and original contribution

GATE Monte-Carlo simulations were used to predict sensitivity and NECR performance of the GE Signa PET/MR according to the NEMA test for ^{18}F, ^{15}O, ^{13}N, ^{11}C, ^{82}Rb and ^{68}Ga radioisotopes. Additionally, we have investigated the positron range effects for different tissue types. Sensitivity and NECR results obtained with the simulated GATE-model matched with published values. The system performance was substantially different for different isotopes. Differences in sensitivity are due

to the scale factor from the positron emission fraction of the radioisotopes. The ^{68}Ga and ^{82}Rb NECR test is affected by larger deadtime and more randoms due to more prompt gammas. The positron range is tissue-dependent and a magnetic field reduces the positron range by a factor of 3-4 in the plane perpendicular to the magnetic field and was found to lead to a measurable increase in the density distribution in z-direction for higher positron energy emitters. Implementing correction using radionuclide specific PSF models in the PET iterative reconstruction algorithms may be useful.

The work described in this chapter gave rise to several conference publications [126, 127, 128, 129] and a manuscript has been submitted for publication in the *Frontiers in Physiology* - Medical Physics and Imaging journal *(currently under review)*.

5

Noise reduction using a BPL reconstruction algorithm on a TOF-PET/CT

In chapter 4 we discussed the performance characteristics of a fully integrated PET/MR system and the impact of using some clinically relevant and commercially available radioisotopes. However the resolution, noise and quantitative accuracy of PET are not only affected by the hardware but also highly influenced by the reconstruction method as discussed in chapter 3. In this chapter, we will discuss the accurate quantitation (*SUV - Standardized Uptake Value*) in PET imaging and the significant challenge with delivering consistently accurate SUV measurements in PET imaging.

5.1 Introduction

Fluorodeoxyglucose (FDG) PET/CT scans provide 3D images of metabolic activity combined with the anatomic structure. This functional imaging modality is widely used for cancer diagnosis in the initial stage and to determine the severity or to assess treatment response [37, 130]. PET/CT technology is constantly being improved and new systems are also combined with emerging improvements in image reconstruction. This leads to changes in the resulting images which need to be tested and clinically validated. The resolution, noise and quantitative accuracy of PET are not only affected by the hardware but also highly influenced by the reconstruction method.

Nowadays the most commonly used PET image reconstruction al-

gorithm in clinical practice is a statistical iterative method known as the Maximum Likelihood Expectation Maximization (MLEM) [131, 132, 133]. This is a slowly converging method, but images are obtained in clinically acceptable times with acceleration through the use of subsets in Ordered Subsets Expectation Maximization (OSEM). However, this accelerated convergence can be problematic since the best result tends to oscillate between different subsets. One of the advantages of statistical reconstruction techniques is the ability to better model the emission and detection process [134]. The effects of attenuation, detector normalization and contamination by scattering and randoms are nowadays corrected in the reconstruction algorithm. These improved models of the interaction in patient and system lead to a more quantitative final image. In the latest systems the modelling of point spread functions (PSF) and Time-of-Flight (TOF) information have also been included and this has shown to lead to a major improvement in image quality [134, 135]. However, OSEM is also suffering from noise increase with increasing number of iterations. In order to reduce image noise, the OSEM algorithm is usually stopped before contrast convergence occurs, in order to prevent excessive image noise amplification. In clinical practice, the algorithm is stopped after 2-4 iterations and 20-30 subsets. Additionally, these images are typically post-smoothed after reconstruction using a low-pass filter to remove noise levels and Gibbs artefacts can occur due to resolution modeling [136, 137, 138].

A new Bayesian Penalized Likelihood Reconstruction algorithm which uses a block sequential regularized expectation maximization as an optimizer, was introduced in the last few years by GE Healthcare. The algorithm, named Q.Clear on their PET scanners, is introduced to improve clinical image quality. The algorithm is expected to reach convergence without increasing noise while preserving edges [139]. Thus, instead of the kernel filter, image characteristics are determined by a regularization β-parameter which penalizes relative differences between neighboring pixels avoiding excessive smoothing over large edges. Also, Gibbs artefacts from resolution modeling are avoided [140]. Several research groups have investigated the improvements of the OSEM and BSREM reconstruction algorithms [30, 141, 142, 143, 144, 145] but not with regards to image quality acquired on the new Discovery MI with 3-

rings (*GE Healthcare*) silicon photomultiplier based TOF-PET/CT with sensitivity of 7.3 cps/kBq and an axial FOV of 15 cm. The lower sensitivity can be compensated for by using more activity or longer acquisition times, however, this is not always possible due to practical, financial or dosimetric constraints.

In this Chapter, the performance and clinical use of BSREM were compared to OSEM with full modelling of PSF and TOF information for both algorithms, acquired on the new Discovery MI with 3-rings (axial FOV of 15 cm). Both phantom and patient data were analyzed with regards to Contrast Recovery (CR), background COV, CNR, SUV ratio, total lesion glycolysis (TLG) and SNR. This study aimed to evaluate different β-factors compared to a clinical post-filter kernel for different data-sets with varying noise levels to investigate whether and to what extent noise can be reduced by using BSREM instead of OSEM.

5.2 Material and Methods

5.2.1 PET/CT System

All data were acquired on a digital GE Discovery MI PET/CT (DMI) system, installed at the Ghent University Hospital, Belgium. The investigated system consists of three detector rings; each PET ring uses 136 detector blocks containing a 4 x 9 array of lutetium-based scintillator (LBS) crystals coupled to a 3 x 6 array of silicon photomultipliers (SiPMs) with Anger multiplexing for crystal identification. Table 5.1 contains a summary of important design and performance parameters [46].

A well counter cross-calibration scan was performed with ^{18}F in a uniform cylindrical phantom before starting the tests as a regular quality control and assurance procedure.

5.2.2 Image reconstruction

The phantom and patient data were reconstructed using a matrix size of 256 x 256 with 2.08 $\times$ 2.08 x 2.78 mm^3 voxels size. Data sets with

Tab. 5.1: Design and performance specifications of the GE Discovery MI commercial system.

GE Discovery MI	3 detector rings
Axial FOV	15 cm
Patient Bore Size	70 cm
Photodetector	SiPM
Scintillator	LBS* (LYSO)
Crystal element size	3.95 x 5.3 x 25 mm^3
Coincidence timing window	4.9 ns
Sensitivity	7.5 cps/kBq
Scatter fraction	41.7%
Peak NECR	102.3 kcps @ 24.7 kBq/ml
Clinical NECR	29.6 kcps @ 2.4 kBq/ml
*Lutetium based scintillator	

multiple acquisition times were generated to evaluate the effect of count statistics on the reconstructed images. BSREM (Q.Clear) reconstruction was done for different penalization β-factors 300, 400, 500, 600, 750, 1000, 1500, and 3000. These reconstructions were compared to the OSEM reconstruction with 3 iterations, 16 subsets and a Gaussian post-filter with a FWHM of 5.0 mm, as recommended by the manufacturer to be used in a clinical setting. All reconstructions included attenuation and scatter correction based on CT as well as PSF modelling and TOF information.

5.2.3 Phantom data

The NEMA (National Electricals Manufacturers Associations) IEC image quality phantom was used for these experiments. To simulate lesions of different sizes, the phantom has 6 fillable spheres of different diameters (10 mm, 13 mm, 17 mm, 22 mm, 28 mm, and 37 mm). The phantom contains a lung insert, which consist of a cylinder positioned in the center of the phantom with an inner diameter of 44.5 mm and a volume of 194 ml. The lung insert was filled with low-density styrofoam pellets and pure water to simulate human lung tissue. The phantom

was prepared according to the NEMA NU 2-2012 protocol (all spheres were filled with ^{18}F) [46]. The background volume of the phantom was filled with an activity concentration of 5.3 kBq/ml (52 MBq of 18F for 9800 ml). The sphere to background ratios were chosen to be 8:1, 6:1, 4:1 and 2:1 for the six spheres.

The phantom data experiments were obtained during a single bed position scan of 20 min. The central slice contained the six spheres and the adjacent slices were also used for the background ROIs. 60 background ROIs of each slice of the reconstructed image of the phantom (12 ROIs on each of five slices) were drawn on the slices as close as possible to ± 1 cm and ± 2 cm on either side of the central slice. The CRs were determined for each hot sphere by Eq. 2.23 described in Chapter 2 Section 2.4. The background Coefficient of Variation (COV) was calculated using Eq. 2.25. Contrast-to-noise ratio was defined as CR divided by the background COV. The SUV values were obtained using a VOI drawn on the OSEM reconstruction of 20 min acquisition and then propagated to the BSREM reconstructions.

The CR data, CNR and background COV of the phantom data were obtained in a single bed-position with full 20 min acquisition. Datasets of 10, 5.0, 2.5, and 1.0 min, representing shorter scans with lower count statistics, were obtained using list-mode selections. Reconstructions of the phantom data were analysed using the NEMA NU 2–2012 protocol and compared based on different reconstruction parameters.

5.2.4 Clinical data

In our institution, an informed patient consent and a positive advice by the ethics committee are necessary for retrospective patient studies. The Belgian registration number (*Belgisch Registratienummer*) for this study is B670201939137. Images were analyzed according to FDG PET-CT European Association of Nuclear Medicine (EANM) procedure guidelines for tumor imaging [146]. The images were analyzed using OsiriX MD 10.0 tools fully optimized for a macOS Mojave 10.14 system installed in the Ghent University Hospital, Belgium. A 71-year-old patient with multiple B-cell lymphoma lesions of different sizes was selected for this study. The patient fasted at least 6 h before receiving an intravenous in-

jection of 340 MBq of ^{18}F-FDG. Before the injection of the radioactivity tracer, a blood sample was taken to ensure the blood glucose levels (97 mg/dl). FDG-PET/CT imaging started 60 min after the intravenous injection of FDG. The total acquisition time (9 time lengths per bed-position), was 10 min (1.07 min/bp). From this dataset, scans of 5.0 min (0.34 min/bp) and 2.5 min (0.17 min/bp) were generated in list-mode. The TOF-PSF-OSEM image with post-smoothing with a 5.0 mm Gaussian filter was chosen to delineate the reference lesion volumes (VOIs). The VOIs were delineated using the a 41% threshold of the maximum voxel value and then propagated to the BSREM reconstructions.

The same reconstruction parameter settings were used as for the phantom data. The noise level was calculated as standard deviation (SD) divided by the SUV_{mean} of a large spherical reference volume ($\ominus$: 3.0 cm) placed in the liver (normal uptake). The lesion SNR was computed as the difference between the SUV_{mean} of the lesion VOI and the background SUV of the reference VOI placed in the liver, divided by the SD of the value in the reference VOI. Contrast was calculated as lesion SUV_{mean} divided by SUV_{mean} of the liver reference VOI. The signal to noise was evaluated for the different lesions by comparing lesion signal to the noise level in the liver (see Table 5.3). The TLG was evaluated as the lesion SUV_{mean} multiplied by the volume of the lesion.

5.3 Results

5.3.1 Phantom data

Contrast Recovery. The results for CR versus background COV of the image quality phantom for each sphere size and for a contrast ratio of 8:1 are shown in Figure 5.1. All plots show a similar trend: the contrast increases when reducing the β-factor and the COV decreases as β increases in value.

Overall, the CR of BSREM reconstructions reach a plateau with only a small gain when changing β from 500 to 300. This is especially the case for the phantom data with low count statistics. There is also a decrease in CR coefficients. Comparing CR of BSREM for different

levels of regularization to the CR of OSEM, reveals higher (or at least similar) contrast recovery for β parameters down to 300, except for the smallest sphere.

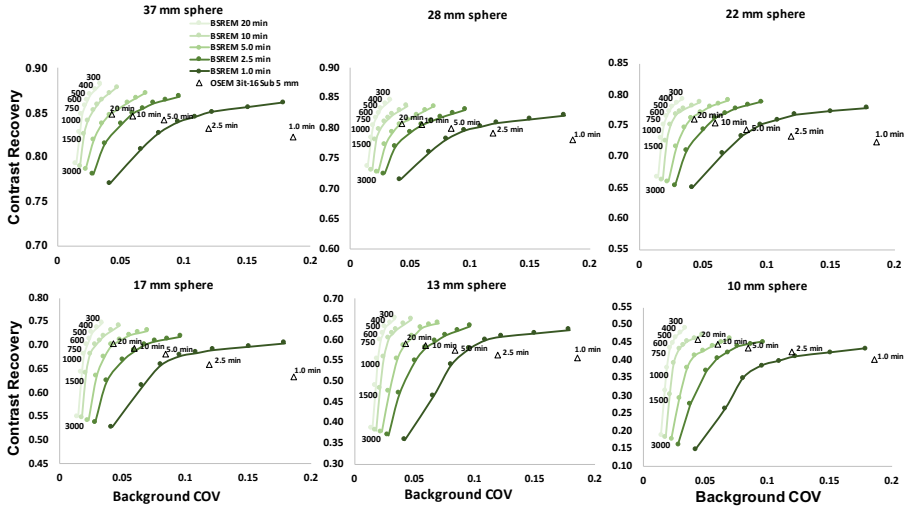

Fig. 5.1: Contrast recovery of BSREM (β =300-3000, including TOF and PSF) and TOF-OSEM (3 iterations, 16 subsets, post-filter 5.0 mm and PSF) as a function of the background coefficient of variation for different acquisition times (20, 10, 5.0, 2.5 and 1.0 min) and a contrast ratio of 8:1. Different plots are shown with decreasing sphere diameter.

For the largest spheres (37, 28, 22 and 17 mm), the CR seems to reach a steady value, where its dependence on the β-parameter decreases. As the sphere size decreases, the convergence of the BSREM reconstructions appears to be dependent of the sphere size. The difference relative to OSEM for each sphere sizes as a function of the β-parameter is shown in Figure 5.2. The CR of OSEM reconstruction under clinical settings at high count statistics (20 min) and contrast ratio of 8:1 match to the CR of BSREM with β =750. Figure 5.3 shows a similar trend (as a function of the acquisition time) for the ratios 6:1 and 4:1.

There is no difference at high count statistics on the CR behavior between the ratios 8:1, 6:1 and 4:1, although the CR of BSREM decreases as the acquisition time reduces. This dependence on the count statistics seems to be more prominent at low count levels (1.0 min) and in the smallest sphere of the 2:1 ratio. The dependence on sphere size, count-

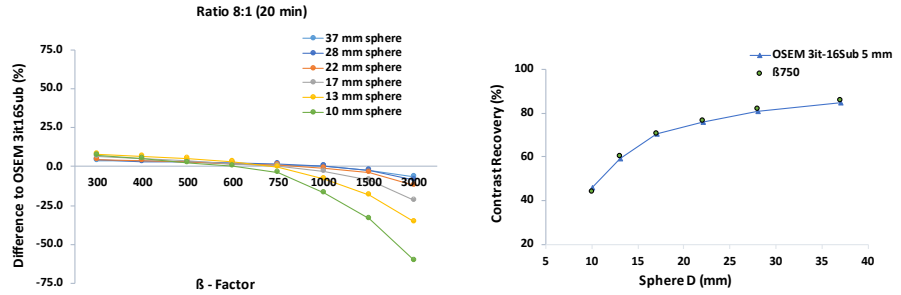

Fig. 5.2: *Left*: Difference relative to the contrast recovery of TOF-OSEM (3 iterations, 16 subsets, post-filter 5.0 mm and PSF) at high count statistics (20 min) for each sphere size as a function of the regularization parameters. *Right*: Comparison of the contrast recovery as a function of the sphere size of BSREM with β =750 (including TOF and PSF) and OSEM for 20 min acquisition. All plots correspond to a contrast ratio of 8:1.

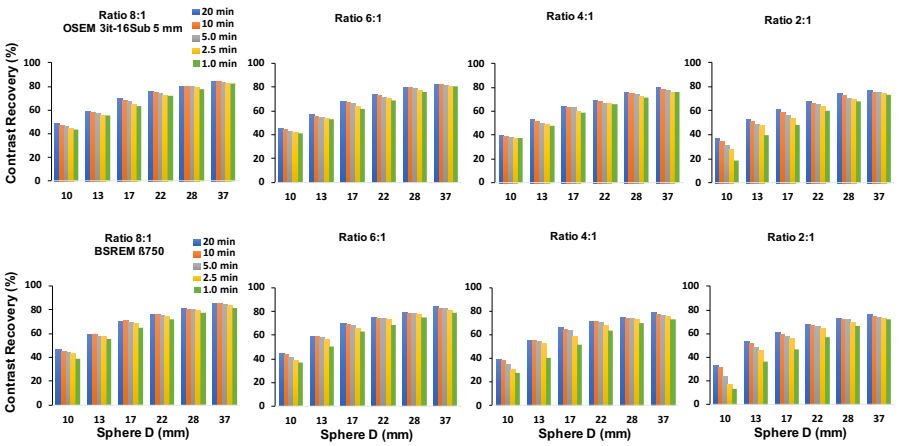

Fig. 5.3: Comparison in terms of contrast recovery as a function of sphere size between (Top) TOF-OSEM (3 iterations, 16 subsets, post-filter 5.0 mm and PSF) and (Bottom) BSREM with β =750(including TOF and PSF) for different counting statistics and contrast ratios.

ing statistics and contrast ratio, is also confirmed by the CNR analysis. Figure 5.4 presents the CNR of BSREM with β =750 and OSEM reconstruction as a function of the sphere sizes for different counting statistics and contrast ratios.

For the ratios 8:1, 6:1 and 4:1, the CNR of β =750 increased by

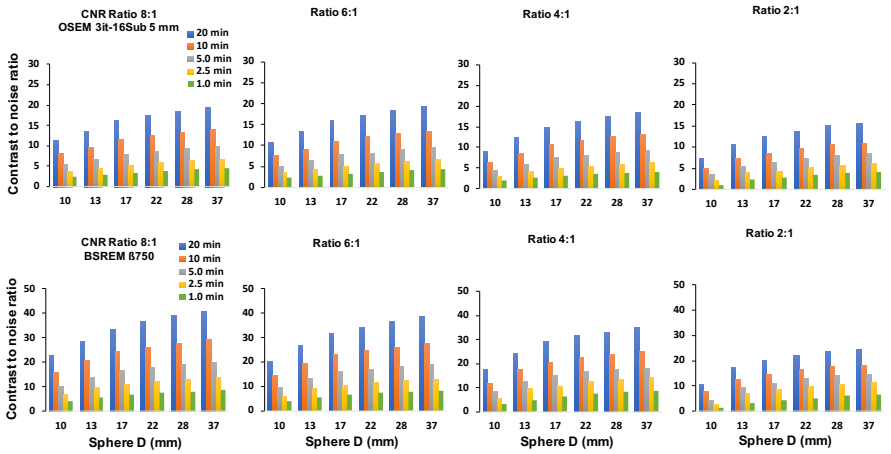

Fig. 5.4: Comparison in terms of CNR as a function of sphere size between (*Top*) TOF-OSEM (3 iterations, 16 subsets, post-filter 5.0 mm and PSF) and (*Bottom*) BSREM with β =750 (including TOF and PSF) for different counting statistics and contrast ratios. Note that the maximum scale value showed in the graphs are different between both reconstructions.

a factor of 2 (for same count level) compared to OSEM reconstruction, although CNR decreases with reduction of counting statistics and sphere size. The same trend was observed for the contrast ratio of 2:1, although there is a clear reduction in the CNR compared to the other ratios.

Tab. 5.2: Comparison in terms of background COV between TOF-OSEM (3 iterations, 16 subsets, post-filter 5.0 mm and PSF) and BSREM with β =750 for a volume of 26.52 ml at different counting statistics. All values correspond to a contrast ratio of 8:1.

Time (min)	Background COV (26.52 ml)	
	OSEM	β750
1.0	0.186	0.095
2.5	0.119	0.059
5.0	0.084	0.041
10	0.059	0.028
20	0.043	0.021

Noise properties. For reduced count statistics of the contrast 8:1 (reducing the acquisition time from 20 to 10, 5.0, 2.5 and 1.0 min),

BSREM has in general a lower COV than OSEM. Moreover, OSEM was more sensitive to noise compared to BSREM with large differences in COV between the different noise levels for OSEM setting. When reducing the number of counts by a factor of 2, the COV can be controlled by increasing the β parameter in the lower count dataset (losing contrast recovery). Similarly, the post-filter can be increased in OSEM. By comparing the reconstruction algorithms for different count levels, the following observations are made: The curves of BSREM at 50 % of counts are always outperforming the curves of OSEM at the full 100 % of counts.

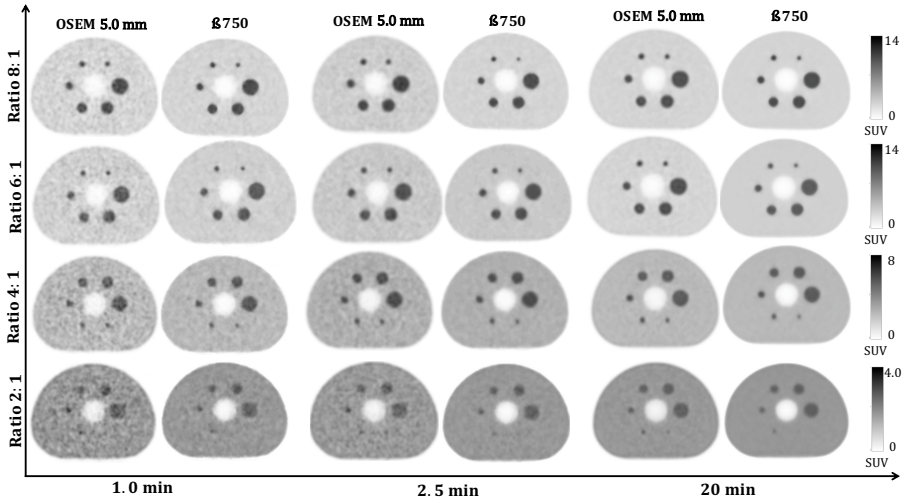

Fig. 5.5: Qualitative evaluation of the transaxial images of the NEMA phantom of TOF-OSEM (3 iterations, 16 subsets, post-filter 5.0 mm and PSF) and BSREM with β =750 (including TOF and PSF). Contrast ratios of 8:1, 6:1, 4:1 and 2:1 are shown in rows and acquisition times (1.0, 2.5 and 20 min) in column. Background level is 5.3 kBq/ml in all cases.

For the 4 largest spheres, the BSREM curves for 25 % of the counts are also outperforming OSEM at 100 % of counts. For any length of the study the highest contrast recovery is observed for the smallest regularization parameter (300). The contrast recovery decreases with increasing β parameter. In comparison with OSEM the contrast is higher for a β between 300 to 600 and comparable for β =750 at 20, 10 and 5.0 min but slightly lower for 2.5 and 1.0 min acquisitions. Furthermore, tak-

ing as a reference the full dataset (20 min) reconstructed with OSEM (post-filter 5.0 mm), it is clear from Figure 5.1 that the contrast (for all sphere sizes) with β =300 to 600 is still higher for 20,10, 5.0 and 2.5 min. For the smallest sphere, the optimal beta is around β =300 and 400. The background COV comparison to OSEM is shown in Table 5.2. The COV of OSEM (20 min) is worse than the COV of BSREM with β =750 for 20, 10 min and 5 min. The COV of OSEM (10 min) is worse than the COV of BSREM with β =750 for 10, 5.0 and 2.5 min. This represents a background COV reduction by a factor of 4. The quantitative noise reduction found in Table 5.2 is also visually confirmed by the reconstructions in Figure 5.5.

For all contrast ratios at 1.0, 2.5 and 20 min, BSREM (with β =750) reconstructions appears to have better background COV compared to OSEM reconstructions. However, β =750 has excessively smoothed the smallest sphere in the 2:1 ratio. This is also confirmed in the Figure 5.1, which suggests using a β value around 300 and 400 for small lesion at high count level. Increasing the β-factor leads to extra contrast loss and should only be done when the count level is low, and contrast can be traded in for reduced background COV.

5.3.2 Clinical data

For the patient data the contrast of the data sets with three different count levels (10, 5.0 and 2.5 total acquisition time) was evaluated for 6 different lesions volume (3.92 ml, 2.46 ml, 1.81 ml, 0.84 ml, 0.54 ml and 0.35 ml) as a function of noise level on the liver. The representa-

Tab. 5.3: Reference values measured in a healthy liver for OSEM and BSREM.

		BSREM					
Measure	OSEM	β300	β500	β750	β1000	β1500	β3000
Volume (cm^3)	14.137						
SUV_{mean}	2.221	2.187	2.192	2.197	2.193	2.204	2.212
SUV_{SD}	0.480	0.441	0.301	0.241	0.206	0.152	0.092

TOF PSF OSEM (3 iterations and 16 subsets and 5mm Gaussian filter).

Measured in a sphere placed in liver for 10 min (total) acquisition time.

tive example of this patient data is presented in Figure 5.6. The curves follow a similar trend as in the phantom reconstructions (Figure 5.1). BSREM outperformed OSEM reconstructions in terms of noise levels with a lower noise level. Also, the largest difference is seen for bigger lesions where reduced noise is combined with higher contrast. The quantitatively measured values of the reference VOIs are shown in Table 5.3.

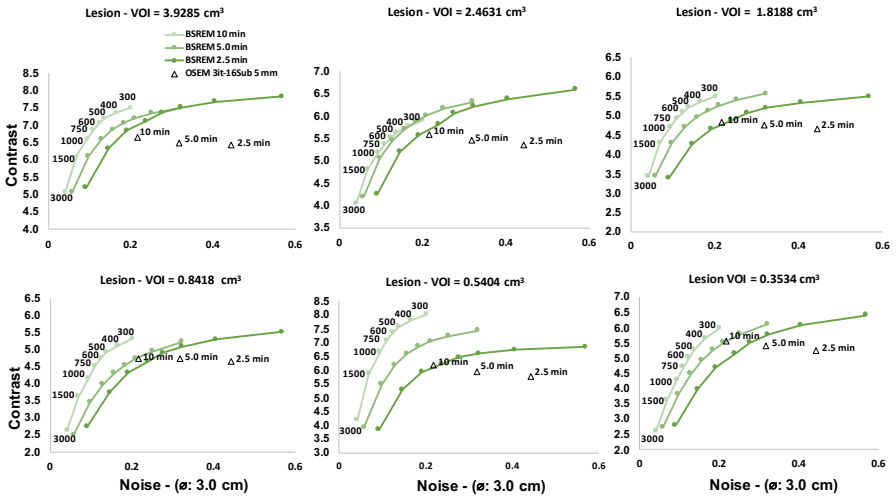

Fig. 5.6: Contrast (SUV ratios) of BSREM (β =300-3000, including TOF and PSF) and TOF-OSEM (3 iterations, 16 subsets, post-filter 5.0 mm and PSF) as a function of noise level of a large VOI ($\ominus$: 3.0 cm) placed in normal liver for different acquisition times (10, 5.0 and 2.5 min). Different plots are shown with decreasing lesion volume.

As shown in Table 5.4, the noise level measured in the liver with BSREM is clearly lower than for OSEM with post-filter. As excepted from the phantom data analysis, the noise in the liver of OSEM reconstruction (10 min) is worse than the noise of BSREM with β =750 for 10 min, 5.0 min and is comparable to 2.5 min. Lower noise can be observed for BSREM in all other cases (also when lowering the counts with a factor 4). This leads to a noise reduction in the liver by a factor of 4. The SNR of BSREM with β =750 and OSEM reconstruction are also shown in Table 5.4 for different count levels.

Similar trend to phantom data presented in the Figure 5.4 is observed

Tab. 5.4: Noise level of a large VOI (⊖: 3.0 cm) placed in the liver and the SNR with all lesion sizes averaged are presenting for TOF-OSEM (3 iterations, 16 subsets, post-filter 5.0 mm and PSF) and BSREM with β =750 (including TOF and PSF). Reference values measured in a healthy liver.

Time (min)*	Noise (14.137 ml)		SNR (Lesion VOI Averaged)	
	OSEM	β750	OSEM	β750
2.5	0.443	0.228	20.256	41.710
5.0	0.318	0.156	15.088	29.092
10	0.217	0.109	10.243	19.448
* Total of 9 range of times per bed-position				

SNR for BSREM with β =750 (averaged for all lesion size) increased by a factor of 2 times for the same counting level. The SNR of both reconstructions decreases with reduction of counting statistics.

Figure 5.7 shows quantitatively the SUV values of the evaluated whole-body ^{18}F-FDG PET images of a patient with multiple lymphoma. In terms of SUV_{mean} and TLG values for all lesion sizes, BSREM (with β =750) reconstructions of 5.0 and 2.5 min are quantitatively similar to the OSEM reconstruction (10 min). Also, a qualitative visual evaluation has the same trends as the phantom reconstructions in Figure 5.5. Based on visual and quantitative differences we found similar trends to the phantom data analysis (Figures 5.1, 5.3 and 5.4). It is possible to reduce the count level of a clinical whole-body ^{18}F-FDG PET/CT imaging with at least a factor of 2.

Another similarity to consider, especially in terms of noise reduction without loss in contrast analyses, is that BSREM reconstruction increased the CNR and SNR by a factor of 2 (for both, phantom and the cinical data) compared to OSEM at same count level.

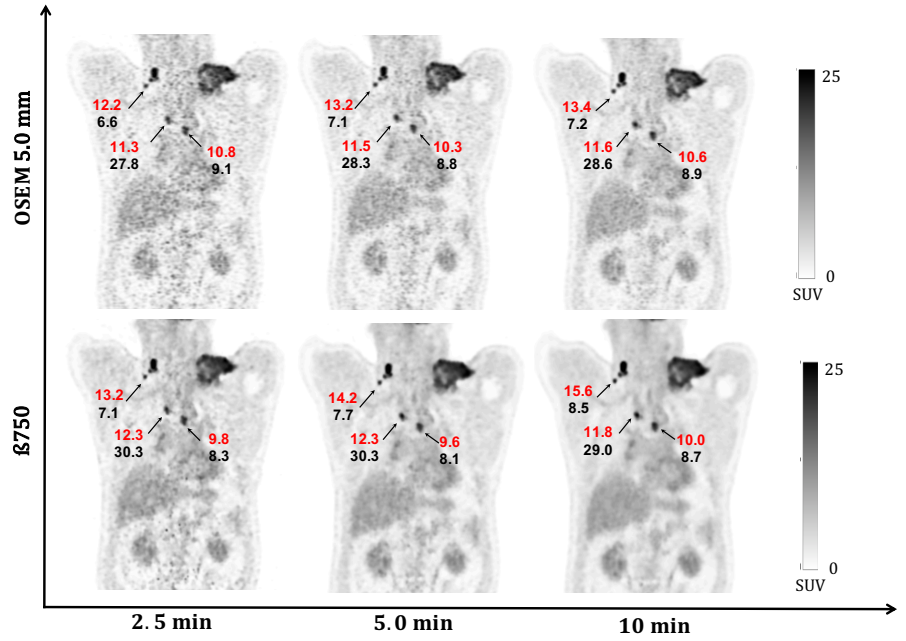

Fig. 5.7: Coronal whole-body ^{18}F-FDG PET images of patient with multiple lesions of different sizes of B-cell lymphoma. The arrows indicate the SUV$_{mean}$ (*red*), and TLG (*black*) of the lesions. Images were reconstructed using BSREM with β =750 (including PSF and TOF) and OSEM PSF TOF (3 iterations and 16 subsets and 5 mm gaussian filter) for 2.5, 5.0 and 10 min.

5.4 Discussion and future work

This study addressed the noise reduction performance of BSREM (Q.clear) compared to OSEM for both phantom and patient data acquired on the new Discovery MI 3-rings silicon photomultiplier based TOF-PET/CT with sensitivity of 7.5 cps/kBq and axial FOV of 15 cm. Differences of the performance between OSEM and BSREM are expected due to the nature of the selective filtering of both algorithms, which can lead to a direct result on different anatomical information [145]. The aim was to investigate if the extent of noise can be reduced without a loss in image quality by using BSREM instead of OSEM.

The latest developments in detector technology and timing resolution of the digital PET/CT result in an increased sensitivity and count

rate statistic compared with conventional PET/CT [147, 148]. These improvements combined with emerging developments in reconstruction methods, lead to changes in the clinical routine which need to be considered and harmonized in order to obtain the most optimal image quality. This should be done in the shortest possible acquisition time, which is preferable in terms of patient care [109, 149]. BSREM reconstructions were compared to OSEM with PSF and TOF information using 3 iterations and 16 subsets and a Gaussian filter with a FWHM of 5 mm, which were the settings recommended by the manufacturer and are expected to be used in a general clinical setting. However, in most of the clinical centers, the reconstruction settings are chosen by the physicians based on the visual assessment of several PET scans. Furthermore, the optimization of BSREM reconstructions has been previously investigated, such as Reynés-Llompart G, *et al.* [145] using a range of β: 50-500 parameters on a BGO PET/CT. Other previous studies [30, 109, 141] have used a range of β: 200-800 to examine the BSREM algorithm. In this work we extended the range to β: 300-3000 to assess, from a clinical point of view which β-parameter has comparable contrast recovery to OSEM on the new GE Discovery MI PET/CT. Afterward, we evaluated qualitatively and quantitatively what is the impact on the noise is under the condition of different contrast ratios and count statistics.

Regarding the contrast recovery and background COV for *equal count levels*, the phantom data analysis showed (Figures 5.1 and 5.2) that for the four largest spheres (17, 22, 28, and 37 mm diameters), BSREM results in increased contrast recovery compared to OSEM. β =750 (Figure 5.2) has comparable resolution to OSEM reconstruction, but with a reduction of 4 times the background COV (Table 5.2). Although β =750 has a comparable CR to OSEM, these results pointed out that the optimal penalization factor depends on the contrast ratio, acquisition time and sphere size. This suggest that a high value of β can lead to a negative impact on the detectability of the small lesions. As presented in Figure 5.1, the phantom results suggest an optimum β-value between 300 and 400, which maximizes the CR and the CNR of the smallest sphere. This is also in agreement with the previous studies [30, 109, 141, 145].

BSREM outperforms OSEM with regards to the COV for all sphere sizes. The investigated clinical data showed a trend similar to the phan-

tom study. For any acquisition time of the phantom data, the highest contrast recovery was found for a β =300 (Figures 5.1 and 5.6), but this value also has the highest background COV of any other BSREM reconstruction. These trends were also confirmed by the clinical data analysis (Figure 5.6 and Table 5.4), where the noise level and contrast are higher for β =300. The use of a lower FWHM value (FWHM < 5 mm) of the smoothing post filter would have maximized the CR and the CNR of OSEM reconstruction, however this would had increased the COV. In comparison with OSEM on the clinical data, BSREM reconstruction (especially for tumor lesions with VOI =3.92 cm3 and VOI =2.46 cm^3) resulted in an increased tumor SUV_{mean}, SUV_{max} and an improved contrast at a matched level of noise. The SNR of the average of all lesion sizes increased by a factor of 2 at the same count level (Figure 5.4). However, for lesions smaller than 1.0 cm^3 (Figures 5.6 and 5.7) both reconstructions were equivalent in terms of SUV values. The same behavior was also found in the phantom data analyses (Figures 5.1 and 5.2). A previous study [150] has reported that while PSF modelling commonly leads to visually enhanced images with higher contrast, it can simultaneously lead to notable edge artifacts affecting the quantification of small lesions. Thus, it is important to assess in which conditions is beneficial and warranted to use PSF modeling. For reduced count levels based on phantom data, BSREM has in general a lower COV than OSEM. When reducing the number of counts by a factor of 2, the COV can be controlled by increasing the β-parameter in the lower count dataset (losing contrast recovery). A similar factor of 2 was observed in the clinical data. BSREM with a β =750 increased SUV values and TLG when compared to OSEM for the same acquisition time (Figure 5.7). However, there was no difference in SUV values between OSEM (10 min) and BSREM (2.5 min), confirming that it is possible to have noise reduction with BSREM while preserving contrast.

Previous studies [109, 149, 150] have suggested β =400 and β =550 as an optimum factor. Another recent study with 45 patients in initial stage of lung cancer has reported a β-values between 450-600 to be ideal for lung cancer [150]. Michael Messerli et. al. [151] highlights the importance for careful standardisation of β-value when following-up non-small cell lung cancer. The optimum factor changes towards

higher β-values in patients who received dose lower than 2 MBq/kg comparing to patients who received doses higher than 2 MBq/kg. The higher β-values appears to be more appropriate for patients with lower ^{18}F-FDG activity. In our study, the most favorable β-factor for both phantom and clinical data was in the same range with β =750 at higher count levels. However, the choice of β might depend on several primary aspects, such as contrast, SNR, counting statistics, radiation dose or lesion detectability. Thus, the β-parameter should be chosen dependent on the requirements and context of the examination. Other aspects to consider are the acquisition duration and the axial FOV size of the TOF PET/CT used. According to EANM's procedure, good clinical whole-body ^{18}F-FDG images are usually obtained with an acquisition time of 3.0 min/bp [146]. The acquisition time reported evaluating the BSREM algorithm used 3 different count statistics varying from 3.0 to 1.0 min/bp reconstruction [109] which has somewhat a discrepancy compared to the range used 1.07, 0.34 and 0.17 min/bp in our study. This peculiar time ranges per bed-position was chosen to evaluate the BSREM under condition of reduced count statistics and, consequently, this decreased range would probably lead to an increase of the β-factor. An axial FOV of 20 cm of the PET/CT scanner, would lead to improvements in sensitivity and count rate statistics compared to an axial FOV of 15 cm used in our study.

There are other limitations that should be considered in this study. All results from the clinical data analysis were taken based on one lymphoma patient with multiple lesions of different sizes. It is possible that an analysis of a larger and diversified group of patients would improve the results concerning the SUV lesion volume dependence. Consequently, it was not possible to evaluate the influence of body mass index of the overweight patients on β-factor [150]. Additionally, there is a restriction concerning the ^{18}F-FDG PET imaging tracer. The use of any other higher positron energy radioisotope would have led to a statistical uncertainty due to the random nature of radioactive emissions [118]. There is a minor risk of using BSREM when the primary requirement is to detect small lesions. Under the condition of higher count statistics, the combination of TOF-PSF-OSEM would lead to a comparable lesion detectability to BSREM, but if OSEM reconstruction is adopted,

caution should also be taken regarding the increase of noise with the increase of the number of iterations. Lowering the counts by a factor of 2-4 (*e.g.* from 10 min to 2.5 min), BSREM would therefore lead to a comparable contrast recovery, CNR, background COV and SUV values than TOF-PSF-OSEM reconstructions at higher count statistics. On the other hand, this reduction, allows clinicians to reduce the PET activity needed for many exams, benefiting especially young patients. In general, BSREM outperforms OSEM reconstructions allowing noise reduction without losing data information.

5.5 Conclusion and original contribution

Penalized-Likelihood BSREM reconstruction improves image quality and allows noise reduction by a factor 2-4 while preserving contrast compared to OSEM reconstructions. Lowering of the injected dose or shortening the acquisition time is therefore possible by introducing regularization in the image reconstruction without a loss in image quality.

This work described in this chapter yields to several conference [117, 152, 153, 154, 155] publications and a *Springer Nature* - EJNMMI Physics publication [156].

5.6 Ethics approval and consent to participate

An informed patient consent and a positive advice by the ethics committee are necessary for retrospective studies in our institution. The Belgian registration number for this study is B670201939137.

5.7 Consent for Publication

The patient gave their written consent to our Healthcare Institute for use data including anonymized pictures.

6 Conclusion and future perspectives

In this chapter, we give a general overview of all chapters and the most important results obtained during this work. For some remaining issues, suggestions for future research will be presented. We will conclude this chapter with a conclusion.

6.1 Summary

This thesis covers the evaluation of image quality and reconstruction parameters in state-of-the-art PET/CT and PET/MR systems. In the first stage, we evaluated the NEMA performance and characteristics of the TOF-PET/MR for ^{18}F, ^{68}Ga and ^{90}Y radioisotopes. Secondly, we used the measured data to develop and validate a realistic GATE Monte Carlo model of the integrated GE Signa PET/MR. This model was used to predict the NEMA performance for PET radioisotopes (^{18}F, ^{11}C, ^{15}O, ^{13}N, ^{82}Rb and ^{68}Ga) and to evaluate the effect of a 3T MR field on positron range. Thirdly, we evaluated the image quality of the new generation of SiPM based TOF-PET/CT system. A noise reduction study was performed to evaluate the impact of varying noise levels on the image quality and to investigate whether and to what extent the impact of noise can be reduced by using BSREM instead of OSEM. For that purpose, we compared the image quality measurements for ^{18}F using different contrast ratios.

In Chapter 2, we gave an overview of different imaging techniques

that were relevant for this work. In the *first part*, we described the concept of anatomical and molecular-functional imaging to help the reader understand the context of this thesis. Before describing positron emission tomography, an overview of radionuclide and radiopharmaceutical application was presented. This was followed by an introduction to PET. Next, we presented the basics of the PET detector technology covering coincidence detection and TOF-PET. Subsequently, effects that degrade the PET image quality and quantitative accuracies, such as the effects related to positron emission physics, limitations of the detector technology and subject dependent effects were discussed. Finally, we summarized the image representation of the patient's body containing the tracer distribution on the PET imaging (discussed in the subsection 2.1.5).

In the *second part*, the state-of-the-art PET image reconstruction algorithms were introduced. Because of noise propagation in iterative reconstruction algorithm such as OSEM, we discussed an efficient and alternative way for noise suppression by introducing a regularization term with a regularization parameter which controls the relative strength of the regularizing term and therefore the noise behaviour. This section was followed by an overview of how PET imaging evolved into hybrid imaging in combination with CT (PET/CT) and MRI (PET/MRI). To objectively compare PET/CT and PET/MR system performance, NEMA performance measurement (spatial resolution, sensitivity, NECR, image quality and accuracy) for PET scanners were described. Finally, because this thesis uses extensively GATE Monte Carlo simulations, we discussed in the last part of this chapter Monte Carlo simulation methods in nuclear medicine.

In Chapter 3, we discussed the important aspects of the performance of a fully integrated PET/MR system and the impact of using different radioisotopes. PET/MR imaging is frequently used in clinical research and routine. NEMA characterization of these systems is generally done with ^{18}F which is clinically the most relevant PET isotope. However, other PET isotopes, such as ^{68}Ga and ^{90}Y, are gaining clinical importance as they are of specific interest for oncological applications. These isotopes have a complex decay scheme with a variety of prompt gammas in coincidence. ^{68}Ga and ^{90}Y have higher positron energy and, because

of the larger positron range, there is significant interference with the magnetic field of the MR compared to ^{18}F. Therefore, it was relevant to determine the performance of PET/MR for these clinically relevant and commercially available isotopes.

The results of the system performance tests were presented and discussed in the final part of chapter 3. The system performance of the integrated GE Signa PET/MR was substantially different, in terms of NEMA *spatial resolution* for ^{68}Ga PET imaging test as compared to ^{18}F and ^{90}Y. We reported that in the transverse plane the magnetic field reduces the effective positron range, the dominant factor on spatial resolution seems to be the detector pixel size and the transverse resolution is therefore comparable with the result of ^{18}F. The FWHM difference relative to ^{18}F measured values were 17.8% and -1.3% at 1 cm and 27.9% and 3.5% at 10 cm off-centre in the axial direction for ^{68}Ga and ^{90}Y respectively. Subsequently, we found the NEMA spatial resolution test is not well designed to account the effect of magnetic field on positron range on the transaxial resolution measurements. To account the positron range effects, NEMA spatial resolution test needs to be adapted. For that, we also measured a new approach measuring the point source distribution with a molecular sieve instead of using capillary glasses. Figure 3.1, shows the limitation of the NEMA SR test. The spatial resolution has increased for ^{68}Ga using the molecular approach.

The biggest change for *image quality* with ^{68}Ga are the increased positron range as compared to ^{18}F. We showed that the inferior resolution also affects the contrast recovery of the radioactive spheres in the NEMA quality phantom for ^{68}Ga. However, the contrast recovery increased when compared using TOF, PSF and post-smooth filter, as showed in Figures 3.4B and 3.5B. Subsequent we evaluated the lung residual error (Table 3.5). The results were comparable between ^{18}F and ^{68}Ga, but for ^{90}Y the background variability and the lung, error is higher than for ^{18}F and ^{68}Ga, which is also visually seen (15h and 30 min acquisition) in Figure 3.6.

Regarding the *Sensitivity* test, the primary factor for the *sensitivity* change is the scale factor related to the positron emission fraction (96.7%, 87.9%, 0.003186% for ^{18}F, ^{68}Ga, and ^{90}Y respectively). The low branching ratio of ^{90}Y explains the substantial quality difference of the

reconstructed transverse image quality phantom as compared with ^{18}F and ^{68}Ga images (Figure 3.6).

In the last part of Chapter 3, we gave a general discussion of the results obtained from NEMA count rate performance measurements. Two major conclusions were drawn. First, the scatter fraction at NECR peak (Table 3.4 and Figure 3.3) for ^{68}Ga was slightly lower compared to ^{18}F. This is primarily due to 1.2% (1.883 MeV) fraction of ^{68}Ga that decays by β^+ can result in a small prompt gamma (1.077 MeV) [97, 98] contamination into the PET data. The prompt gammas of ^{68}Ga can directly fall into the energy window and accepted by the PET scanner. This happens when the 1.077 MeV photon scatters in the phantom and generates energy in the energy window. Second, the ^{68}Ga NECR test was lower than for ^{18}F and the peak appears at a slightly higher activity concentration (Figure 3.2). The lower peak for the NECR can be explained by the additional 1.077 MeV gamma-ray which leads to additional detections and increases the deadtime of the detector blocks. These can also lead to additional randoms or scatter when they lose enough energy and fall into the energy window. However, the effect of these prompt-gammas is very small compared to the scatter fraction (Table 3.4). The maximum absolute value of the slice error is 2.9% and 6.0% for ^{18}F and ^{68}Ga, respectively.

Further validation of a realistic GATE Monte Carlo model of the PET/MR using the NEMA measurements was presented in Chapter 4. Three major findings were presented and discussed. In the first part of the chapter, we gave an overview of the physical properties of the ^{18}F, ^{11}C, ^{15}O, ^{13}N, ^{82}Rb, ^{68}Ga radioisotopes and the GATE Monte Carlo simulation setup. Monte Carlo simulations were implemented in GATE using the high-performance computer *Vlaams Supercomputer Centrum* installed at Ghent University. Subsequently, we implemented a realistic GATE model of the GE Signa integrated PET/MR. The geometry was modelled using a cylindrical PET system in GATE, considering foam, plastic and copper shielding between the field of view and the detectors. In the subsection 4.3.1, we presented the GATE-model of the GE Signa PET/MR NEMA scatter and sensitivity phantoms with the uniform activity distribution in a 70-cm-line source (Figure 4.2) as described by the corresponding NEMA protocol.

In the second part of this chapter, we gave a general discussion of the results obtained from the simulated phantom data. The GATE-model was validated with NEMA measurement of the sensitivity and noise equivalent count rate for ^{18}F and ^{68}Ga as described in Chapter 3 [118]. NEMA sensitivity tests shown in the Tables 4.1 and 4.2 were in line with the theoretical values for all measured and simulated PET radioisotopes (compared to 21.5 cps/kBq sensitivity measured value). For ^{11}C ^{15}O and ^{13}N the sensitivity result was comparable to that of ^{18}F. For ^{68}Ga, a lower measured and simulated sensitivity of about 2 cps/kBq less than ^{18}F [118] was observed as expected and described in literature values show. With a positron branching ratio similar to ^{18}F (<2% difference), the sensitivity obtained for ^{82}Rb was much lower than what was expected. The NEMA sensitivity phantom design needs to be adapted to accurately measure the sensitivity for ^{82}Rb. Due to the extremely high energy of 3.381 MeV of the emitted positrons, the measurement with only one attenuation layer shows that it falls outside the trend of the rest of the measurements for this radioisotope compared to the other radioisotopes. Equally important, because of the additional 776.5 keV prompt-gamma emission, a significant portion of the coincidences coming from the same particle can be registered inside the scanner, even when the source is outside of the scanner. In terms of NEMA count rate statistics, simulation results for ^{18}F and ^{68}Ga showed good agreement with published and measured values of Chapter 3. The comparison between simulated and measured values for PET/MR are summarized in Table 4.3. Figure 4.4 shows the true, random and scattered coincidence rates as a function of the activity concentration. The curves of the test are presented for ^{18}F, ^{15}O, ^{13}N, ^{82}Rb, ^{68}Ga. Comparing the NECR of ^{68}Ga and ^{82}Rb emitting higher energy positrons with ^{18}F measurements and simulations, the simulated count rate curves were slightly lower. Because of the simultaneous emission of prompt gammas (3.2% with 1.077 MeV and 15.1% with 0.777 MeV for ^{68}Ga and ^{82}Rb, respectively) additional random and scatter events are detected which increase the dead time of the detector blocks.

Finally, we used the GATE-model to predict the performance of the system for ^{18}F, ^{11}C, ^{15}O, ^{13}N, ^{82}Rb, ^{68}Ga and to evaluate the effect of the 3T-MR field on positron range in different tissue types (lung

tissue, soft tissue and bone). We confirmed a strong tissue dependency of positron range as shown in Figure 4.9. The effect of the magnetic field is also clearly seen throughout the different radioisotopes and different tissues, although it is much more prominent for high energy emitters is less dense tissues. As expected, there is also an effect of the 3T magnetic field on isotopes with a higher positron energy isotopes range. This effect strongly reduces the positron range by a factor of 3-4 in the transverse plane (x/y) perpendicular to the magnetic field resulting in a significantly increased density distribution in z-direction. While significant changes are seen in the transversal plane, the magnetic field does not have an impact on the positron range in the axial direction, which is the same direction as the MR field. Because of the limited spatial resolution of 4 mm of the PET detector, this transverse positron range reduction effect will be only partially observed in the resolution properties of the PET/MR system.

In Chapter 5, we discussed the accurate quantitation (*SUV - Standardized Uptake Value*) in PET imaging and the significant challenge with delivering consistently accurate SUV measurements in PET imaging. *Q.Clear* is a block sequential regularized expectation maximization (BSREM) penalized-likelihood reconstruction algorithm for PET. It tries to improve image quality by controlling noise amplification during image reconstruction. In this chapter, the noise properties of this BSREM were compared to the ordered-subset expectation maximization (OSEM) algorithm for both phantom and patient data acquired on a state-of-the-art PET/CT. All data were acquired on a digital GE Discovery MI PET/CT (DMI) system, installed in Ghent University Hospital, Belgium. To access this issue, the performance and clinical use of BSREM was compared to OSEM with full modelling of PSF and TOF information for both algorithms acquired on the Discovery MI with 3-rings (axial FOV of 15 cm). Both phantom and patient data were analyzed with regards to CR, background COV, CNR, SUV ratio, metabolic active tumour volumes (MATVs) and SNR. This study aimed to evaluate different β-factors compared to a clinical post-filter kernel for different datasets with varying noise levels to investigate whether and to what extent noise can be reduced by using BSREM instead of OSEM.

In the first part, the method is described in detail. The NEMA IQ

phantom and a whole-body patient study were acquired on a GE DMI 3-rings system in list mode and different datasets with varying noise levels were generated. Phantom data was evaluated using four different contrast ratios (8:1, 6:1, 4:1 and 2:1). These were reconstructed using BSREM with different β-factors of 300, 400, 500, 600, 750, 1000, 1500 and 3000 and with a clinical setting (3 iterations, 16 subsets with 5.0 mm FWHM) used for OSEM including point spread function (PSF) and time-of-flight (TOF) information. Contrast recovery (CR), background noise levels (coefficient of variation, COV), and contrast-to-noise ratio (CNR) were used to determine the performance in the phantom data. Findings based on the phantom data were compared with clinical data. For the patient study, the SUV ratio, metabolic active tumour volumes (MATVs), and the signal-to-noise ratio (SNR) were evaluated using the liver as the background region.

The results of the phantom data were presented in subsection 5.3.1 and discussed in the final part of this chapter. Two major parts were discussed. The first part is regarding the *Contrast Recovery*. Based on the phantom data for the same count statistics, BSREM resulted in higher CR and CNR and lower COV than OSEM. In all plots, we observed a similar trend: the contrast increases when reducing the β-factor and the COV decreases as β increases in value. We found the CR of BSREM with $\beta = 750$ that matches to the CR of OSEM at high count statistics for 8:1. A similar trend was observed for the ratios 6:1 and 4:1.

A dependence on sphere size, counting statistics, and contrast ratio were confirmed by the CNR of the ratio 2:1. For the largest spheres (37, 28, 22 and 17 mm), the CR seems to reach a steady value, where its dependence on the β-parameter decreases. As the sphere size decreases, the convergence of the BSREM reconstructions appears to be dependent on the sphere size. The difference relative to OSEM for each sphere sizes as a function of the β-parameter is shown in Figure 5.2. Additionally, for the phantom data with low count statistics, we also observed that the CR of BSREM reconstructions reaches a plateau with only a small gain when changing β from 500 to 300. Comparing CR of BSREM for different levels of regularization to the CR of OSEM, reveals higher (or at least similar) contrast recovery for β parameters down to 300, except

for the smallest sphere.

The second part is regarding the *Noise properties*. For reduced count statistics of the contrast 8:1 (reducing the acquisition time from 20 to 10, 5.0, 2.5 and 1.0 min), BSREM has in general lower COV than OSEM. Moreover, OSEM was more sensitive to noise compared to BSREM with large differences in COV between the different noise levels for OSEM setting. BSREM with $\beta = 750$ for 2.5 and 1.0 min acquisition has comparable COV to the 10 and 5.0 min acquisitions using OSEM. The background COV comparison to OSEM is shown in Table 5.2. The COV of OSEM (20 min) is worse than the COV of BSREM with β =750 for 20, 10 min and 5 min. The COV of OSEM (10 min) is worse than the COV of BSREM with β =750 for 10, 5.0 and 2.5 min. This resulted in a noise reduction by a factor of 2–4 when using BSREM instead of OSEM.

For the patient data, a 71-year-old patient with multiple *B*-cell lymphoma lesions of different sizes was selected for this study. The patient fasted at least 6 h before receiving an intravenous application of 340 MBq of ^{18}F-FDG. The total acquisition time (9-time lengths per bed-position) was 10 min (1.07 min/bp). From this dataset, scans of 5.0 min (0.34 min/bp) and 2.5 min (0.17 min/bp) were generated in list-mode. The TOF-PSF-OSEM image with post-smoothing with a 5.0 mm filter was chosen as reference lesion volumes (VOIs). Finally, the VOIs were delineated using the 41% threshold of the maximum voxel value and then propagated to the BSREM reconstructions.

The results were presented in the last part of this chapter. We observed a similar trend to the phantom data. SNR was reduced by at least a factor of 2 while preserving contrast. In agreement with phantom data analysis, BSREM outperformed OSEM reconstructions in terms of noise levels with a lower noise level. Also, the largest difference is seen for bigger lesions where reduced noise is combined with higher contrast. The quantitatively measured values of the reference VOIs are shown in Table 5.3. Regarding the *noise properties*, the noise in the liver of OSEM reconstruction (10 min) is worse than the noise of BSREM with β =750 for 10 min, 5.0 min and is comparable to 2.5 min. Lower noise can be observed for BSREM in all other cases (also when lowering the counts with a factor 4). This leads to a noise reduction in the liver by a fac-

tor of 4. The SNR of BSREM with β =750 and OSEM reconstruction are also shown in Table 5.4 for different count levels. However, under the condition of higher count statistics, the combination of TOF-PSF-OSEM would lead to a comparable lesion detectability to BSREM, but if OSEM reconstruction is adopted, caution should also be taken regarding the increase of noise with the increase of the number of iterations.

In general, BSREM outperforms OSEM reconstructions allowing noise reduction by a factor of 2-4 without losing data information. This would allow clinicians to reduce the PET activity/acquisition time needed for many exams, benefiting especially young patients.

6.2 Future perspectives

This is the first published NEMA PET performance measurement and characteristic for different clinically relevant and commercially available isotopes. NEMA procedures are intended for characterizing a PET imaging system. However, NEMA test has some major limitations. The spatial resolution results presented in Chapter3 were affected by the mean MR field. An alternative approach to measuring the SR using molecular sieve instead of capillary glasses was proposed for ^{68}Ga SR measurements (see Figure 3.1). This approach has shown an improvement of 9.1% and 19.2% at 1 cm and 10 cm off centre for ^{68}Ga measurements. It confirms that the NEMA SR test needs to be adapted. As we pointed out, the branching ratio can be used to predict theoretical sensitivities for the different isotopes. But the NECR predictions are more difficult than the sensitivity test. NECR is highly dependent on block deadtime with prompt gammas affecting the deadtime, even if their energy does not fall within the energy window. Therefore, the high-energy gamma from ^{82}Rb and ^{68}Ga will affect the NECR. A way to quantify the quality of the system timing resolution is to perform the TOF test method, first introduced by Wang et al. [157] and later on included in the latest version of the NEMA NU 2-2018 protocol [46]. This method uses the list-mode data acquired during the standard NEMA NECR measurements for timing resolution characterization. Although NEMA NU 2-2018 protocol only recommend to use ^{18}F for this measurement, it would

be of great scientific interest to measure the TOF resolution for ^{82}Rb, ^{68}Ga and ^{90}Y and plotting timing resolution (in ps) versus the activity concentration (in kBq/ml). Since there are no count rate performance data reported in this book for ^{90}Y, it would be interesting to perform the NECR test for ^{90}Y. The line source could remain in the scatter phantom for several weeks, and every day, be repositioned for a frame of acquisition. However, it is recommended to use specific activities and acquisition times similar to that of clinical whole-body ^{18}F-FDG, instead to counterbalance by increasing acquisition times [158]. Additional NEMA tests such as image quality may be necessary when resolving PET signal in air tissue boundary such as lung nodules with high-energy positron emitters. Certainly, we do not recommend that all sites measure all radionuclides they use with the NEMA NU 2 approach. If sites want some intuition how that would extend to other radionuclides, then they would reference publications in this book. Furthermore, a secondary conclusion of this thesis is drawn regarding the effect of the magnetic field on the measurements/simulations and this study has been limited to a 3T magnetic field of the GE Signa PET/MR. In terms of literature data, a direct comparison of resolution measurements between PET/CT and PET/MR is available but only for ^{18}F. Although it is not a straightforward comparison because PET/CT systems have larger PET ring diameters, it would be interesting to compare both systems in terms of RC and contrast rations for the different radioisotope. That is why the results presented in this book are useful. With the GATE-model of the GE Signal Integrated PET/MR, it is possible to simulate the NEMA performance without 3T and with different magnetic field strengths and to evaluate the performance of different reconstruction algorithms using time-of-flight.

The noise reduction results presented in Chapter 5, should be explored for other applications. In PET centres with different PET systems or a multicenter setting, the resolution of different PET systems is generally harmonized for clinical use and optimal exchange of patient data. We found a beta value that matches the resolution of an OSEM reconstruction using 3 iterations, 16 subsets, and a 5 mm FWHM Gaussian postfilter. As such, we could compare in detail the noise characteristics of OSEM and BSREM reconstructions while both reconstruction

approaches were matched in terms of resolution. Findings showed that BSREM reconstruction algorithm allowed a noise reduction without a loss of contrast by a factor of 2-4 compared to OSEM reconstructions for all data evaluated. This reduction can be used to lower the injected dose or shorten the acquisition time. However, the patient data used for this study is very limited. Even though we choose for this study a patient with multiple *B*-cell lymphoma lesions of different sizes (in line with the sphere sizes of the image quality phantom) the analysis of a larger and diverse group of number patients, would be interesting to reconfirm findings. Conducting observational research in different clinical centres using patient with small lesions (< 0.5 ml) for a diagnostic test is another way to reconfirm (the dependence on sphere size) with our phantom study. Besides the noise reduction using a more advanced reconstruction approach, it would be very interesting to study the use of deep learning network training to improve noise characteristics. This would be especially valuable for the development and validation of new image reconstruction methods based on deep learning.

6.3 Conclusion

In this thesis, we have evaluated the system performance and image quality of state-of-the-art PET/CT and PET/MR systems for different PET isotopes. The system performance of GE Signa integrated PET/MR was substantially different, in terms of NEMA spatial resolution, image quality, and NECR for ^{68}Ga and ^{90}Y compared to ^{18}F. On the other hand, the larger positron range of PET radioisotopes emitting higher energy positrons was affected by the presence of a 3T MR field in case of PET/MR. Subsequently, we used GATE Monte-Carlo simulations to predict sensitivity and NECR performance of GE Signa PET/MR for ^{18}F, ^{11}C, ^{15}O, ^{13}N, ^{82}Rb and ^{68}Ga radioisotopes. Differences in sensitivity are in line with the different branching ratios for positron emissions of the different PET isotopes. ^{82}Rb and ^{68}Ga NECR values are affected by deadtime effects because of more random and scatter events due to prompt gamma emissions. Finally, the Penalized-Likelihood BSREM reconstruction improves image quality compared to standard OSEM re-

constructions and allows noise reduction by a factor 2-4 while preserving contrast. Therefore, lowering of the injected dose or shortening the acquisition time is possible without a loss in image quality by introducing regularization in the image reconstruction. Therefore, the results of this thesis will allow clinicians to reduce the PET dose which is especially relevant for young patients. Besides, MC simulation platform for PET/MR developed for this thesis will allow physicists and engineers to better understand and design integrated PET/MR systems.

A

Decay schemes of radioisotopes for PET

In this appendix, we provide formal decay schemes of different radioisotopes.

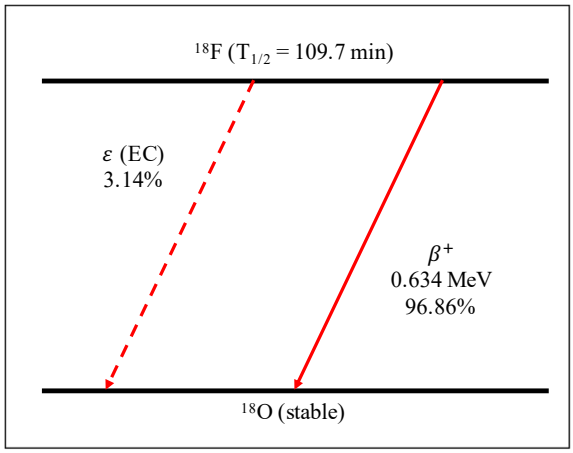

^{18}F 110min	%	max(mean) E (MeV)	range (mm)
β+	96.9	0.634(0.250)	2.4(0.6)
EC	3.1	--	--

Fig. A.1: Fluorine-18(^{18}F)

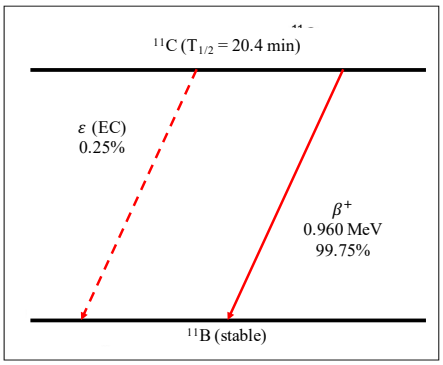

^{11}C 20.4min	%	max(mean) E (MeV)	range (mm)
β+	99.8	0.960(0.386)	4.2(1.2)
EC	0.2	--	--

Fig. A.2: Carbon-11 (^{11}C)

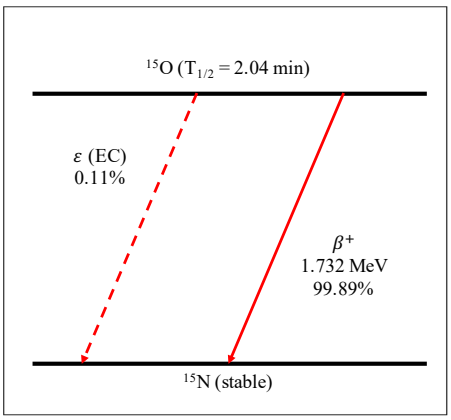

^{15}O 2.0min	%	max(mean) E (MeV)	range (mm)
β+	99.9	1.732(0.735)	8.4(3.0)
EC	0.1	--	--

Fig. A.3: Oxygen-15 (^{15}O)

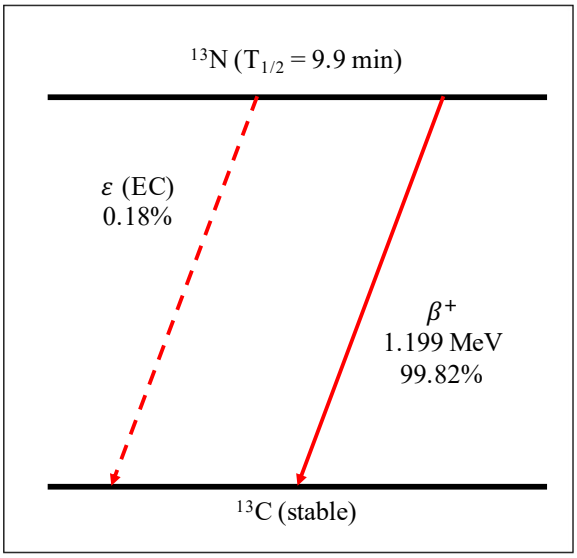

^{13}N 10.0min	%	max(mean) E (MeV)	range (mm)
β+	99.8	1.199(0.492)	5.5(1.8)
EC	0.2	--	--

Fig. A.4: Nitrogen-13 (^{13}N)

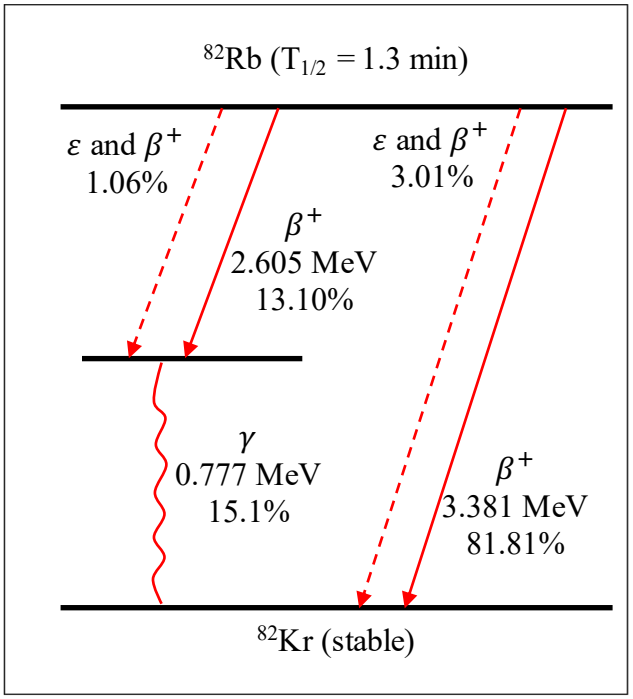

^{82}Rb 1.3min	%	max(mean) E (MeV)	range (mm)
β_1+	81.8	3.378(1.535)	17.0(7.1)
β_2+	13.1	2.601(1.168)	13.0(5.0)
β_3+	0.3	1.206(0.527)	5.5(1.9)
β_4+	0.1	1.903(0.843)	9.0 (3.5)
EC	4.6	--	--
γ_1	15.1	0.777	--

Fig. A.5: Rubidium-82 (^{82}Rb)

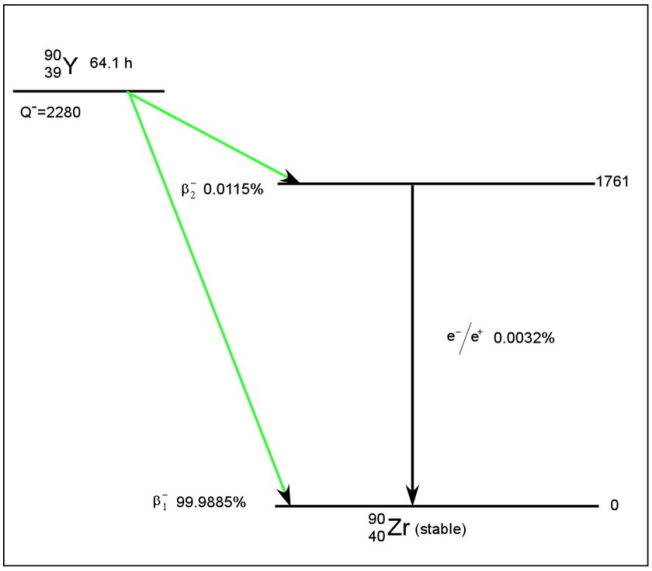

^{90}Y 64.1h	%	max(mean) E (MeV)	range (mm)
β_1^-	99.9885	2.280(0.934)	11.0(4.0)
β_2^-	0.0115	0.519(0.185)	1.9(0.4)
with β_2^-:			
e^-/e^+	0.0032	<0.739	--
with β_1^-: Bremsstrahlung			
X-rays		0-2.280	--

Fig. A.6: Yttrium-90 (^{90}Y)

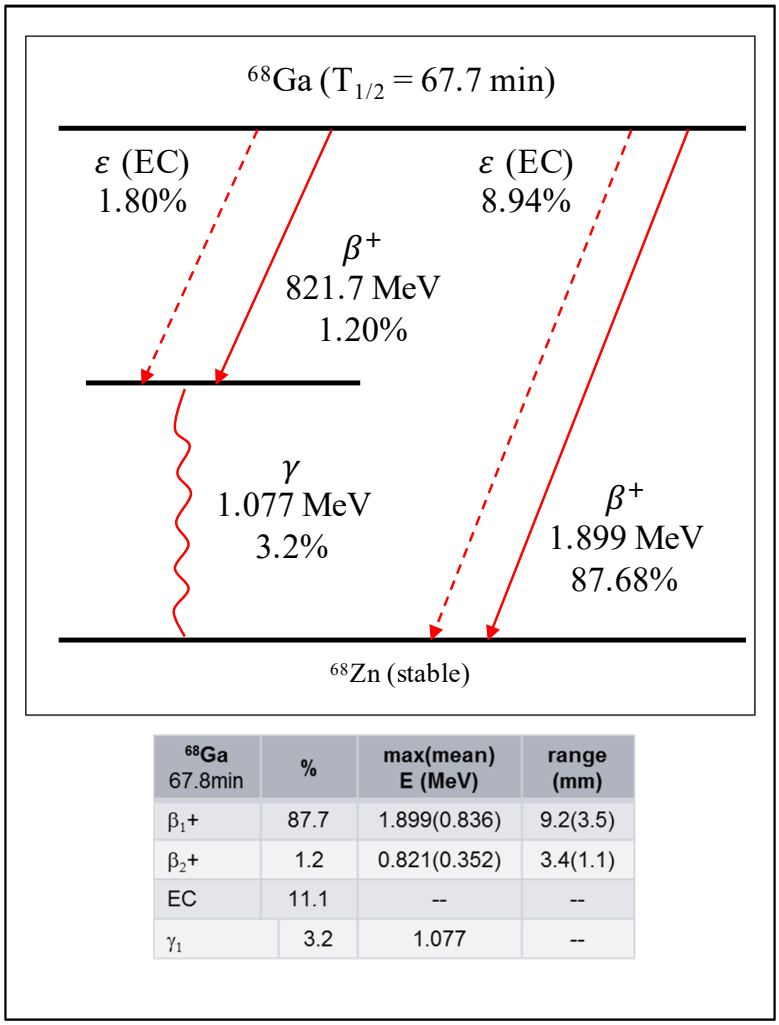

^{68}Ga 67.8min	%	max(mean) E (MeV)	range (mm)
β_1+	87.7	1.899(0.836)	9.2(3.5)
β_2+	1.2	0.821(0.352)	3.4(1.1)
EC	11.1	--	--
γ_1	3.2	1.077	--

Fig. A.7: Gallium-68 (^{68}Ga)

B
Clinical evaluation

Complete evaluation of reconstruction algorithm performance requires task-based assessment of image quality under broad imaging conditions. Quantitative figures of merit for lesion SNR, contrast, and noise were used as described here.

Lesion SNR

For each lesion, the SNR was computed as the difference between the mean lesion and liver SUV_{mean}, compared to the liver noise.

$$SNR = \frac{SUV_{Lesion,mean} - SUV_{Liver,mean}}{SUV_{Liver,\sigma}} \tag{B.1}$$

where $SUV_{liver,mean}$ and $SUV_{Liver,\sigma}$ are the mean and standard deviation, respectively, of a 5 cm^3 VOI placed in a healthy liver zone. The VOIs were delineated using the a 41% threshold of the maximum voxel value.

Contrast

The contrast was defined as:

$$Contrast = \frac{SUV_{Lesion,mean}}{SUV_{Liver,mean}} \tag{B.2}$$

TLG

The total lesion glycolysis was defined as:

$$TLG = SUV_{Lesion,mean} \times VOI_{Lesion} \tag{B.3}$$

Noise

The noise was defined as:

$$Noise = \frac{SUV_{Liver,\sigma}}{SUV_{Liver,mean}} \tag{B.4}$$

Bibliography

[1] Specialty Portable X-Ray. X-ray and ultrasound imaging company specializing in in-home care. `http://xrayathome.com`, 2018. Accessed: 2019-11-11.

[2] Paul Suetens. *Fundamentals of Medical Imaging*, volume 6. Cambridge University Press, Cambridge CB2 8RU, UK, 2009.

[3] Thorsten M. Buzug. *Computed Tomography*. Springer Berlin Heidelberg, Berlin, Heidelberg, 2007.

[4] Simon R. Cherry, James A. Sorenson, and Michael E. Phelps. *Physics in Nuclear Medicine*. Elsevier Sumders, Saunders: Philadelphia, 2012.

[5] Gopal B. Saha, PhD. *Basics of PET Imaging: Physics, Chemistry, and Regulations*. Springer International Publishing, Switzerland, 2016.

[6] Maurizio Conti and Lars Eriksson. Physics of pure and non-pure positron emitters for PET: A review and a discussion. *EJNMMI Physics*, 3(1):8, Dec 2016.

[7] T.G. Walker and M. Saffman. Zeros of Rydberg-Rydberg Foster interactions. *Journal of Physics B (Atomic, Molecular and Optical Physics)*, 38(2):309–19, jan 2005.

[8] HEADQUARTERS. National institute of standards and technology. http://www.nist.gov/, 2019. Accessed: 2019-06-19.

[9] EDP Sciences. Laboratoire national henri becquerel:library for gamma and alpha emissions. http://laraweb.free.fr/, 2019. Accessed: 2019-06-18.

[10] Alejandro Sonzogni and NNDC. National nuclear data center, brookhaven national laboratory. www.nndc.bnl.gov/nndc/nudat, 2019. Accessed: 2019-06-19.

[11] Craig S Levin and Edward J Hoffman. Calculation of positron range and its effect on the fundamental limit of positron emission tomography system spatial resolution. *Phys. Med. Biol. 44 781.*, 44(3):781–799, 1999.

[12] Perkins JM Pagnanelli RA Borges-Neto S Reiman RE. Howard BA, James OG. A practical method of i-131 thyroid cancer therapy dose optimization using estimated effective renal clearance. *SAGE Open Med Case Rep.*, 5:1–4, Dec 2017.

[13] Khan AH. Maqsood MH, Tameez Ud Din A. Neuroendocrine tumor therapy with lutetium-177: A literature review. *Cureus*, 1:11, Jan 2019.

[14] Riaz A. Salem R. Memon K., Lewandowski R.J. Yttrium 90 microspheres for the treatment of hepatocellular carcinoma. *Multidisciplinary Treatment of Hepatocellular Carcinoma: Recent Results in Cancer Research*, 190, Jan 2013.

[15] Renaud Lhommel, Larry Van Elmbt, Pierre Goffette, Marc Van Den Eynde, François Jamar, Stanislas Pauwels, and Stephan Walrand. Feasibility of 90Y TOF PET-based dosimetry in liver metastasis therapy using SIR-Spheres. *European Journal of Nuclear Medicine and Molecular Imaging*, 37(9):1654–1662, 2010.

[16] Thomas Carlier, Kathy P. Willowson, Eugene Fourkal, Dale L. Bailey, Mohan Doss, and Maurizio Conti. 90Y -PET imaging: Exploring limitations and accuracy under conditions of low counts and high random fraction. *Medical Physics*, 42(7):4295–4309, 2015.

[17] CNEN. Comissão nacional de energia nuclear. `http://www.cnen.gov.br`, 2019. Accessed: 2019-08-12.

[18] ANVISA. Brazilian health regulatory agency. `http://portal.anvisa.gov.br/english`, 2019. Accessed: 2019-08-12.

[19] Association of Imaging Producers and Equipment Suppliers. Diagnosis tracers and radiotherapeutics: What for? `www.aipes-eeig.org`, 2019. Accessed: 2019-08-19.

[20] R. Laforest and X. Liu. Image quality with non-standard nuclides in PET. *Quarterly Journal of Nuclear Medicine and Molecular Imaging*, 52(2):151–158, 2008.

[21] Ashwin A. Wagadarikar, Adrian Ivan, Sergei Dolinsky, and David L. McDaniel. Sensitivity improvement of time-of-flight (ToF) PET detector through recovery of compton scattered annihilation photons. *IEEE Transactions on Nuclear Science*, 61(1):121–125, 2014.

[22] Cristina Lois, Bjoern W. Jakoby, Misty J. Long, Karl F. Hubner, David W. Barker, Michael E. Casey, Maurizio Conti, Vladimir Y. Panin, Dan J. Kadrmas, and David W. Townsend. An assessment of the impact of incorporating time-of-flight information into clinical PET/CT imaging. *Journal of Nuclear Medicine*, 51(2):237–245, 2010.

[23] Craig S. Levin, Sri Harsha Maramraju, Mohammad Mehdi Khalighi, Timothy W. Deller, Gaspar Delso, and Floris Jansen. Design Features and Mutual Compatibility Studies of the Time-of-Flight PET Capable GE SIGNA PET/MR System. *IEEE Transactions on Medical Imaging*, 35(8):1907–1914, 2016.

[24] UEMS/EBNM EANM. *European Nuclear Medicine Guide*. HGP Vullers, 2017-2018.

[25] L. G. Strauss and P. S. Conti. The applications of PET in clinical oncology. *Journal of Nuclear Medicine*, 32(4):623–648, 1991.

[26] R. Pani, M.N. Cinti, R. Scafè, R. Pellegrini, F. Vittorini, P. Bennati, S. Ridolfi, S. Lo Meo, M. Mattioli, G. Baldazzi, F. Pisacane, F. Navarria, G. Moschini, P. Boccaccio, V. Orsolini Cencelli, and D. Sacco. Energy resolution measurements of labr3:ce scintillating crystals with an ultra-high quantum efficiency photomultiplier tube. *Nuclear Instruments and Methods in Physics Research Section A: Accelerators, Spectrometers, Detectors and Associated Equipment*, 610(1):41 – 44, 2009. New Developments In Photodetection NDIP08.

[27] Alexander M. Grant, Timothy W. Deller, Mohammad Mehdi Khalighi, Sri Harsha Maramraju, Gaspar Delso, and Craig S. Levin. NEMA NU 2-2012 performance studies for the SiPM-based ToF-PET component of the GE SIGNA PET/MR system. *Medical Physics*, 43(5):2334–2343, 2016.

[28] Stefaan Vandenberghe and Paul K. Marsden. PET-MRI: A review of challenges and solutions in the development of integrated multimodality imaging. *Physics in Medicine and Biology*, 60(4):R115–R154, 2015.

[29] E.A. Kravchenko, V.V. Porosev, and G.A. Savinov. Measurement of the time resolution of small SiPM-based scintillation counters. *Journal of Instrumentation*, 12(12):P12020–P12020, dec 2017.

[30] David F.C. Hsu, Ezgi Ilan, William T. Peterson, Jorge Uribe, Mark Lubberink, and Craig S. Levin. Studies of a next-generation silicon-photomultiplier-based time-of-flight PET/CT system. *Journal of Nuclear Medicine*, 58(9):1511–1518, 2017.

[31] Cherry SR. Berg E. Innovations in instrumentation for positron emission tomography. *Semin Nucl Med*, 48(4):311–331, 2018.

[32] Marnix C Maas. *Monolithic Scintillator Detectors for High-Resolution Positron Emission Tomography*. Mekelweg 15, 2629 JB Delft, The Netherlands, nov 2008.

[33] Roel Van Holen Mariele Stockhoff and Stefaan Vandenberghe. Optical simulation study on the spatial resolution of a thick

monolithic pet detector. *Physics in Medicine and Biology*, 64(195003):13, 2019.

[34] Tabacchini V Borghi G and Schaart DR. Towards monolithic scintillator based tof-pet systems: practical methods for detector calibration and operation. *Phys. Med. Biol.*, 61(13):4904, 2016.

[35] Conde P et. al. Determination of the interaction position of gamma photons in monolithic scintillators using neural network fitting. *IEEE Trans. Nucl. Sci.*, 63:30, 2016.

[36] Keereman V Vandenberghe S España S, Marcinkowski R and Van Holen R. Digipet: sub-millimeter spatial resolution small-animal pet imaging using thin monolithic scintillators. *Phys. Med. Biol.*, 59(13):3405, 2014.

[37] Stefaan Vandenberghe, Ekaterina Mikhaylova, Ester D'Hoe, Pieter Mollet, and Joel S. Karp. Recent developments in time-of-flight pet. *EJNMMI PHYSICS*, 3(1):30, 2016.

[38] Siemens Healthcare. Introducing biograph vision. `https://siemens.com/vision`, 2018. Accessed: 2019-09-11.

[39] Joyce Van Sluis, Johan De Jong, Jenny Schaar, Walter Noordzij, Paul Van Snick, Rudi Dierckx, Ronald Borra, Antoon Willemsen, and Ronald Boellaard. Performance characteristics of the digital biograph vision PET/CT system. *Journal of Nuclear Medicine*, 60(7):1031–1036, 2019.

[40] Lewellen TK. Recent developments in pet detector technology. *Physics in Medicine and biology*, 53(17):R287, 2008.

[41] Derenzo SE. Moses WW. Prospects for time-of-flight pet using lso scintillator. *Nuclear Sci IEEE Trans.*, 43(3):474–478, 1999.

[42] Trott CM Scheuermann J-Karp JS. El Fakhri G, Surti S. Improvement in lesion detection with whole-body oncologic time-of-flight pet. *J Nucl Med.*, 52(3):347–353, 2011.

[43] Andrei Iagaru, Erik Mittra, Ryogo Minamimoto, Mehran Jamali, Craig Levin, Andrew Quon, Garry Gold, Robert Herfkens, Shreyas Vasanawala, Sanjiv Sam Gambhir, and Greg Zaharchuk. Simultaneous Whole-Body Time-of-Flight 18F-FDG PET/MRI. *Clin Nucl Med*, 40(1):1–8, 2019.

[44] Gaspar Delso, Sebastian Fürst, Björn Jakoby, Ralf Ladebeck, Carl Ganter, Stephan G. Nekolla, Markus Schwaiger, and Sibylle I. Ziegler. Performance measurements of the siemens mMR integrated whole-body PET/MR scanner. *Journal of Nuclear Medicine*, 52(12):1914–1922, 2011.

[45] GE Healthcare. SIGNA PET/MR NEMA NU 2-2007 Manual. pages 1–58, 2007.

[46] National Electrical Manufacturers Association. Nema nu-2-2018 performance measurement of positron emission tomographs. `https://www.nema.org`, 2019. Accessed: 2019-09-01.

[47] Pieter Mollet. *Transmission-based attenuation correction for time-of-flight positron emission tomography*. PhD thesis, Ghent University, 2014.

[48] Bert Vandeghinste, Jan De Beenhouwer, Roel Van Holen, Stefaan Vandenberghe, and Steven Staelens. Characterizing the parallax error in multi-pinhole micro-spect reconstruction. In *IEEE Nuclear Science Symposium Conference Record*, pages 2738–2742. IEEE, 2011.

[49] A. et. al. Rahmin. Analitic system matrix resolution modeling in pet: an application to rb-82 cardiac imaging. *Phys. Med. Biol.*, 53:5947–5965, 2008.

[50] Martin S. Judenhofer and Simon R. Cherry. Applications for preclinical PET/MRI. *Seminars in Nuclear Medicine*, 43(1):19–29, 2013.

[51] Ottavia Bertolli, Afroditi Eleftheriou, Matteo Cecchetti, Niccolò Camarlinghi, Nicola Belcari, and Charalampos Tsoumpas. PET

iterative reconstruction incorporating an efficient positron range correction method. *Physica Medica*, 32(2):323–330, 2016.

[52] Shih Ying Huang, Dragana Savic, Jaewon Yang, Uttam Shrestha, and Youngho Seo. The effect of magnetic field on positron range and spatial resolution in an integrated whole-body time-of-flight PET/MRI system. *2014 IEEE Nuclear Science Symposium and Medical Imaging Conference, NSS/MIC 2014*, 94143:3–6, 2016.

[53] S. E. Derenzo. Mathematical removal of positron range blurring in high resolution tomography. *IEEE Transactions on Nuclear Science*, 33(1):565–569, Feb 1986.

[54] H. Pérez-H.Castro H. Olaya Dávila, S. A. Martínez Ovalle. Determination of spatial resolution of positron emission tomograph of clear pet-xpad3/ct system. *Universal Journal of Physics and Application*, 4(11):97–101, 2017.

[55] John M Ollinger. Model-based scatter correction for fully 3d PET. *Physics in Medicine and Biology*, 41(1):153–176, jan 1996.

[56] Alden N Bice. Monte carlo PET simulations: effect of photon polarization on scatter estimates. *Physics in Medicine and Biology*, 37(5):1185–1188, may 1992.

[57] I Torres-Espallardo, M Rafecas, V Spanoudaki, D P McElroy, and S I Ziegler. Effect of inter-crystal scatter on estimation methods for random coincidences and subsequent correction. *Physics in Medicine and Biology*, 53(9):2391–2411, apr 2008.

[58] R D Badawi, M P Miller, D L Bailey, and P K Marsden. Randoms variance reduction in 3d PET. *Physics in Medicine and Biology*, 44(4):941–954, jan 1999.

[59] A. K. Shukla and Utham Kumar. Positron emission tomography: An overview. *J Med Phys*, 31(1):13–21, jan-Mar 2006.

[60] Frederic H. Fahey. Data acquisition in pet imaging. *Journal of Nuclear Medicine Technology*, 30:39–49, may 2002.

[61] Samuel Matej, Joel S Karp, Robert M Lewitt, and Amir J Becher. Performance of the fourier rebinning algorithm for PET with large acceptance angles. *Physics in Medicine and Biology*, 43(4):787–795, apr 1998.

[62] J G Colsher. Fully-three-dimensional positron emission tomography. *Physics in Medicine and Biology*, 25(1):103–115, jan 1980.

[63] Adam Kesner. 3d image reconstruction explained with gifs. `http://bit.ly/1cXb5vq`, 2014. Accessed: 2019-09-21.

[64] Daniël M. Pelt and Kees Joost Batenburg. Improving filtered backprojection reconstruction by data-dependent filtering. *IEEE Transactions on Image Processing*, 23(11):4750–4762, Jully 2014.

[65] Judit Lantos, Erik S Mittra, Craig S Levin, and Andrei Iagaru. Standard OSEM vs. regularized PET image reconstruction: qualitative and quantitative comparison using phantom data and various clinical radiopharmaceuticals. *American journal of nuclear medicine and molecular imaging*, 8(2):110–118, 2018.

[66] Ronald Boellaard, Nanda C. Krak, Otto S. Hoekstra, and Adriaan A. Lammertsma. Effects of noise, image resolution, and ROI definition on the accuracy of standard uptake values: A simulation study. *Journal of Nuclear Medicine*, 45(9):1519–1527, 2004.

[67] Sangtae Ahn and Jeffrey A. Fessler. Globally convergent image reconstruction for emission tomography using relaxed ordered subsets algorithms. *IEEE Transactions on Medical Imaging*, 22(5):613–626, 2003.

[68] Natalya Denisova. Bayesian maximum-a-posteriori approach with global and local regularization to image reconstruction problem in medical emission tomography. *Entropy*, 21:08, nov 2019.

[69] Shan Tong, Adam M Alessio, and Paul E Kinahan. Image reconstruction for PET/CT scanners: past achievements and future challenges. *Imaging in Medicine*, 2(5):529–545, oct 2010.

[70] L. Guralnik D. Gaitini-A. Frenkel A. Kuten H. Altman Z. Keidar R. Bar-Shalom, N. Yefremov and O. Israel. Clinical performance of pet/ct in evaluation of cancer: additional value for diagnostic imaging and patient management. *Journal of nuclear medicine*, 44(8):1200–1209, 2003.

[71] Picchio M. Scattoni V. et al. Giovacchini, G. Psa doubling time for prediction of [11c]choline pet/ct findings in prostate cancer patients with biochemical failure after radical prostatectomy. *Eur J Nucl Med Mol Imaging*, 37:1106–1116, 2010.

[72] Julia G. Mannheim, Andreas M. Schmid, Johannes Schwenck, Prateek Katiyar, Kristina Herfert, Bernd J. Pichler, and Jonathan A. Disselhorst. Pet/mri hybrid systems. *Seminars in Nuclear Medicine*, 48(4):332 – 347, Jully 2018.

[73] Jakob Wehner Bjorn Weissler Pierre Gebhardt Benjamin Goldschmidt Andre Salomon Peter Duppenbecker Fabian Kiessling Patrick Hallen, David Schug and Volkmar Schultz. Evaluation of pet performance and mr compatibility of a preclinical pet/mr insert with digital silicon photomultiplier technology. *EJNMMI Physics*, 2(1):A55, 2015.

[74] G.B. Ko, K.Y. Kim, H.S. Yoon, M.S. Lee, J.-W. Son, H.-J. Im, and J.S. Lee. Evaluation of a silicon photomultiplier pet insert for simultaneous pet and mr imaging. *Medical Physics*, 43(1):72–83, 2016. cited By 22.

[75] C. Catana, Y. Wu, M.S. Judenhofer, J. Qi, B.J. Pichler, and S.R. Cherry. Simultaneous acquisition of multislice pet and mr images: Initial results with a mr-compatible pet scanner. *Journal of Nuclear Medicine*, 47(12):1968–1976, 2006. cited By 306.

[76] R. Leahy and X. Yan. Incorporation of anatomical mr data for improved functional imaging with pet. *Lecture Notes in Computer Science (including subseries Lecture Notes in Artificial Intelligence and Lecture Notes in Bioinformatics)*, 511 LNCS:105–120, 1991. cited By 107.

[77] C. Keller. Adrenalectomy - hormone replacement in adrenal insufficiency [adrenalektomie - hormonsubstitution bei nebenniereninsuffizienz]. *Journal fur Urologie und Urogynakologie*, 22(1):14–15, 2015.

[78] Ronald Boellaard, Ivo Rausch, Thomas Beyer, Gaspar Delso, Maqsood Yaqub, Harald H. Quick, and Bernhard Sattler. Quality control for quantitative multicenter whole-body PET/MR studies: A NEMA image quality phantom study with three current PET/MR systems. *Medical physics*, 42(10):5961–5969, 2015.

[79] D E Raeside. Monte carlo principles and applications. *Physics in Medicine and Biology*, 21(2):181–197, mar 1976.

[80] Michael A. King Michael Ljungberg, Sven-Erik Strand(Editor). *Monte Carlo Calculations in Nuclear Medicine, Second Edition: Applications in Diagnostic Imaging (Series in Medical Physics and Biomedical Engineering)*. Taylor and Francis-CRC Press, 2013.

[81] Eric Vandervoort, Marie-Laure Camborde, Sébastien Jan, and Vesna Sossi. Monte carlo modelling of singles-mode transmission data for small animal PET scanners. *Physics in Medicine and Biology*, 52(11):3169–3184, may 2007.

[82] Karuta B. and Lecomte R. Effect of detector weighting functions on the point spread function of high-resolution pet tomographs: a simulation study. *IEEE Trans. Med. Imaging*, 11(3):379, 1992.

[83] Jan S et al. Gate: a simulation toolkit for pet and spect. *Phys. Med. Biol.*, 49(19):4543, 2004.

[84] Jan S et al. Monte carlo simulation of the micropet focus system for small rodents imaging applications. *IEEE Nuclear Science Symp. and Medical Imaging Conf. Rec.*, 3:1653, 2005.

[85] Knoess C et al. Performance evaluation of the micropet r4 pet scanner for rodents. *Eur. J. Nucl. Med. Mol. Imaging*, 30(5):737, 2003.

[86] Rowland D Siegel S Newport D Chow P Tai Y, Ruangma A and Laforest R. Performance evaluation of the micropet focus: a third-generation micropet scanner dedicated to animal imaging. *J. Nucl. Med.*, 46(3):455, 2005.

[87] Livieratos L Adam LE Bailey DL Wegmann K, Zaers J and Brix G. Investigation of the scatter contribution in single photon transmission measurements by means of monte carlo simulations. *IEEE Trans. Nucl. Sci.*, 46(4):1184, 1999.

[88] S. Agostinelli at. el. Geant4—a simulation toolkit. *Nuclear Instruments and Methods in Physics Research Section A: Accelerators, Spectrometers, Detectors and Associated Equipment*, 506(3):250 – 303, 2003.

[89] Hatazawa J. Yamamoto S Watabe H Kanai Y Aoki M Sugiyama E Watabe T Imaizumi M Shimosegawa E. Fpga-based rf interference between pet and mri sub-systems in a silicon-photomultiplier-based pet/mri system. *Phys Med Biol.*, 56:4147–4159, 2011.

[90] Gaspar Delso and Sibylle Ziegler. PET/MRI system design. *European Journal of Nuclear Medicine and Molecular Imaging*, 36(SUPPL. 1):86–92, 2009.

[91] Bing Bai, Quanzheng Li, and Richard M. Leahy. Magnetic resonance-guided positron emission tomography image reconstruction. *Seminars in Nuclear Medicine*, 43(1):30–44, 2013.

[92] Maurizio Conti and Lars Eriksson. Physics of pure and non-pure positron emitters for PET: a review and a discussion. *EJNMMI Physics*, 3(1):8, Dec 2016.

[93] Sangeeta Ray Banerjee and Martin G. Pomper. Clinical applications of Gallium-68. *Applied Radiation and Isotopes*, 76:2–13, 2013.

[94] Ali Afshar-Oromieh, Christian M. Zechmann, Anna Malcher, Matthias Eder, Michael Eisenhut, Heinz G. Linhart, Tim Holland-Letz, Boris A. Hadaschik, Frederik L. Giesel, Jürgen Debus, and

Uwe Haberkorn. Comparison of PET imaging with a 68Ga-labelled PSMA ligand and 18F-choline-based PET/CT for the diagnosis of recurrent prostate cancer. *European Journal of Nuclear Medicine and Molecular Imaging*, 41(1):11–20, 2014.

[95] Martin T. Freitag, Jan P. Radtke, Boris A. Hadaschik, A. Kopp-Schneider, Matthias Eder, Klaus Kopka, Uwe Haberkorn, Matthias Roethke, Heinz Peter Schlemmer, and Ali Afshar-Oromieh. Comparison of hybrid 68Ga-PSMA PET/MRI and 68Ga-PSMA PET/CT in the evaluation of lymph node and bone metastases of prostate cancer. *European Journal of Nuclear Medicine and Molecular Imaging*, 43(1):70–83, 2016.

[96] Zweifel R Cservenyak T Westera G Goerres GW et al. Schmin DT, John H. Fluorocholine pet/ct in patients with prostate cancer: initial experience. *Radiology*, 235:623–628, 2005.

[97] A. Andreyev and A. Celler. Dual-isotope PET using positron-gamma emitters. *Physics in Medicine and Biology*, 56(14):4539–4556, 2011.

[98] Irina Velikyan. Prospective of 68Ga-Radiopharmaceutical development. *Theranostics*, 4(1):47–80, 2014.

[99] Usha Pandey, Archana Mukherjee, H. D. Sarma, Tapas Das, M. R.A. Pillai, and Meera Venkatesh. Evaluation of 90Y-DTPA and 90Y-DOTA for potential application in intra-vascular radionuclide therapy. *Applied Radiation and Isotopes*, 57(3):313–318, 2002.

[100] Rizzieri DA. Rao AV, Akabani G. Radioimmunotherapy for non-hodgkin's lymphoma. *Clin Med Res.*, 3(3):157–165, 2005.

[101] Rosslyn. Nema standards publication nu 2–2007, performance measurements of positron emission tomographs. `https://www.nema.org`, 2007. Accessed: 2019-11-19.

[102] Thomas B Gaspar D Maqsood Y Harald HQ Bernhard S. Ronald B, Ivo R. Quality control for quantitative multicenter

whole-body pet/mr studies: a nema image quality phantom study with three current pet/mr systems. *Med Phys.*, 42:59–61, 2015,.

[103] Harald B Daniel HP Harald HQ. Susanne Z, Bjoern WJ. Nema image quality phantom measurements and attenuation correction in integrated pet/mr hybrid imaging. *EJNMMI Physics.*, 2:18, 2015.

[104] Braad PEN. Pet imaging with the non-pure positron emitters: Co-55, y-86 and i-124. *Phys Med Biol.*, 60(9):3479, 2015.

[105] Alexander M. Grant, Timothy W. Deller, Mohammad Mehdi Khalighi, Sri Harsha Maramraju, Gaspar Delso, and Craig S. Levin. NEMA NU 2-2012 performance studies for the SiPM-based ToF-PET component of the GE SIGNA PET/MR system. *Medical Physics*, 43(5):2334–2343, 2016.

[106] Rebekka Kraus, Gaspar Delso, and Sibylle I. Ziegler. Simulation study of tissue-specific positron range correction for the new biograph mMR whole-body PET/MR system. *IEEE Transactions on Nuclear Science*, 59(5 PART 1):1900–1909, 2012.

[107] N. Jon Shah, Hans Herzog, Christoph Weirich, Lutz Tellmann, Joachim Kaffanke, Liliana Caldeira, Elena Rota Kops, Syed M. Qaim, Heinz H. Coenen, and Hidehiro Iida. Effects of magnetic fields of up to 9.4 T on resolution and contrast of PET images as measured with an MR-BrainPET. *PLoS ONE*, 9(4), 2014.

[108] GE Healthcare. Signa pet/mr nema nu 2–2007 manual. `https://www.nema.org`, 2007. Accessed: 2019-11-18.

[109] Estelle Spasic, Nina Jehanno, Sandy Blondeel Gomes, Virginie Huchet, Marie Luporsi, and Thibaut Cassou Mounat. Phantom and Clinical Evaluation for New PET/CT Reconstruction Algorithm: Bayesian Penalized Likelihood Reconstruction Algorithm Q.Clear. *Journal of Nuclear Medicine & Radiation Therapy*, 09(04), 2018.

[110] Jansen FP Glover GH. Deller Timothy W, Khalighi MM. Pet imaging stability measurements during simultaneous pulsing of aggressive mr sequences on the signa pet/mr system. *J Nucl Med.*, 59(1):167–172, 2018.

[111] et. al. Ottavia BB. Pet iterative reconstruction incorporating an efficient positron range correction method. *Physica Medica.*, 32:323–330, 2016.

[112] Minamimoto R Jamali M Levin C Quon A Gold G Herfkens R Vasanawala S Gambhir SS Zaharchuk G. Iagaru A, Mittra E. Simultaneous whole-body time-of-flight 18f-fdg pet/mri: a pilot study comparing suv_{max} with pet/ct and assessment of mr image quality. *Clin Nucl Med.*, 40(1):1–8, 2015.

[113] Paulo Caribé, Michel Koole, Tim Deller, and Stefaan Vandenberghe. Ge signa integrated pet/mr : Nema nu 2–2007 performance characteristics for different pet isotopes. In *XXXI Congresso Brasileiro de Medicina Nuclear*, 2017.

[114] Paulo Caribé, Michel Koole, and Stefaan Vandenberghe. Monte carlo simulation of the effect of magnetic field on positron range in the ge signa integrated pet/mr system. Belnuc Ghent, 2017.

[115] Paulo Caribé, Michel Koole, Stefaan Vandenberghe, and T. Deller. Ge signa integrated pet/mr : Nema nu 2–2007 performance characteristics for ga-68 pet imaging. In *EANM'17 : abstracts*, volume 44, pages S507–S508, 2017.

[116] Paulo R. R. V. Caribé, Michel Koole, Stefaan Vandenberghe, Tim Deller, and K. Van Laere. Nema nu 2-2007 performance characteristics of ge signa integrated pet/mr: impact of using different pet isotopes. In *EANM'17*, volume 44, pages OP–615:S339–OP–615:S339, 2017.

[117] Paulo Caribé, Michel Koole, Hugo Bertin, Yves D'Asseler, and Stefaan Vandenberghe. Nema nu 2012 performance evaluation of silicon-photomultiplier– based and conventional pmt-based time-of-flight systems. *EJNMMI Physics 2018*, 2018.

[118] Paulo R. R. V. Caribé, M. Koole, Yves D'Asseler, Timothy W. Deller, K. Van Laere, and S. Vandenberghe. NEMA NU 2–2007 performance characteristics of GE Signa integrated PET/MR for different PET isotopes. *EJNMMI Physics*, 6(1):11, dec 2019.

[119] Yiping Shao, Simon R Cherry, Keyvan Farahani, Ken Meadors, Stefan Siegel, Robert W Silverman, and Paul K Marsden. Simultaneous PET and MR imaging. *Physics in Medicine and Biology*, 42(10):1965–1970, oct 1997.

[120] C. Catana, A. van der Kouwe, T. Benner, C. J. Michel, M. Hamm, M. Fenchel, B. Fischl, B. Rosen, M. Schmand, and A. G. Sorensen. Toward Implementing an MRI-Based PET Attenuation-Correction Method for Neurologic Studies on the MR-PET Brain Prototype. *Journal of Nuclear Medicine*, 51(9):1431–1438, sep 2010.

[121] S. Yamamoto, K. Kuroda, and M. Senda. Scintillator selection for MR compatible gamma detectors. *2002 IEEE Nuclear Science Symposium Conference Record*, 3(5):1632–1635, 2003.

[122] G Soultanidis, N Karakatsanis, G Nikiforidis, and G Loudos. Study of the effect of magnetic field in positron range using GATE simulation toolkit. *Journal of Physics: Conference Series*, 317(1):012021, sep 2011.

[123] Fuyan Liu Haohui Tang Zhiming Zhang Baoyi Wang Chong Li, Xingzhong Cao and Long Wei. Compressive effect of the magnetic field on the positron range in commonly used positron emitters simulated using geant4. *The European Physical Journal Plus*, 132(484), 2017.

[124] G Soultanidis, N Karakatsanis, G Nikiforidis, and G Loudos. Study of the effect of magnetic field in positron range using GATE simulation toolkit. *Journal of Physics: Conference Series*, 317:012021, sep 2011.

[125] A. Wagadarikar M. Khalif, S. Stute and C. Comtat. Modelling the ge signa pet-mr with monte-carlo simulations using gate. *IEEE*

Nuclear Science Symposium and Medical Imaging Conference, (1), 2015.

[126] Paulo Caribe, Andre Diogo, and Stefaan Vandenberghe. Ge signa integrated pet/mr: evaluation of positron range for clinically relevant pet isotopes. *17th National Day on Biomedical Engineering*, (8608252), 2018.

[127] Paulo Caribé, Michel Koole, Andre Diogo, Yves D'Asseler, and Stefaan Vandenberghe. Nema nu 2–2007 measurements and gate monte carlo simulations of ge signa integrated pet/mr for different pet isotopes. In *8th IEEE CONFERENCE on PET/MR and SPECT/MR*, 2019.

[128] Paulo Caribé, Michel Koole, Andre Diogo, Yves D'Asseler, Timothy Deller, and Stefaan Vandenberghe. Nema nu 2-2007 measurements and gate monte carlo simulations of ge signa integrated pet/mr for pure and non-pure positron emitters. *32nd Annual Congress of the European Association of Nuclear Medicine - EANM19*, 2019.

[129] André Diogo, Paulo Caribé, Yves D'Asseler, Michel Koole, and Stefaan Vandenberghe. Ge signa integrated pet/mr system: results of the nema nu2-2007 tests and a gate monte carlo study of the clinically available isotopes. In *19th Symposium of the Belgian Society of Nuclear Medicine*, 2019.

[130] Gerd Muehllehner and Joel S Karp. Positron emission tomography. *Physics in Medicine and Biology*, 51(13):R117–R137, jun 2006.

[131] Tong S et al. Alessio AM, Stearns CW. Application and evaluation of a measured spatially variant system model for pet image reconstruction. *IEEE Trans Med Imaging*, 29(13):938–949, 2010.

[132] H Malcolm Hudson and Richard S Larkin. Accelerated image reconstruction using ordered subsets of projection data. *IEEE transactions on medical imaging*, 13(4):601–609, 1994.

[133] S. Vandenberghe, Y. D'Asseler, R. Van De Walle, T. Kauppinen, M. Koole, L. Bouwens, K. Van Laere, I. Lemahieu, and R. A.

Dierckx. Iterative reconstruction algorithms in nuclear medicine. *Computerized Medical Imaging and Graphics*, 25(2):105–111, 2001.

[134] Ian S. Armstrong, Matthew D. Kelly, Heather A. Williams, and Julian C. Matthews. Impact of point spread function modelling and time of flight on FDG uptake measurements in lung lesions using alternative filtering strategies. *Archiv der Mathematik*, 1(1):1–18, 2014.

[135] Elena Prieto, Inés Domínguez-Prado, María José García-Velloso, Iván Peñuelas, José Ángel Richter, and Josep Maria Martí-Climent. Impact of time-of-flight and point-spread-function in SUV quantification for oncological PET. *Clinical Nuclear Medicine*, 38(2):103–109, 2013.

[136] Anastasios Gaitanis, George Kontaxakis, George Spyrou, George Panayiotakis, and George Tzanakos. Pet image reconstruction: A stopping rule for the mlem algorithm based on properties of the updating coefficients. *Computerized Medical Imaging and Graphics*, 34(2):131 – 141, 2010.

[137] Qi J. Wang G. Penalized likelihood pet image reconstruction using patch-based edge-preserving regularization. *IEEE Trans Med Imaging*, 31(12):2194–2204, 2012.

[138] C Tsoumpas, I Polycarpou, K Thielemans, C Buerger, A P King, T Schaeffter, and P K Marsden. The effect of regularization in motion compensated PET image reconstruction: a realistic numerical 4d simulation study. *Physics in Medicine and Biology*, 58(6):1759–1773, feb 2013.

[139] Sangtae Ahn and Jeffrey A. Fessler. Globally convergent image reconstruction for emission tomography using relaxed ordered subsets algorithms. *IEEE Transactions on Medical Imaging*, 22(5):613–626, 2003.

[140] Dupont P Mortelmans L. Nuyts J, Bequé D. A concave prior penalizing relative differences for maximum-a-posteriori reconstruc-

tion in emission tomography. *IEEE Trans Med Imaging*, 49(1):56–60, 2002.

[141] Elin Lindström, Anders Sundin, Carlos Trampal, Lars Lindsjö, Ezgi Ilan, Torsten Danfors, Gunnar Antoni, Jens Sörensen, and Mark Lubberink. Evaluation of penalized-likelihood estimation reconstruction on a digital time-of-flight PET/CT scanner for 18 F-FDG whole-body examinations. *Journal of Nuclear Medicine*, 59(7):1152–1158, 2018.

[142] Teoh EJ McGowan DR Bradley KM Belcher E Black E Gleeson FV. Novel penalised likelihood reconstruction of pet in the assessment of histologically verified small pulmonary nodules. *Eur Radiol*, 26:56–60, 2016.

[143] Sangtae Ahn, Steven G Ross, Evren Asma, Jun Miao, Xiao Jin, Lishui Cheng, Scott D Wollenweber, and Ravindra M Manjeshwar. Quantitative comparison of OSEM and penalized likelihood image reconstruction using relative difference penalties for clinical PET. *Physics in Medicine and Biology*, 60(15):5733–5751, jul 2015.

[144] Nassim Parvizi, James M. Franklin, Daniel R. McGowan, Eugene J. Teoh, Kevin M. Bradley, and Fergus V. Gleeson. Does a novel penalized likelihood reconstruction of 18f-fdg pet-ct improve signal-to-background in colorectal liver metastases? *European Journal of Radiology*, 84(10):1873 – 1878, 2015.

[145] et al. Reynés-Llompart G. Phantom, clinical, and texture indices evaluation and optimization of a penalized-likelihood image reconstruction method (q.clear) on a bgo pet/ct scanner. *Med Phys*, 45(7):3214–3222, jul 2018.

[146] Charlotte S. van der Vos, Daniëlle Koopman, Sjoerd Rijnsdorp, Albert J. Arends, Ronald Boellaard, Jorn A. van Dalen, Mark Lubberink, Antoon T. M. Willemsen, and Eric P. Visser. Quantification, improvement, and harmonization of small lesion detection with state-of-the-art pet. *European Journal of Nuclear Medicine and Molecular Imaging*, 44(1):4–16, Aug 2017.

[147] Eugene J. Teoh, Daniel R. McGowan, Ruth E. Macpherson, Kevin M. Bradley, and Fergus V. Gleeson. Phantom and clinical evaluation of the Bayesian penalized likelihood reconstruction algorithm Q.Clear on an LYSO PET/CT system. *Journal of Nuclear Medicine*, 56(9):1447–1452, 2015.

[148] Sattar A et al. Nguyen NC, Vercher-Conejero JL. Image quality and diagnostic performance of a digital pet prototype in patients with oncologic diseases: initial experience and comparison with analog pet. *J Nucl Med.*, 56:1447–1452, 2015.

[149] Arman Rahmim, Jinyi Qi, and Vesna Sossi. Resolution modeling in PET imaging: Theory, practice, benefits, and pitfalls. *Medical Physics*, 40(6):1–15, 2013.

[150] Michael Messerli, Paul Stolzmann, Michèle Egger-Sigg, Josephine Trinckauf, Stefano D'Aguanno, Irene A. Burger, Gustav K. von Schulthess, Philipp A. Kaufmann, and Martin W. Huellner. Impact of a Bayesian penalized likelihood reconstruction algorithm on image quality in novel digital PET/CT: clinical implications for the assessment of lung tumors. *EJNMMI Physics*, 5(1), 2018.

[151] Michael Messerli, Fotis Kotasidis, Irene A. Burger, Daniela A. Ferraro, Urs J. Muehlematter, Corina Weyermann, David Kenkel, Gustav K. von Schulthess, Philipp A. Kaufmann, and Martin W. Huellner. Impact of different image reconstructions on pet quantification in non-small cell lung cancer: a comparison of adenocarcinoma and squamous cell carcinoma. *The British Journal of Radiology*, 92(1096):20180792, 2019. PMID: 30673302.

[152] Paulo Caribé, Lois Kay, Yves D'Asseler, and Stefaan Vandenberghe. Bayesian penalized-likelihood reconstruction algorithm : noise reduction study of different contrast ratios. In *Biomedical Engineering Day*, 2019.

[153] Paulo Caribé, Lois Kay, Yves D'Asseler, Bliede Van den Broeck, and Stefaan Vandenberghe. Bayesian penalized-likelihood reconstruction algorithm: Noise reduction study on a 15 cm axial field-

of-view pet/ct scanner. In *19th Symposium of the Belgian Society of Nuclear Medicine*, 2019.

[154] Lois Kay, Paulo Caribé, Yves D'Asseler, Bliede Van den Broeck, and Stefaan Vandenberghe. Bayesian penalized-likelihood reconstruction algorithm : noise reduction study of different contrast ratios. In *Master of Science in Biomedical Engineering*, 2019.

[155] Paulo Caribé, Georg Schramm, Yves D'Asseler, Hugo Bertin, Michel Koole, and Stefaan Vandenberghe. Image quality evaluation of sipm-based and standard pmt-based time-of-flight systems for yttrium-90 pet/ct imaging. *Springer Berlin Heidelberg. 2017. Eur J Nucl Med Mol Imaging.*, 2018.

[156] Paulo Caribé, M Koole, Yves D'Asseler, Bliede Van den Broeck, and Stefaan Vandenberghe. Noise reduction using a bayesian penalized-likelihood reconstruction algorithm on a time-of-flight pet-ct scanner. *EJNMMI PHYSICS*, 6:14, 2019.

[157] Xiaofeng Niu Huini Du Karthik Balakrishnan Hongwei Ye Gin-Chung Wang, Xiaoli Li and Kent Burr. Pet timing performance measurement method using nema nec phantom. *IEEE Transactions on Nuclear Science*, 63(6), 2016.

[158] Michel Hesse and Stephan Walrand. Significant artefactual noise in ^{90}y tof-pet imaging of low specific activity phantoms arises despite increased acquisition time. *EJNMMI Physics*, 20:6, 2019.